



AFRL-RB-WP-TR-2012-0060

**STRUCTURAL TECHNOLOGY EVALUATION AND
ANALYSIS PROGRAM (STEAP)**

**Delivery Order 0042: Development of the Equivalent Overload Model,
Demonstration of the Failure of Superposition, and
Relaxation/Redistribution Measurement**

**Thomas B. Mills, Kyle T. Honeycutt, Scott A. Prost-Domasky, and Craig L. Brooks
APES, Inc.**

**SEPTEMBER 2011
Final Report**

Approved for public release; distribution unlimited.

See additional restrictions described on inside pages

STINFO COPY

**AIR FORCE RESEARCH LABORATORY
AIR VEHICLES DIRECTORATE
WRIGHT-PATTERSON AIR FORCE BASE, OH 45433-7542
AIR FORCE MATERIEL COMMAND
UNITED STATES AIR FORCE**

NOTICE AND SIGNATURE PAGE

Using Government drawings, specifications, or other data included in this document for any purpose other than Government procurement does not in any way obligate the U.S. Government. The fact that the Government formulated or supplied the drawings, specifications, or other data does not license the holder or any other person or corporation; or convey any rights or permission to manufacture, use, or sell any patented invention that may relate to them.

This report was cleared for public release by the USAF 88th Air Base Wing (88 ABW) Public Affairs Office (PAO) and is available to the general public, including foreign nationals. Copies may be obtained from the Defense Technical Information Center (DTIC) (<http://www.dtic.mil>).

AFRL-RB-WP-TR-2012-0060 HAS BEEN REVIEWED AND IS APPROVED FOR PUBLICATION IN ACCORDANCE WITH THE ASSIGNED DISTRIBUTION STATEMENT.

*//Signature//

ROBERT A. REUTER
Associate Materials Research Engineer
Analytical Mechanics Branch
Structures Division

//Signature//

MICHAEL J. SHEPARD, Ph.D., Chief
Analytical Mechanics Branch
Structures Division

//Signature//

DAVID M. PRATT, Ph.D.
Technical Advisor
Structures Division
Air Vehicles Directorate

This report is published in the interest of scientific and technical information exchange, and its publication does not constitute the Government's approval or disapproval of its ideas or findings.

*Disseminated copies will show “//Signature//” stamped or typed above the signature blocks.

REPORT DOCUMENTATION PAGE

*Form Approved
OMB No. 0704-0188*

The public reporting burden for this collection of information is estimated to average 1 hour per response, including the time for reviewing instructions, searching existing data sources, gathering and maintaining the data needed, and completing and reviewing the collection of information. Send comments regarding this burden estimate or any other aspect of this collection of information, including suggestions for reducing this burden, to Department of Defense, Washington Headquarters Services, Directorate for Information Operations and Reports (0704-0188), 1215 Jefferson Davis Highway, Suite 1204, Arlington, VA 22202-4302. Respondents should be aware that notwithstanding any other provision of law, no person shall be subject to any penalty for failing to comply with a collection of information if it does not display a currently valid OMB control number. **PLEASE DO NOT RETURN YOUR FORM TO THE ABOVE ADDRESS.**

1. REPORT DATE (DD-MM-YY) September 2011			2. REPORT TYPE Final		3. DATES COVERED (From - To) 16 January 2009 – 16 January 2011	
4. TITLE AND SUBTITLE STRUCTURAL TECHNOLOGY EVALUATION AND ANALYSIS PROGRAM (STEAP) Delivery Order 0042: Development of the Equivalent Overload Model, Demonstration of the Failure of Superposition, and Relaxation/Redistribution Measurement			5a. CONTRACT NUMBER FA8650-04-D-3446-0042			
			5b. GRANT NUMBER			
			5c. PROGRAM ELEMENT NUMBER 62201F			
6. AUTHOR(S) Thomas B. Mills, Kyle T. Honeycutt, Scott A. Prost-Domasky, and Craig L. Brooks			5d. PROJECT NUMBER 2401			
			5e. TASK NUMBER			
			5f. WORK UNIT NUMBER A0FU0A			
7. PERFORMING ORGANIZATION NAME(S) AND ADDRESS(ES) By: APES, Inc. 6669 Fyler Avenue St. Louis, MO 63139			For: General-Dynamics Information Technology 5100 Springfield Pike, Suite 509 Dayton, OH 45431			
9. SPONSORING/MONITORING AGENCY NAME(S) AND ADDRESS(ES) Air Force Research Laboratory Air Vehicles Directorate Wright-Patterson Air Force Base, OH 45433-7542 Air Force Materiel Command United States Air Force			10. SPONSORING/MONITORING AGENCY ACRONYM(S) AFRL/RBSM			
			11. SPONSORING/MONITORING AGENCY REPORT NUMBER(S) AFRL-RB-WP-TR-2012-0060			
12. DISTRIBUTION/AVAILABILITY STATEMENT Approved for public release; distribution unlimited.						
13. SUPPLEMENTARY NOTES PAO Case Number: 88ABW-2012-0633; Clearance Date: 16 Feb 2012. Report contains color.						
14. ABSTRACT This project has the goal of focusing on a few of the key issues and questions related to cold working of holes in aircraft grade metals: relaxation and redistribution of residual stresses, and models of crack propagation in complex residual stress fields.						
15. SUBJECT TERMS corrosion damage tolerance, criticality assessment, environment corrosion sensors, structural health, service life prediction, non-destructive inspection, optimized maintenance						
16. SECURITY CLASSIFICATION OF: a. REPORT Unclassified		17. LIMITATION OF ABSTRACT: b. ABSTRACT Unclassified		18. NUMBER OF PAGES c. THIS PAGE Unclassified SAR 132	19a. NAME OF RESPONSIBLE PERSON (Monitor) Robert A. Reuter 19b. TELEPHONE NUMBER (Include Area Code) N/A	

TABLE OF CONTENTS

<u>Section</u>	<u>Page</u>
EXECUTIVE SUMMARY	1
1 Problem Statement	3
2 Objectives	4
3 Basic Material Data.....	5
3.1 Task 1: Material Property Acquisition/Testing.....	5
3.1.1 Test: Fatigue Crack Growth Baseline (ASTM E-647, M(T))	5
3.1.2 Test: Tensile Static Strength (ASTM E-8).....	6
3.1.3 Test: Fracture Toughness (K_{Ic}) (ASTM E-399).....	18
4 Modeling Fatigue in Cold-worked Holes	22
4.1 Test: Open Hole, Non CX Fatigue Tests (Part of Task 1).....	22
4.1.1 Specimen Geometry.....	22
4.1.2 Material	22
4.1.3 AFGROW Crack Model	26
4.1.4 Results and Discussion	26
4.1.5 Digital Image Correlation, Open Hole Coupons.....	30
4.1.6 Results and Discussion	30
4.2 Digital Image Correlation of Cold Worked Holes	37
4.3 Fatigue Testing of Cold-worked Coupons (Task 2)	38
4.4 Modeling Fatigue in Cold-worked Coupons.....	42
4.4.1 Introduction.....	42
4.4.2 Modeling	43
4.4.3 Conclusions.....	52
5 Application of Superposition to Verify the Need for Relaxation and Redistribution Effects (Task 5)	53
5.1 Literature Review.....	53
5.2 Prediction of non CX coupon lives.....	57
5.3 Calculation of Residual Stress Intensity Factors from Traveling Microscope Measurements	60
5.3.1 Modeling	60
5.3.2 Results and Discussion	66
5.3.3 Conclusions.....	69
6 Relaxation/Redistribution Effects (Task 6)	70
6.1 Preliminary Digital Image Correlation	70
6.2 Contour Method Measurements.....	75
6.2.1 Introduction.....	75

6.2.2	Results and Discussion	77
6.2.3	Comparison of Contour Method to X-ray Diffraction.....	84
6.2.4	Cyclic Evolution of Residual Strains Measured by Digital Image Correlation.....	85
6.2.5	Conclusions.....	86
6.3	DIC Data from Task 8 and Observations on Residual Stress Relaxation.....	87
6.3.1	Initial Observations	87
6.3.2	Experiments and Refined Observations	90
6.3.3	Relaxation and Redistribution Parameters.....	96
7	Overload Model	97
7.1	FEA Modeling to Determine the Equivalent Overload (Task 3).....	97
7.1.1	Model	97
7.1.2	Results and Discussion	98
7.2	Analyses Using Equivalent Overload (Task 4).....	101
7.3	Experimental and Analytical Investigation of Overload Model	103
7.3.1	Task 8 Test Results	103
7.3.2	Analysis and Correlation of Task 8 Test Results.....	107
8	Summary and Conclusions	112
9	Reference.....	114
	Appendix.....	116

LIST OF FIGURES

<u>Figure</u>	<u>Page</u>
Figure 1. Comparison of Fatigue Crack Growth Rates from Various Sources (Indicated in Legend)	6
Figure 2. APES Monotonic Stress Strain Coupon	7
Figure 3. Ramberg Osgood Curve Fit to Small Strain Section of Monotonic Stress Strain Relation	8
Figure 4. Ramberg Osgood Curve Fit to Large Strain Section of Monotonic Stress Strain Relation	9
Figure 5. Monotonic Stress Strain Measurements Compared to MIL-HDBK-5 Curve Fits	10
Figure 6. DIC Computed (Lagrangian) Strains.....	11
Figure 7. StressCheck FE Model	12
Figure 8. Normal Stress (Load Direction), $\delta_{end} = 0.029 \text{ in.}$ DIC image shown for reference	12
Figure 9. Comparison of Two Plasticity Constitutive Relations (Ramberg Osgood and Bilinear) to Experimentally Measured Monotonic Stress-Strain Measurements.....	15
Figure 10. MIL-HDBK-5 Ramberg Osgood Material Curve Compared to Experimental Data	16
Figure 11. Close Up of Cold Worked Hole in FE Simulation. Arrow Shows Direction That Residual Stress Computed in Figure 12 Below	17
Figure 12. Residual Stresses, Cold Working Simulations with the Two Plasticity Models	17
Figure 13. APES Fracture Toughness Coupon.....	19
Figure 14. Four 95% Slope Curves and Their Varied P_Q Intersections, Computed From Four Different Initial Tangencies	20
Figure 15. APES Cold Work Specimen Geometry.....	22
Figure 16. NRC-C Specimen Geometry. All dimensions in inches	23
Figure 17. MACS Probability Density Function (Histogram).....	25
Figure 18. Crack Growth Rates, AA2024-T351. EIFSv8.lkp.....	25
Figure 19. Fatigue Crack Scenario.....	26
Figure 20. Fatigue Life Predictions. Open Hole. AA2024-T351	28
Figure 21. Fatigue Life Predictions. Open Hole. AA2024-T351	28
Figure 22. Remaining Life. Open Hole. AA2024-T351	29
Figure 23. Crack Aspect Ratio to Through Crack Transition as a Function of Maximum Applied Stress. Open Hole. AA2024-T351	29
Figure 24. Dogbone Coupon Design	30
Figure 25. Measurement of DIC Noise Floor for a Non-Cx Hole	31
Figure 26. Comparison of FEA Computed Strains to DIC Measured Strains at 12.5 ksi	32
Figure 27. Comparison of FEA Computed Strains to DIC Measured Strains at 15.0 ksi	33
Figure 28. Various Speckle Patterns Used for Noise Measurement	35
Figure 29. Typical Error (Sigma) Values for Eight Speckle Patterns.....	35

Figure 30. Average Standard Deviation in ϵ_{yy} for Eight Speckle Patterns	36
Figure 31. Peak Range of ϵ_{yy} Across All Images	36
Figure 32. Correlation of DIC Measured Strain at 27.5 ksi Applied Load with FEA Simulations	37
Figure 33. Correlation of Shifted DIC Measured Strain at 27.5 ksi Applied Load with FEA Simulations	38
Figure 34. Comparison of Crack Propagation Normalized to Total Life. The Non CX Coupons (2H20/33/34) Collapse Well; the CX Coupons Have Some Qualitative Variations	40
Figure 35. Simulated Fatigue Lives Increase with Decreasing Initial Crack Sizes (Area here); Measured Fatigue Lives Apparently Not Correlated with Initial Crack Sizes	41
Figure 36. The Measured Fatigue Lives Increase with Increasing Cold Working Level. CX Process 1 and CX Process 2 refer to the order of cold working relative to EDM and pre-cracking process as discussed above.....	42
Figure 37. Residual Stress Distribution Measured by Hill Engineering with Contour Method	46
Figure 38. Ratio of Predicted/Actual Lives for Coupons with EDM Notches	47
Figure 39. Ratio of Predicted/Actual Lives for Coupons with Naturally Occurring Cracks	49
Figure 40. Shifted Stress Distribution.....	51
Figure 41. StressCheck Finite Element Mesh.....	53
Figure 42. Relaxation of Residual Hoop Stresses by Compression Load as Measured by XRD and Computed by Finite Element Method. Outlet Face. 100 MPa=14.5 ksi	55
Figure 43. Relaxation of Residual Stresses by Compression Loads.....	56
Figure 44. Relaxation of Residual Stresses by Tension Loads.....	57
Figure 45. Comparison of Two Prediction Methods to the Measured Surface Crack Lengths, Coupon 2H33	59
Figure 46. Schematic of Coupon Design. All dimensions are in inches.....	60
Figure 47. Schematic of Fracture (Crack) Plane. $W = 2.0 \text{ in.}$, $D = 0.25 \text{ in.}$, $t = 0.25 \text{ in.}$	61
Figure 48. Crack Growth Rates for AA2024-T351, EIFSv8.lkp. All Values of Stress Intensity Factor (x-axis) are ΔK if $R \geq 1$, K_{\max} if $R < 1$	62
Figure 49. Residual Stress Intensity Factors for Crack-c and Crack-a. Non Cold Worked	65
Figure 50. Residual Stress Intensity Factors for Crack-c and Crack-a. Cold Worked	65
Figure 51. Correlation of Retro-dictions Using Residual SIFs to Measured Fatigue Lives. Cold Worked Coupons	67
Figure 52. Correlation of Retro-dictions to Measured Fatigue Lives, Naturally Occurring Cracks ..	68
Figure 53. Strain Measured at Periodic Fatigue Cycle Intervals. ϵ_{yy} -left.....	70
Figure 54. Strain Measured at Periodic Fatigue Cycle Intervals. ϵ_{yy} -right.....	71
Figure 55. Location of Strain Results	72
Figure 56. Strain Changes with Cycling, Measured During Zero Load Dwells.....	74
Figure 57. Strain Changes with Cycling, Measured During 25 ksi Load Dwells.....	74
Figure 58. Strain Changes Adjacent to the Hole.....	75
Figure 59. Measurement Plane Cross Section. Line 1 is "Mid Plane," Line 2 is "Hole Edge Left," Line 3 is "Hole Edge Right," Line 4 is "Entry Side," and Line 5 is "Exit Side"	76

Figure 60. Mid Plane Residual Stress Measurements, Line 1. 2H21-3 are not cold worked or cyclically loaded, 2H24-6 are cold worked but not cyclically loaded, 2H27-8 are cold worked and loaded for 100 cycles, 2H29-30 are cold worked and loaded for 5,000 cycles, and 2H31-32 are cold worked and loaded for 50,000 cycles.....	77
Figure 61. Left Side Bore Edge Residual Stress Measurements, Line 2. 2H21-3 are not cold worked or cyclically loaded, 2H24-6 are cold worked but not cyclically loaded, 2H27-8 are cold worked and loaded for 100 cycles, 2H29-30 are cold worked and loaded for 5,000 cycles, and 2H31-32 are cold worked and loaded for 50,000 cycles.....	78
Figure 62. Right Side Bore Edge Residual Stress Measurements, Line 3. 2H21-3 are not cold worked or cyclically loaded, 2H24-6 are cold worked but not cyclically loaded, 2H27-8 are cold worked and loaded for 100 cycles, 2H29-30 are cold worked and loaded for 5,000 cycles, and 2H31-32 are cold worked and loaded for 50,000 cycles.....	79
Figure 63. Residual Stress Measurements, Line 4, “Entry Side.” 2H21-3 are not cold worked or cyclically loaded, 2H24-6 are cold worked but not cyclically loaded, 2H27-8 are cold worked and loaded for 100 cycles, 2H29-30 are cold worked and loaded for 5,000 cycles, and 2H31-32 are cold worked and loaded for 50,000 cycles.....	80
Figure 64. Residual Stress Measurements, Line 5, “Exit Side.” 2H21-3 are not cold worked or cyclically loaded, 2H24-6 are cold worked but not cyclically loaded, 2H27-8 are cold worked and loaded for 100 cycles, 2H29-30 are cold worked and loaded for 5,000 cycles, and 2H31-32 are cold worked and loaded for 50,000 cycles.....	81
Figure 65. Both Bore Edge Residual Stress Measurements in Non Cold Worked Coupons Along Left (Line 2) and Right (Line 3) Hole Edges. 2H21-3 are not cold worked or cyclically loaded.....	82
Figure 66. Averaged Relative Residual Stress Measurements as a Function of pre-Applied Load Cycles, Line 3. A StressCheck simulation, marked “SOTA FEA” of 4% CX is added for reference.....	83
Figure 67. Averaged Residual Stress Measurements, 4% CX, No Load. Exit, Middle and Entry Planes	83
Figure 68. Residual Hoop Stress Measurements, 4% CX, Entry Plane, Variable Cycles	84
Figure 69. Comparison of Residual Stress Measurements with CM and XRD Methods, 0 Load Cycles.....	85
Figure 70. Residual Strain Measurements, 4% CX, Entry Face, Variable Cycles	86
Figure 71. Comparison of Surface Strain Changes near the Hole for 2H06 and 2H05	88
Figure 72. Remaining Life Plot for Specimens ‘Similar’ to 2H06 and 2H05	89
Figure 73. IC Strain Changes vs. Expected Surface Crack Length	90
Figure 74. Normalized spectrum MB-DIC for specimens 2H35 and 2H36	91
Figure 75. Strain Extraction Line, Definition of “Group C”, and Loading Direction (Y).....	92
Figure 76. Marker Band Crack Growth Plots for 2H35 and 2H36	92
Figure 77. IC Strain Changes vs. Total Life for 2H35 and 2H36.....	93
Figure 78. IC Strain Changes vs. Marker Band Surface Crack Length for 2H35 and 2H36.....	93
Figure 79. IC Strain Changes vs. Marker Band Surface Crack Length for Multiple Experiments	95
Figure 80. Finite Element Mesh. Overload Model	97

Figure 81. Cold Working (CX) and Overload Simulations, 2 inch Gage Widths	100
Figure 82. Cold Working (CX) and Overload Simulations, 1.5 inch Gage Widths	100
Figure 83. Computed Residual Stresses by Tensile Overload Level.....	101
Figure 84. Comparison of Fatigue Crack Growth Rates from Various Sources (Indicated in Legend)	102
Figure 85. Results Using CA Spectrum: Non Cx, overload, Cx test, and Cx estimates.....	105
Figure 86. Results Using MB-DIC Spectrum, Non Cx, overload, and Cx	106
Figure 87. Model P/A Performance, 50% IDS Initial Crack	109
Figure 88. Model P/A Performance, 0.005" Initial Crack	109
Figure 89. Model P/A Performance, 0.05" Initial Crack	110
Figure 90. Current Industry Practice for Predicting Fatigue Life of Cold Worked Holes.....	111

LIST OF TABLES

<u>Table</u>	<u>Page</u>
Table 1. Summary of Elastic and Plastic Constants	10
Table 2. Average Strain in Load Direction.....	11
Table 3. Average Engineering Quantities in Load (Axial) Direction.....	13
Table 4. Material Constitutive Parameters for Two Ramberg-Osgood Plasticity Relations	15
Table 5. E 399-08 Specimen Test Results	19
Table 6. Results of Four Tangency Scenarios for Specimen 2F01. $P_{max} = 5.17$ kips	21
Table 7. Distribution of Initial Discontinuity State (IDS)	24
Table 8. Initial Discontinuity States Used in Fatigue Life Predictions.....	24
Table 9. Remaining Life at Maximum Stress of 25 ksi	27
Table 10. Summary of Fatigue Behaviors of AA2024 non CX (2H20/2H33/2H34) and CX Coupons (all others).....	39
Table 11. Test Data for Coupons with Naturally Occurring Cracks.....	43
Table 12. Verification of the Weight Function Method for Single Corner Crack at a Hole in an Infinite Plate.....	44
Table 13. AFGROW Reference Modeling, Non CX Coupons. MB18==Marker Band 18.....	44
Table 14. Effect of Default Angles on AFGROW Life Predictions, Non CX Coupons. Actual Life is 40,352 cycles	45
Table 15. Effect of Default Angles on AFGROW Life Predictions, CX Coupons. Actual Life is 195,695 cycles.....	45
Table 16. Predictions of EDM Notch Coupon Lives	47
Table 17. Predictions of Coupons with Naturally Occurring Cracks	48
Table 18. Corner Crack with Independent Stress Drivers	50
Table 19. Corner Crack at Hole with Superposed Residual and Open Hole Stress.....	51
Table 20. Bilinear Material Parameters	54
Table 21. Summary of Retro-dictions.....	58
Table 22. Test Matrix for Traveling Microscope Measurements	61
Table 23. Residual K K_{res} for Each Crack Tip. Non Cold Worked.....	64
Table 24. Residual K K_{res} for Each Crack Tip. Cold Worked.....	64
Table 25. Summary of Measured Fatigue Lives and Retro-dictions Using K_{res}	66
Table 26. Coupon Test Results	67
Table 27. Initial Crack Dimensions. AA2024-T351 IDS	68
Table 28. Retro-dictions of Coupon Lives.....	68
Table 29. Coupon Matrix	76
Table 30. Marker band spectrum MB-DIC.....	90
Table 31. Specimen Details.	91

Table 32. Task 8 Specimens Selected for IC Correlation vs. Marker Band Crack Length	94
Table 33. Task 8 Specimen Details and Results. All cracks were naturally occurring	104
Table 34. 37 ksi Overload Factor, Relative to the Maximum Spectrum Stress.....	106
Table 35. Models A, B, C, and Associated Residual Stress Profiles.....	107
Table 36. Analysis Matrix, Predicted Life Values, Actual Test Values, and P/A Metric	108

EXECUTIVE SUMMARY

This report is the final deliverable for the “Development of the Equivalent Overload Model, Demonstration of the Failure of Superposition, and Relaxation/Redistribution Measurement Program”, STEAP Task Order 42, Contract FA8650-04-D-3446, executed by Analytical Processes/Engineered Solutions (APES, Inc.) in St. Louis, Missouri.

The overall objective of this program was to research the residual stress behavior around cold-worked holes that are subsequently subjected to cyclic loads, with particular emphasis on measuring stress or strain relaxation (if present) and observation of the damage progression for this specific manufacturing process. The focus of this research was to evaluate, from the physical study of the material and fatigue behavior of cold-worked holes and non-cold-worked holes, the suitability of some industry proposed analytical models. All tests were performed with aluminum alloy AA2024-T351 using simple element specimens and standard material behavior coupons.

Specific goals accomplished in this program were to:

1. Use a non-destructive inspection (NDI) method, Digital Image Correlation, to measure surface strains around cold worked holes. These measurements were used to attempt to measure strain relaxation due to load cycling, with the result that no relaxation was discernable under conditions common for fighter aircraft wings skins.
2. Use a destructive technique, Contour Method Measurements (CMM), to measure interior residual stresses at several pre-determined load cycle intervals, 0, 100, 5,000, and 50,000 cycles. Changes observed could not be directly attributed to “relaxation,” as computations approximating indications of early cracking showed good explanation of “redistribution” of stress. The CMM experiments did provide significant insight into the damage progression path.
3. Characterize the material with monotonic stress-strain tests (ASTM E08 tests to measure Young’s modulus, yield stress, and power law parameters for 2024-T351), fatigue crack growth rates (E647 tests), and fracture toughness (ASTM E-399 tests). All material parameters appeared to fall in line with MIL-HDBK-5 data for this material and showed consistent behavior in replicate tests.
4. Predictions were completed for all tests before the particular test was run, to establish a “benchmark” reference state-of-the-art (SOTA). After tests were completed, retrodictions were completed and compared to measured results illustrating the strengths and, moreso, the deficiencies of some of the analytical approximations.
5. Evaluate the efficacy of an equivalent overload model. The equivalent overload stress selected to mimic the effect of cold working was 37 ksi based upon the better correlation of finite element computed residual stresses in a crack growth analysis against the experimental life of 4% cold worked coupons, under specific conditions. Fatigue testing with coupons that had been loaded with a single 37 ksi pulse prior to subsequent cycling were not favorable to this method.

The use of a single overload model does not adequately simulate the crack size progression during the actual measurements of the fatigue process under cold-worked conditions as performed. While the overall experiment and analytical calibration indicates a common failure point, the fracture path (crack size as a function of cycles) is not suitable for establishing analytical confidence, thus the technique has limited applications. Other analytical methods are advised for a long-term robust solution for predicting the optimum service life benefits of the cold-worked process. A simple empirically-derived scale factor would accomplish the objectives

as well as the single over-load model and be more honest to continued assessment methods development and aircraft applications.

This report is divided into eight (8) major sections, along with an Appendix with supporting data:

1. Problem Statement
2. Objectives
3. Basic Material Data
4. Modeling Fatigue in Cold-worked Holes
5. Application of Superposition to Verify the Need for Relaxation and Redistribution Effects
6. Relaxation/Redistribution Effects
7. Overload Model
8. Summary & Conclusions

1 Problem Statement

Current analysis methods cannot accurately predict crack growth through cold-worked holes. This inability may be due to inadequacies in quantifying the effect of material relaxation (changes of the stress state in the time domain, and due to mechanical working) or load redistribution (changes of the stress state, maintaining equilibrium as cracking develops and progresses). This inability may also be in the application of linear, pseudo non-linear, finite element simulations of materials and their relationships in quasi-linear elastic fracture mechanics algorithms to extreme yielding (non-linear) conditions.

This 6.2 project has the goal of focusing on a few of the key issues and questions related to cold working of holes in aircraft grade metals: relaxation and redistribution of residual stresses, and models of crack propagation in complex residual stress fields.

2 Objectives

The technical objectives of this program are to:

- 1) Explore an approach to using an equivalent overload to simulate a cold-worked hole in fatigue, quantify the process' accuracy, and identify approach strengths & weaknesses.
- 2) Determine the effect of relaxation and/or redistribution effects caused by fatigue loads on a cold worked hole in the laboratory environment and project field environment concerns based upon engineering observations.
- 3) Demonstrate the ability of the equivalent overload concept to predict crack growth behavior at cold worked holes and characterize the suitability of the approach for USAF "lifing" philosophies.
- 4) Provide recommendations to USAF AFRL of suitable criteria for individual aircraft or fleet applications—subject to resolution of Conclusions and Recommendations section

3 Basic Material Data

This section of the report details basic material data collected under this effort. Tests completed include those for basic tensile properties, fatigue crack growth, and fracture toughness. The tensile data and fatigue crack growth data were gathered in 2042-T351, 0.25" thick aluminum plate (the same thickness used in subsequent cold worked (CW) fatigue tests. The fracture toughness data was gathered in 1" thick plate per USAF direction. Since the thickness of the fracture toughness coupons was much greater than that of the various fatigue and tensile coupons, the toughness properties cannot be considered directly relevant to the thinner plate.

3.1 Task 1: Material Property Acquisition/Testing

The technical goals of Task 1 were primarily designed to verify suitable quality and material performance for the alloy selected. Various tests were completed to make this determination, to include:

- ASTM E-647 crack growth (da/dN vs ΔK) at $R = 0$ (2 replicates)
- ASTM E-8 monotonic stress-strain curve (E, yield stress, plastic behavior, etc.) (3 reps)
- ASTM E-399 K_{Ic} (3 replicates)
- Simple, Open Hole, Non-Cx Fatigue Tests $R = 0.0$ at 25 ksi (3 replicates)

3.1.1 Test: Fatigue Crack Growth Baseline (ASTME E-647, M(T))

These tests obtained basic long-crack fatigue crack growth rates (FCGRs) for 0.25 in. thick AA2024-T351. The FCGR test was conducted according to ASTM Test Standard E-647, Ref. [1]. The standard calls for a decreasing/increasing K load cycling to capture the fatigue threshold. Because the fatigue threshold was expected to be on the order of 3.2 ksi-in^{1/2}, the crack growth rates are on the order of 1E-9 in/cycle. Each crack growth increment was measured and recorded per the standard. The raw data from this test is plotted against several comparison curve, Figure 1. These include "Harter-T" data from AFGROW, a NASGRO material curve fit, and data from another Air Force database (A5P10XX), Ref. [2]. Also shown are historical material models for 2024-T351 that attempt to account for "small crack effects" that are missed by the E-647 type testing. These are identified in Figure as AGARD v6 (which is a fit of AGARD short crack data Ref. [3] and EIFSv8.lkp, which an APES material model that is designed to capture crack growth from constituent-particle-sized discontinuities in a fracture mechanics framework, Ref. [4].

The 2I02 coupon raw data is marked with DIAMONDS in Figure 1; 2I04 raw data is shown with PLUSSES (crosses), and 2I05 data is shown with STARS. The measured thresholds in Stress Intensity Factor are comparable to those measured in M(T) coupon 2I02; the so-called "long crack threshold" appears to be about 3.0 to 3.5 ksi-in^{1/2} for coupons 2I02 and 2I04.

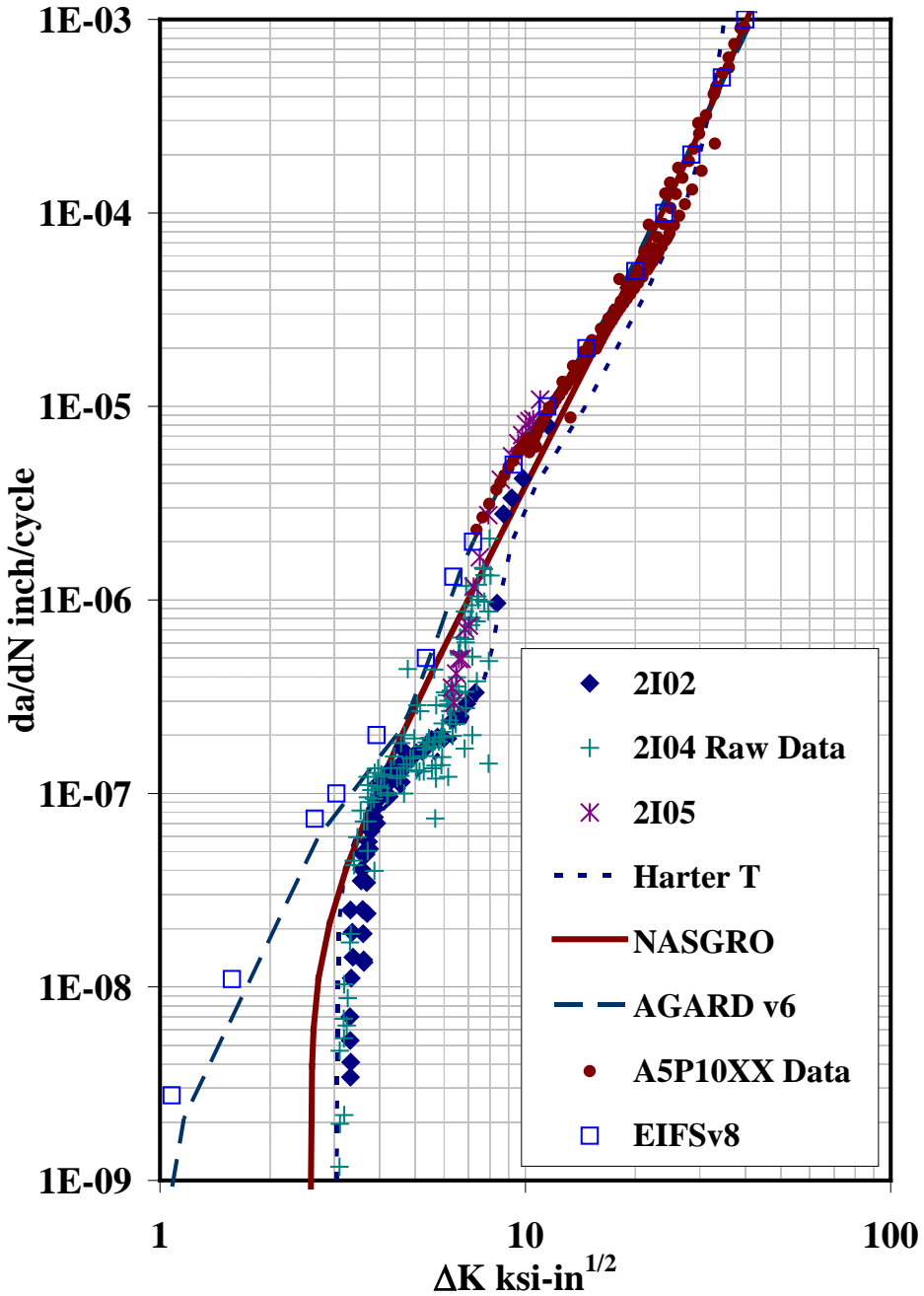


Figure 1. Comparison of Fatigue Crack Growth Rates from Various Sources (Indicated in Legend)

3.1.2 Test: Tensile Static Strength (ASTM E-8)

The monotonic stress strain behavior of Aluminum Alloy 2024-T351 was measured using ASTM E-08 protocol on APES' 22 kip MTS machine. Digital Image Correlation (DIC) was used to measure displacements and compute strains that the coupon was experiencing during the monotonic loading. Strains were also computed with finite element software and compared to the DIC-computed strains. DIC strains were 5.6% larger than the finite element computed strains.

3.1.2.1 Specimen Geometry

All specimens were machined from 0.25 inch plate AA 2024-T351, purchased from Aero Specialties Material Corp., Deer Park, NY, 10/6/09. All plates were certified AMS4037/QQA-250/4. The geometry, which conforms at coupon dimensions suggested in ASTM Standard E-08-08, is shown in Figure 2.

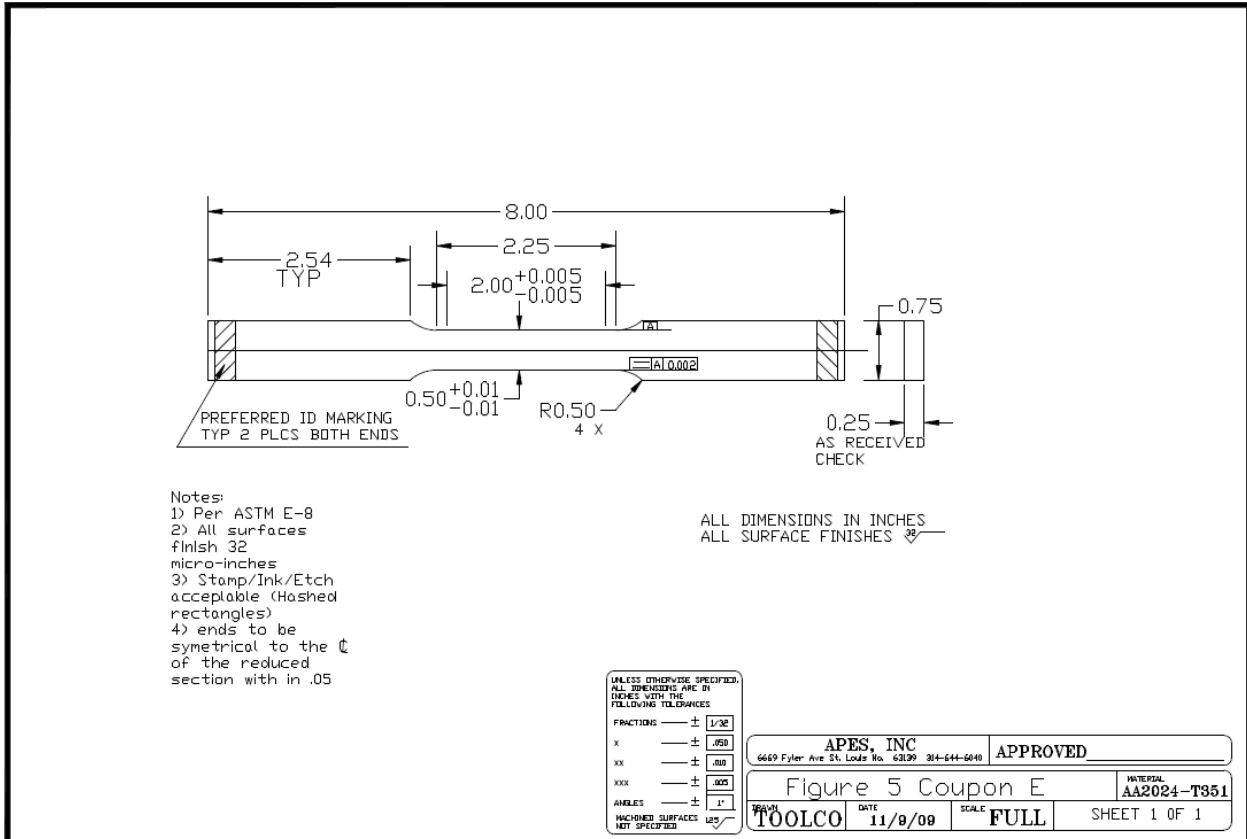


Figure 2. APES Monotonic Stress Strain Coupon

3.1.2.2 Test Standard

The monotonic stress strain curve was measured according the standard ASTM E-08-08, Ref. [5]. The MTS extensometer model 632.13E-20 was used to measure the deformation of the coupon. In addition, digital images were captured using an optical camera to compare the strains computed with the DIC to the strains measured with the extensometer.

3.1.2.3 Results and Discussion

3.1.2.3.1 Extensometer Measured Monotonic Stress Strain

Over two hundred measurements of the displacements on the centerline of the coupon were made with an extensometer. The raw data has been regressed and is shown as the “star” symbols in Figure 3 below. In order to capture the behavior near the ‘knee’ of the stress-strain curve, more points had to be measured in the small strain region than in the large strain region (plotted in Figure 3).

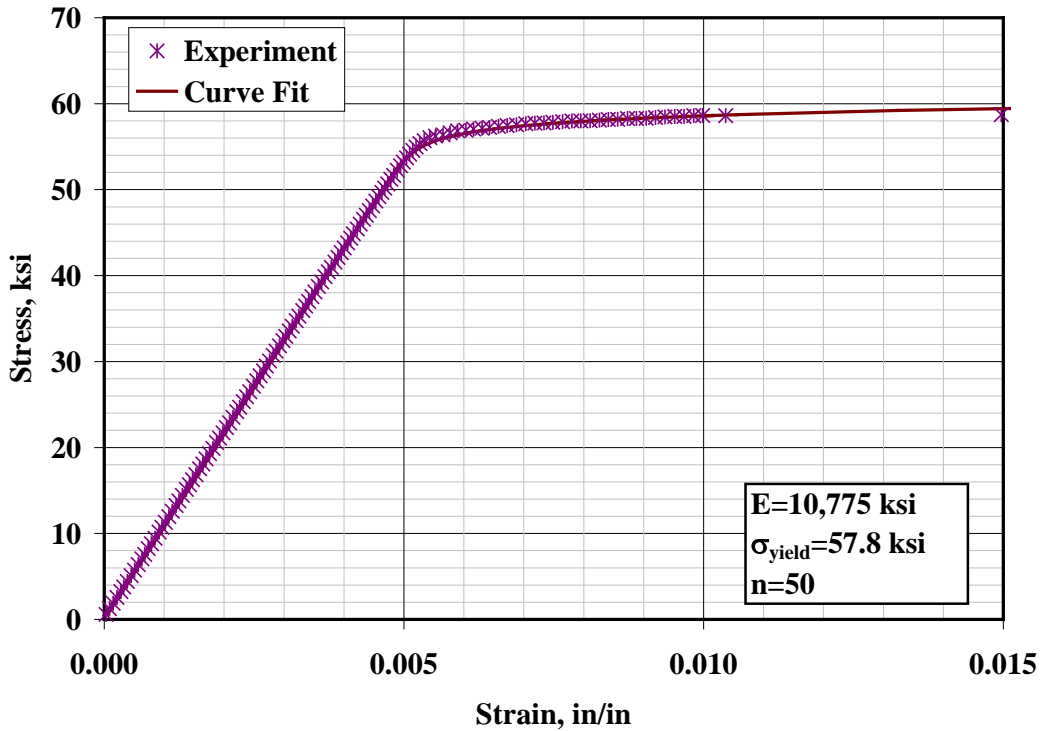


Figure 3. Ramberg Osgood Curve Fit to Small Strain Section of Monotonic Stress Strain Relation

To determine the “Young’s Modulus,” or the slope of the linear region of the curve, the experimental data is curve fit with a linear least squares procedure: starting with the first experimental point (near strain=0 in/in.), a progressively larger number of points is used in the least squares fit, then the Pearson correlation coefficient “ R^2 ” is computed for each sample pool. The maximum correlation coefficient (much less than 99% of the maximum possible, 1.000) is identified and denoted the ‘best fit’ for that particular experimental measurement. The procedure continues for the remaining measured points. The Young’s modulus (the slope of the curve fit) is then the average slope for all curve fits that have correlation coefficient greater than 99.99% (27 data sets in this instance). The resulting Young’s modulus, 10,775 ksi, is used first estimate the 0.2% Yield Stress (per the procedures described in ASTM E-08-08) and then visually curve fit to the experimental data to obtain the power n in the Ramberg-Osgood (AKA “power law”) material stress strain relation, Eq. (1) below:

$$\varepsilon = \frac{\sigma}{E} + 0.002 \left(\frac{\sigma}{\sigma_{yield}} \right)^n \quad (1)$$

which is equivalent to:

$$\varepsilon = \frac{\sigma}{E} + \frac{3}{7} \frac{S_{70E}}{E} \left(\frac{\sigma}{S_{70E}} \right)^n \quad (2)$$

if

$$\sigma_{yield} = \left(\frac{7}{3} 0.002 E \right)^{1/n} (S_{70E})^{(n-1)/n} \quad (3)$$

The visual curve fit of the experimental data is the solid line in Figure 3 above for the small strain region. The Yield Stress, 57.8 ksi, is much higher than the Yield Stress in MIL-HDBK-5H, which is closer to 48-50 ksi (Table 3.2.3.0 (b₁)) for A and B-basis, respectively Ref. [6]. Note that the Yield Stress is calculated from the intersection of the line with slope of E (10,775 ksi) which crosses the $\sigma = 0$ ksi plane at $\varepsilon = 0.002$ in/in with the experimentally measured stress-strain data. The power law coefficient, n (50) is the same as the coefficient in the MIL-HDBK-5H Ramberg Osgood curve, Figure 3.2.3.1.6(b).

If you want the Ramberg-Osgood (AKA “power law”) curve fit coefficients to be useful over the entire range of strain that is important to your problem, then you might have to compute the Ramberg-Osgood coefficients appropriate to your particular strain range. For instance, the coefficients $(\sigma_{yield}, n) = (57.8$ ksi, 50) work well in the small strain region (Figure 3), while work poorly for fitting the large strain region, Figure 4. For a better fit through 0.1 in/in., the coefficients $(\sigma_{yield}, n) = (53$ ksi, 15) appear to work better than $(\sigma_{yield}, n) = (57.8$ ksi, 50).

Three (3) more monotonic stress strain curves were measured, on coupons 2E03 and 2E04, and are presented along with the above Figure 4 data (which is for coupon 2E01) in Figure 5. The data are consistent except at the all-important knee near the yield stress, approximately 58 ksi. The MIL-HDBK-5 curve fit is included for comparison—the MIL 5 data has curve fit parameters of $(E, \sigma_{yield}, n) = (10,700$ ksi, 48 ksi, 50), substantially smaller (20%) yield stress than measured here.

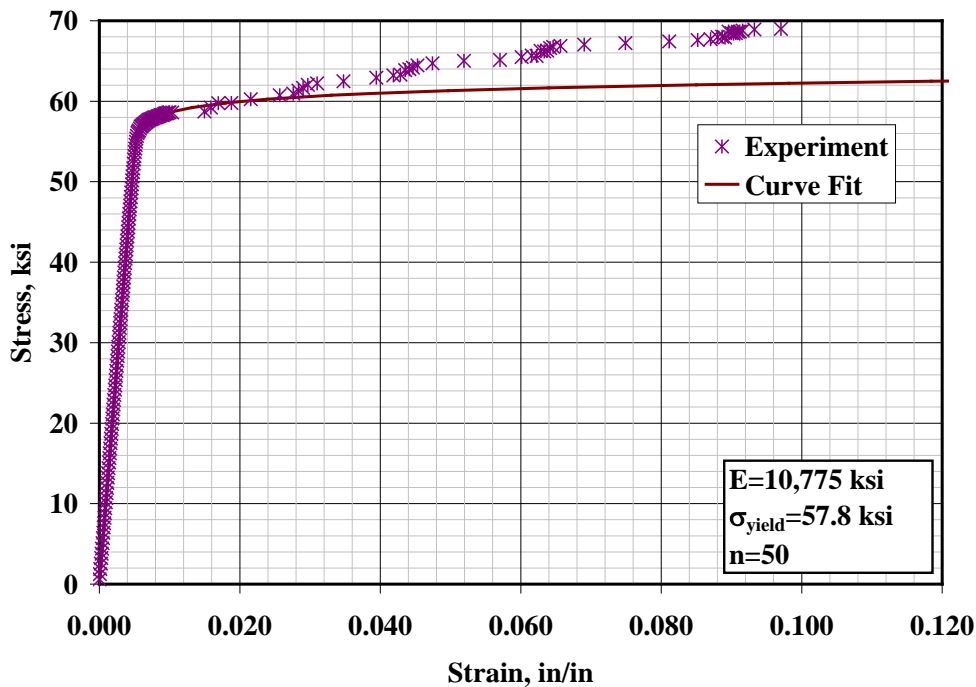


Figure 4. Ramberg Osgood Curve Fit to Large Strain Section of Monotonic Stress Strain Relation

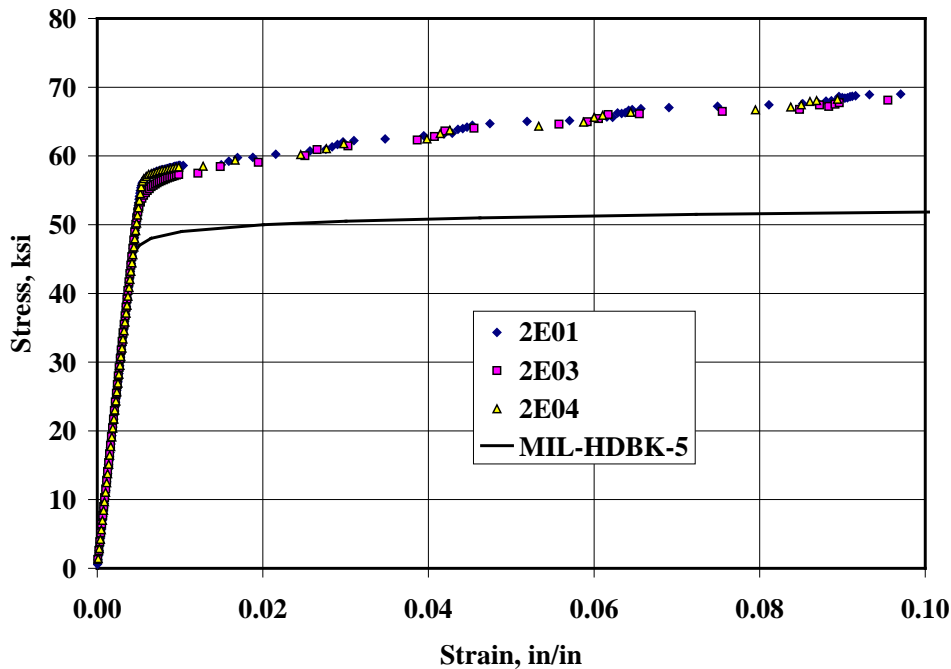


Figure 5. Monotonic Stress Strain Measurements Compared to MIL-HDBK-5 Curve Fits
Table 1 summarizes the curve fits for the monotonic stress strain tests.

Table 1. Summary of Elastic and Plastic Constants

Coupon	Young's Modulus, ksi	0.2% Yield Stress, ksi	0.2% Yield Strain, in/in	70%E Stress, ksi	Power, n
2E01	10,775	57.80	0.007362	57.93	62
2E03	10,696	56.20	0.007245	56.36	42
2E04	10,405	57.88	0.007560	58.05	60

3.1.2.3.2 DIC Measured Monotonic Stress Strain

ASTM E-8 specimen 2E01 was speckle painted and digital images were captured every 2 seconds during the E-8 test. Strain near the central part of the specimen's gage section could not be computed with VIC-2D due to the presence of the wooden backing block for the extensometer that is necessary to provide the knife edge clamping force. Figure 6 (left) shows the test setup, the backing block and springs that hold the extensometer and the two Areas-Of-Interest (AOI) used for image correlation. The upper AOI is selected and is red, the lower AOI is shown in light blue. Figure 6 (right) shows the VIC-2D computed ε_{y-y} strain contours (smoothed at filter size = 35) at a load of 6.365 kips and a gage section nominal stress of 50.3 ksi, slightly less than yield. The theoretical elastic strain value at this stress is 0.00467 in/in. There appear to be some localized AOI edge effects near the wooden backing block, so strain statistics were computed for the two rectangular regions shown in Figure 6. The rectangles start just inside the gage section of the specimen. Table 2 shows the results, and shows the statistical variation on the strain based on the entirety of the two AOI's.

Table 2. Average Strain in Load Direction

Location	Mean strain, μ_{strain} (inches/inch)	Standard Deviation, σ (inches/inch)	Theoretical difference
Upper rectangle	0.004894	0.0001135	+ 4.80%
Lower Rectangle	0.004874	0.0001808	+ 4.37%
Entire AOI	0.004652	0.0004191	- 0.385%

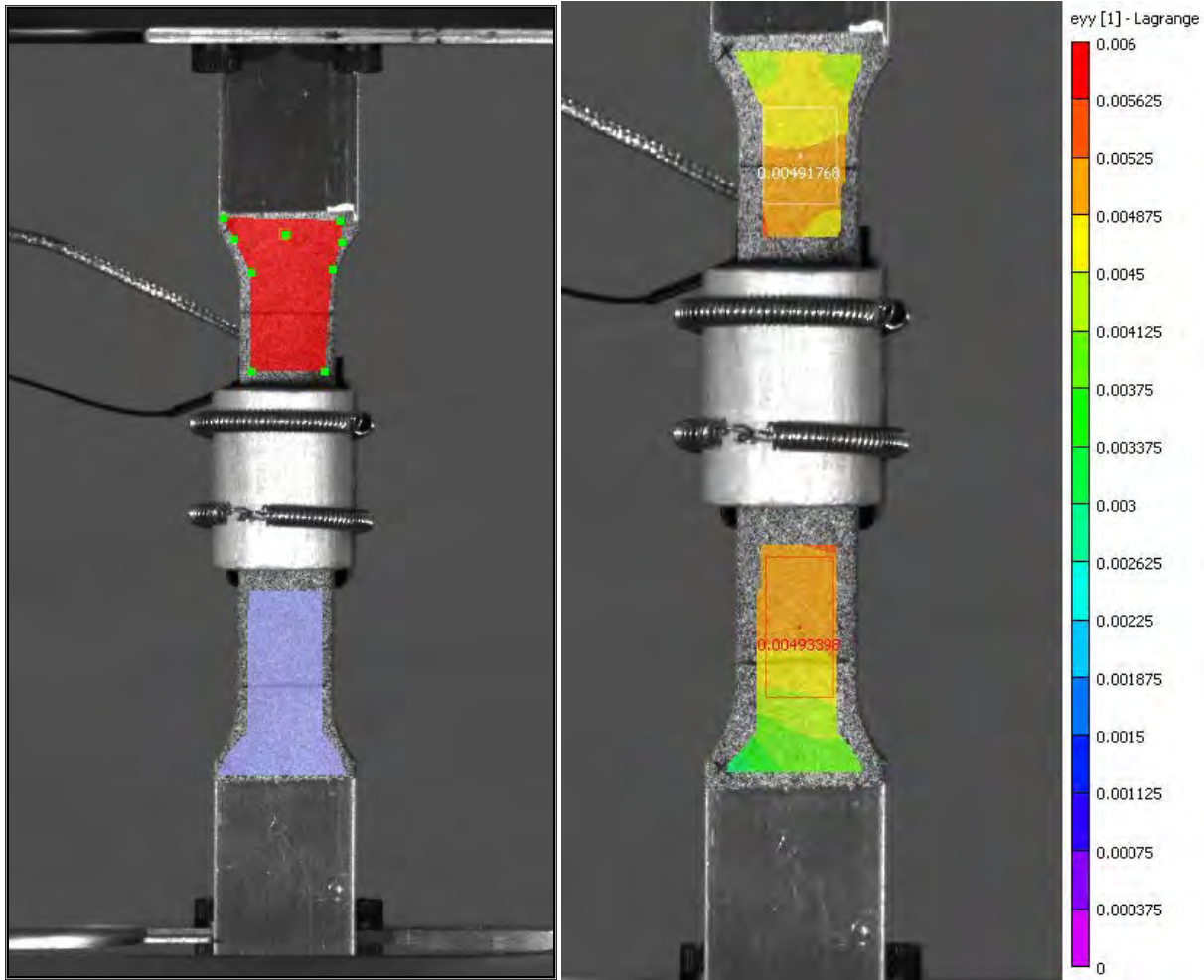


Figure 6. DIC Computed (Lagrangian) Strains

3.1.2.3.3 Finite Element Simulations

The Ramberg-Osgood material coefficients $(\sigma_{\text{yield}}, n) = (57.8 \text{ ksi}, 50)$ are used to describe a nonlinear plastic material constitutive relation in the p -version finite element software StressCheck. The FE model simulates a plane stress dogbone coupon with a constant displacement δ_{end} applied to one end, Figure 7.

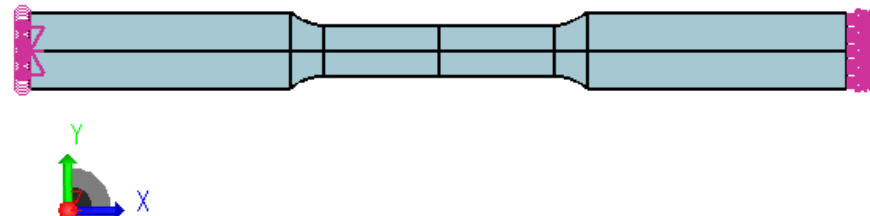


Figure 7. StressCheck FE Model

The axial stress contour is plotted for an end displacement of $\delta_{end} = 0.029 \text{ in.}$ in Figure 8. The maximum stress $\sigma_{xx} = 56.55 \text{ ksi.}$ is close to the input yield stress 57.8 ksi. The gage stress (based on the un-deformed section) is $\sigma_{gage} = 6.295 \text{ kips}/(0.5002 \text{ in.} \cdot 0.2528 \text{ in.}) = 49.78 \text{ ksi.}$ The axial strain contours are plotted for the same end displacement of $\delta_{end} = 0.029 \text{ in.}$ in Figure 9 for direct comparison to the DIC computed contours.

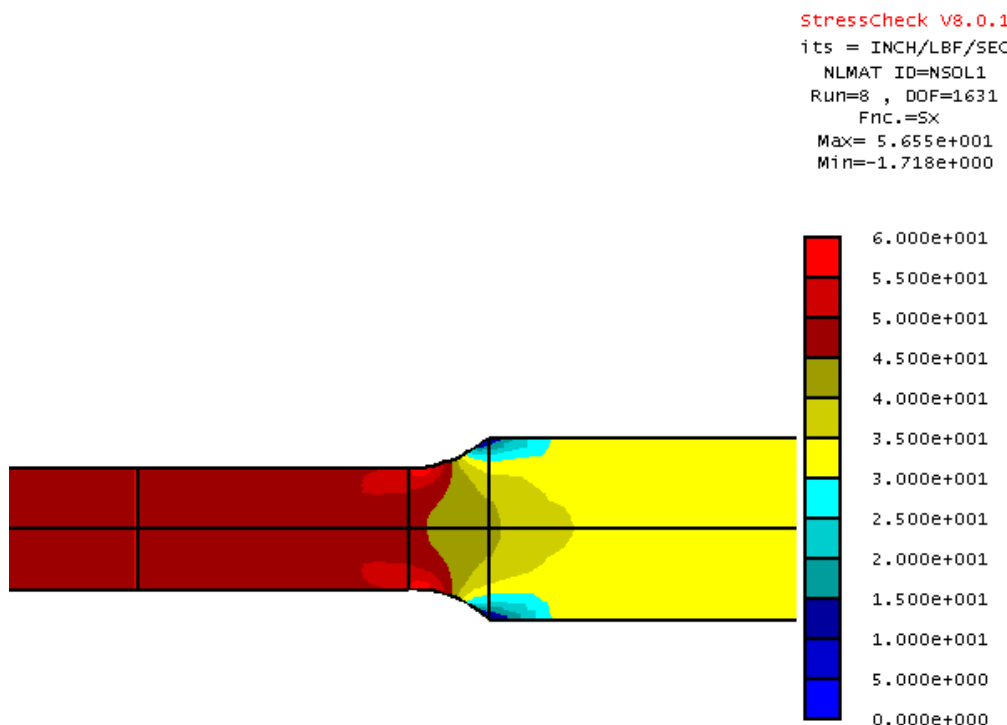


Figure 8. Normal Stress (Load Direction), $\delta_{end} = 0.029 \text{ in.}$ DIC image shown for reference

The normal strain and stress at the middle of the gage section is computed and compared to the theoretical value in Table 3.

Table 3. Average Engineering Quantities in Load (Axial) Direction.

	Units	Computed	Theoretical	Difference, %
Mean stress	ksi	49.776	49.782	0.012
Mean strain	in./in.	0.004621	0.004620	-0.014

The FE computed strain, 0.004621 in/in, is 5.6% less than the DIC computed strain, 0.004894 in/in.

3.1.2.4 Comparison to Other Results

The correlation of the DIC to the expected strains in the present results are compared to DIC correlations in a Colorado University report by Cintron and Saouma, Ref. [7]. In this NEES report, Cintron and Saouma used DIC on aluminum or brick and mortar specimens. They did not identify the particular aluminum alloy, but did state that the Young's modulus was 70 GPa (10,153 ksi). Coupons of two sizes , 1.0x1.0x1.0 in. and 1.3x1.5x1.0 in., were compressed with gradually increasing loads. The theoretical strain (the applied stress divided by the Young's modulus) was compared at several load levels to the DIC strain computations. Stresses were well below yield stress for this material (which could be from 45 to 80 ksi), being on the order of 25 ksi. The results were not good—their DIC strains were anywhere from 20 to 500% larger than the strains predicted from the linear elastic model. Surprising too was the large difference in strains as measured on the surfaces of the two coupon sizes—the small blocks (1x1x1) produced strains 500% larger than the predicted strains, while the large blocks (1.3x1.5x1.0) produced strains 25% larger than predicted, an order of magnitude difference.

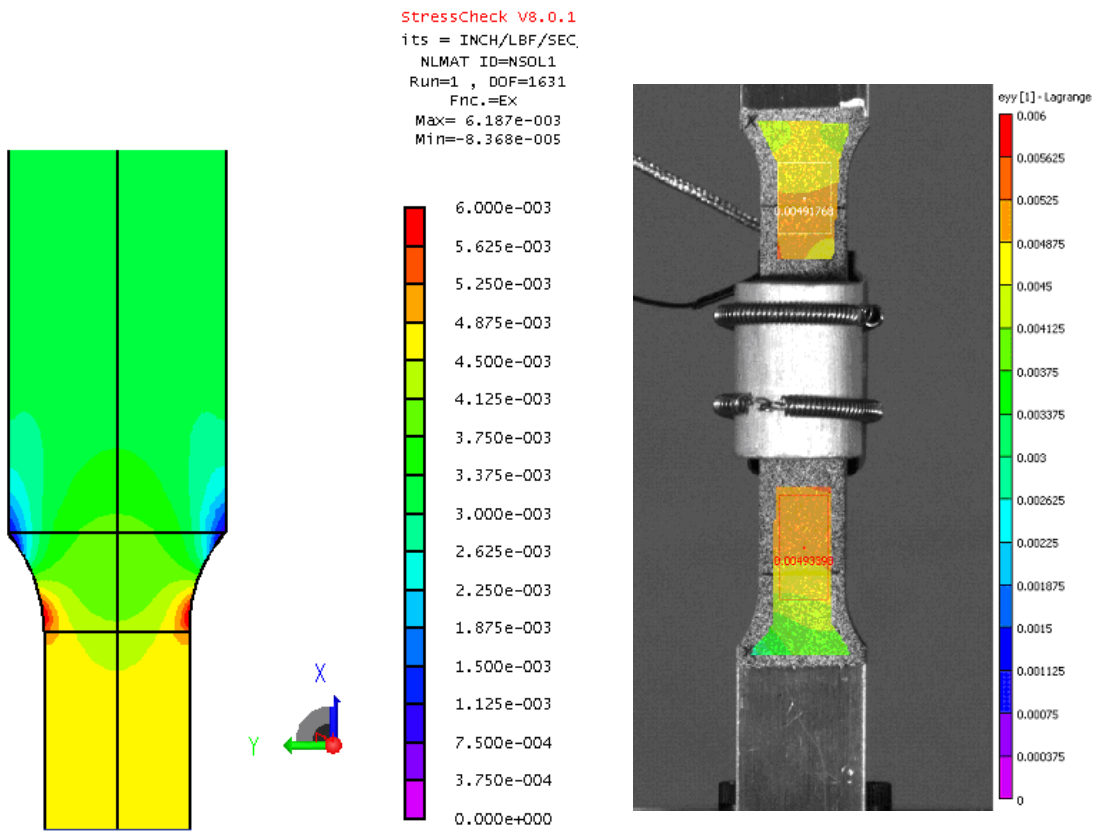


Figure 9. Normal Strain (Load Direction), $\delta_{end} = 0.029 \text{ in.}$

3.1.2.5 Cold Working Simulations

An important question to answer is, “what differences do the relative values of the material constitutive parameters make?” If the residual stresses due to cold working are to be computed with finite elements or some other numerical method, a key input is the particular material constitutive relation (stress vs. strain) and the magnitudes of the parameters in that constitutive relation. All finite element simulations here are performed with the p -version FEA software StressCheck, which requires the material to be described by either the Ramberg-Osgood (R-O, aka “power law”) plasticity curve or a bilinear plasticity curve. Both plasticity curves use 3 parameters to define the respective curves: Ramberg-Osgood uses Young’s modulus, yield stress and the power law, while the bilinear plasticity curve uses Young’s modulus, tangent modulus, and yield stress. Figure 9 below shows both material curve types, as well as some experimental measurements. If no actual data exists, open sources such as MIL-HDBK-5, which has “typical” Ramberg Osgood parameters, must be relied upon. If actual data exists, then the experimental data can be fit with either or both of these two curve fits.

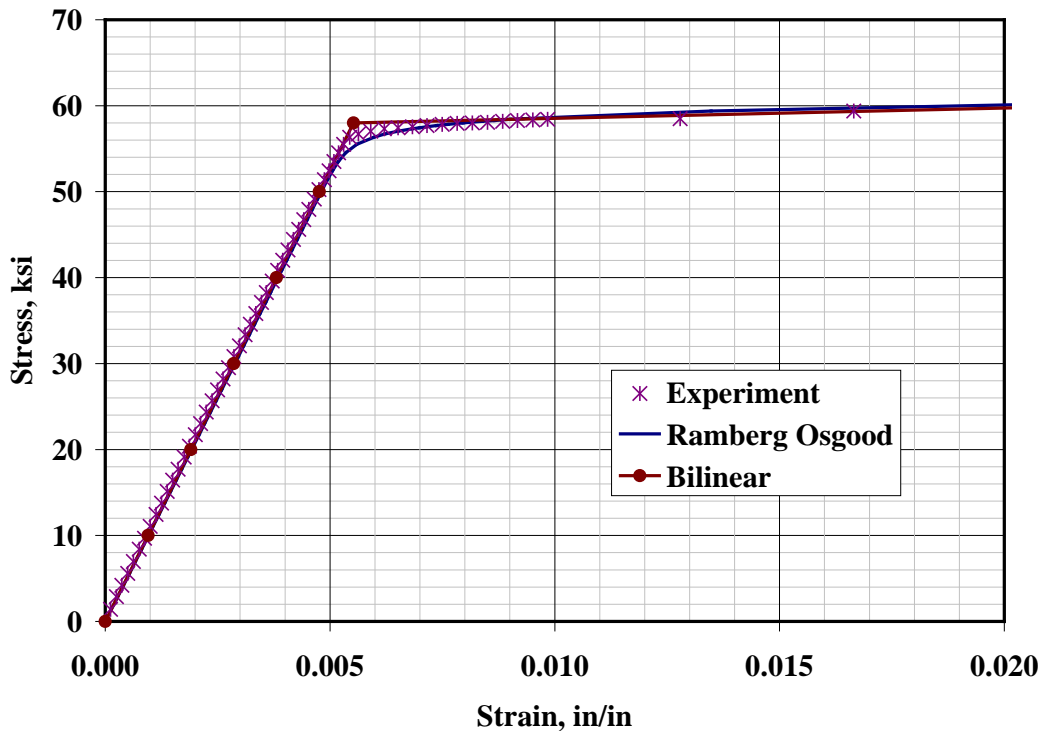


Figure 9. Comparison of Two Plasticity Constitutive Relations (Ramberg Osgood and Bilinear) to Experimentally Measured Monotonic Stress-Strain Measurements

A possible method for estimating the difference due to the material parameters is to complete FEA simulations for a structure being loaded plastically, such as a cold worked hole, and compute the residual stresses that remain after the hole has been plastically deformed for two or more material constitutive relations. The cold working of holes in plates made of two different materials was simulated. Both materials are defined with Ramberg-Osgood plasticity relations: Material 1 uses the R-O fits in MIL-HDBK-5 for AA2024-T351, Material 2 uses the R-O fits of the experimentally measured monotonic stress-strain curves in the current project. The magnitudes of the R-O parameters for each material are summarized in Table 4 below.

Table 4. Material Constitutive Parameters for Two Ramberg-Osgood Plasticity Relations

Material	Source	Young's Modulus, ksi	Yield Stress, ksi	Power law coefficient, n
1	MIL-HDBK-5	10,700	48.0	50
2	CX Add-on MSS	10,775	57.8	50

The MIL-HDBK-5 (Material 1) Ramberg-Osgood curve fit is plotted against the experimental data in Figure 10 below, while the CX Add-on MSS (Material 2) Ramberg Osgood curve fits are plotted against the experimental data in Figure 9 above.

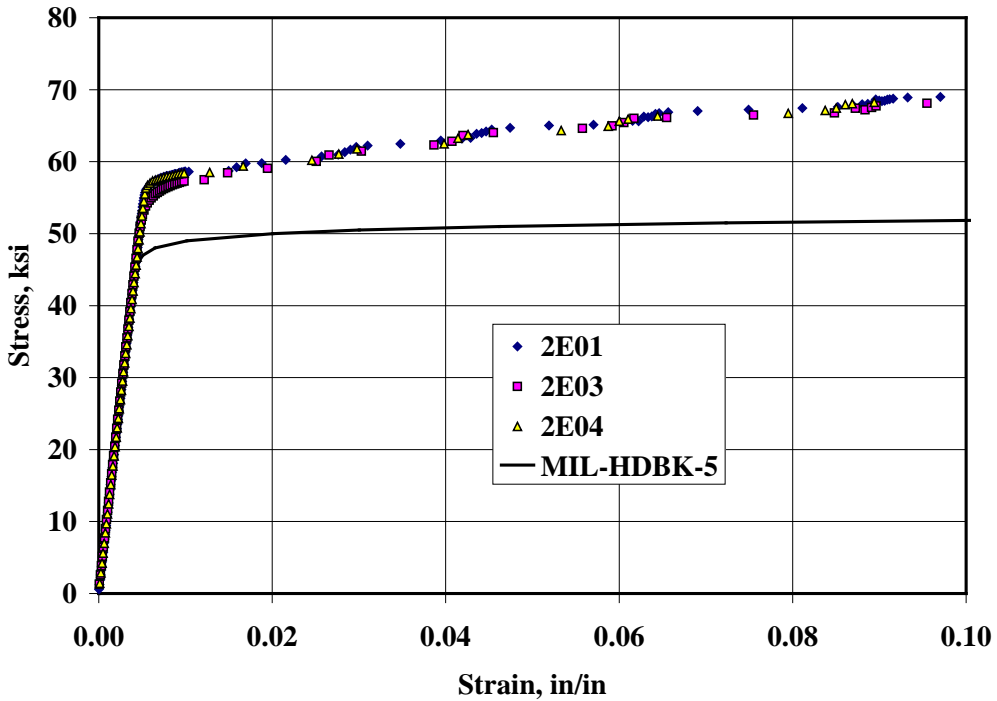


Figure 10. MIL-HDBK-5 Ramberg Osgood Material Curve Compared to Experimental Data

Each material was used to simulate nominal 4% cold working of a hole in a plate, Figure 11. The simulation used a relatively stiff pin to simulate the mandrel insertion, and then the pin is forced to become almost limp to simulate the mandrel removal. As the mandrel is inserted, the stresses in the plate become plastic; when the mandrel is removed, the elastic material in the plate pushes back on the plastic region around the hole, possibly resulting in large compressive tangential stresses close to the hole, Figure 12, which shows the variations of those residual stresses that are due to the variations in the Ramberg-Osgood material parameters. Material 1 is marked “MIL-5” in the Legend, Material 2 is marked “Current” in the Legend.

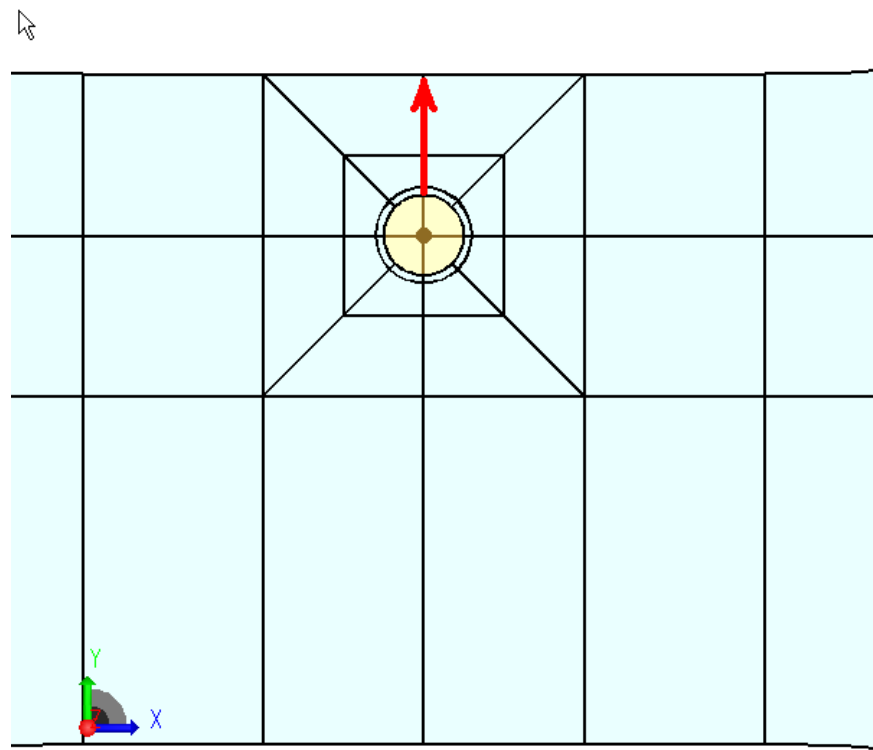


Figure 11. Close Up of Cold Worked Hole in FE Simulation. Arrow Shows Direction That Residual Stress Computed in Figure 12 Below

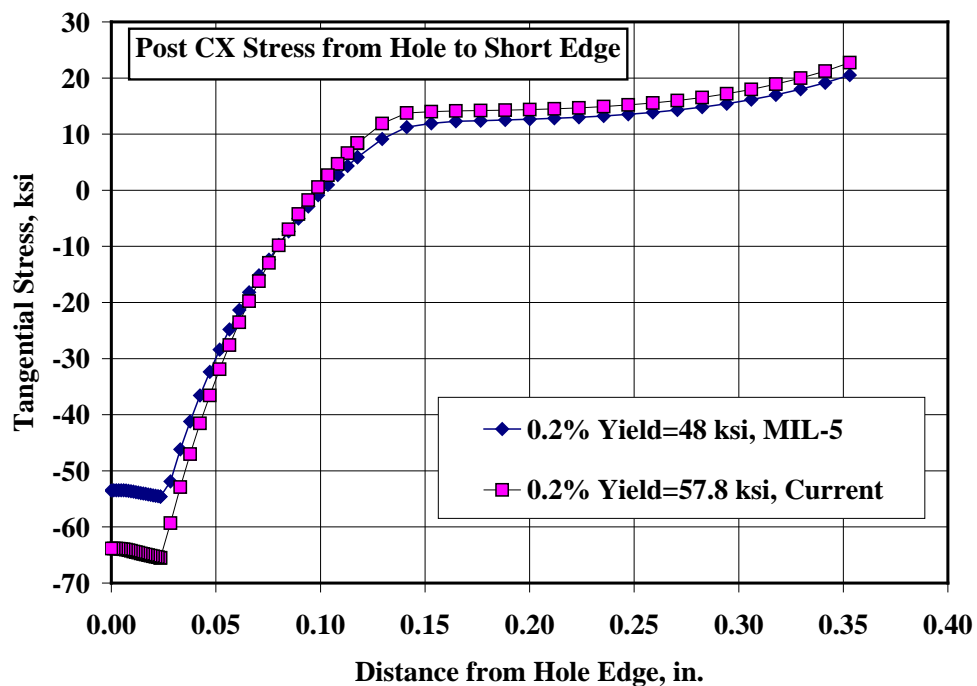


Figure 12. Residual Stresses, Cold Working Simulations with the Two Plasticity Models

The biggest difference between Materials 1 and 2 is the yield stress: Material 1's yield stress is 17% less than Material 2's yield stress—the difference is quite evident near the hole edge, at $x=0$ in Figure 12. Material 1's residual stress decreases as the hole edge is approached, up to 0.02354 in. from the hole edge, down to -54.6 ksi, then starts to increase, finally attaining -53.5 ksi right at the hole edge. Material 2's residual stress decreases as the hole edge is approached, up to 0.02236 in. from the hole edge, down to -65.5 ksi, then starts to increase, finally attaining -63.9 ksi right at the hole edge. Material 2 clearly has a much larger (in magnitude) compressive stress at the hole edge, which typically is the region where cracks will form in a cold worked plate. The result should be a much slower growing crack in Material 2 than in Material 1.

3.1.2.6 Conclusions

The monotonic stress strain behavior of Aluminum Alloy 2024-T351 was measured and reduced using ASTM E-08.08 procedures. Digital Image Correlation (DIC) was used to measure displacements and compute strains that the coupon was experiencing during the monotonic loading. Strains were also computed with Finite element software and compared to the DIC computed strains. DIC strains were 5.6% larger than the Finite element computed strains. These findings should be further pursued. The importance of having the particular monotonic data for the material batch of concern, as opposed to handbook generic properties, has been assessed in relation to their influence residual stress computations.

3.1.3 Test: Fracture Toughness (K_{Ic}) (ASTM E-399)

The fracture toughness of 1 in. thick Aluminum Alloy 2024-T351 was measured using ASTM E-399 protocol (Ref. [8]) on a 22 kip MTS machine. These tests were used to ensure that the aluminum from the supplier used for cold work testing did not exhibit anomalies in terms of the industry-standard, expected fracture toughness values for K_{Ic} , the plane strain fracture toughness.

3.1.3.1 Specimen Geometry

All specimens were machined from 1.0 inch plate AA 2024-T351, purchased from Aero Specialties Material Corp., Deer Park, NY, 10/6/09. All plates were certified AMS4037/QQA-250/4. The geometry, which conforms at coupon dimensions suggested in ASTM Standard E-399, is shown in Figure 13.

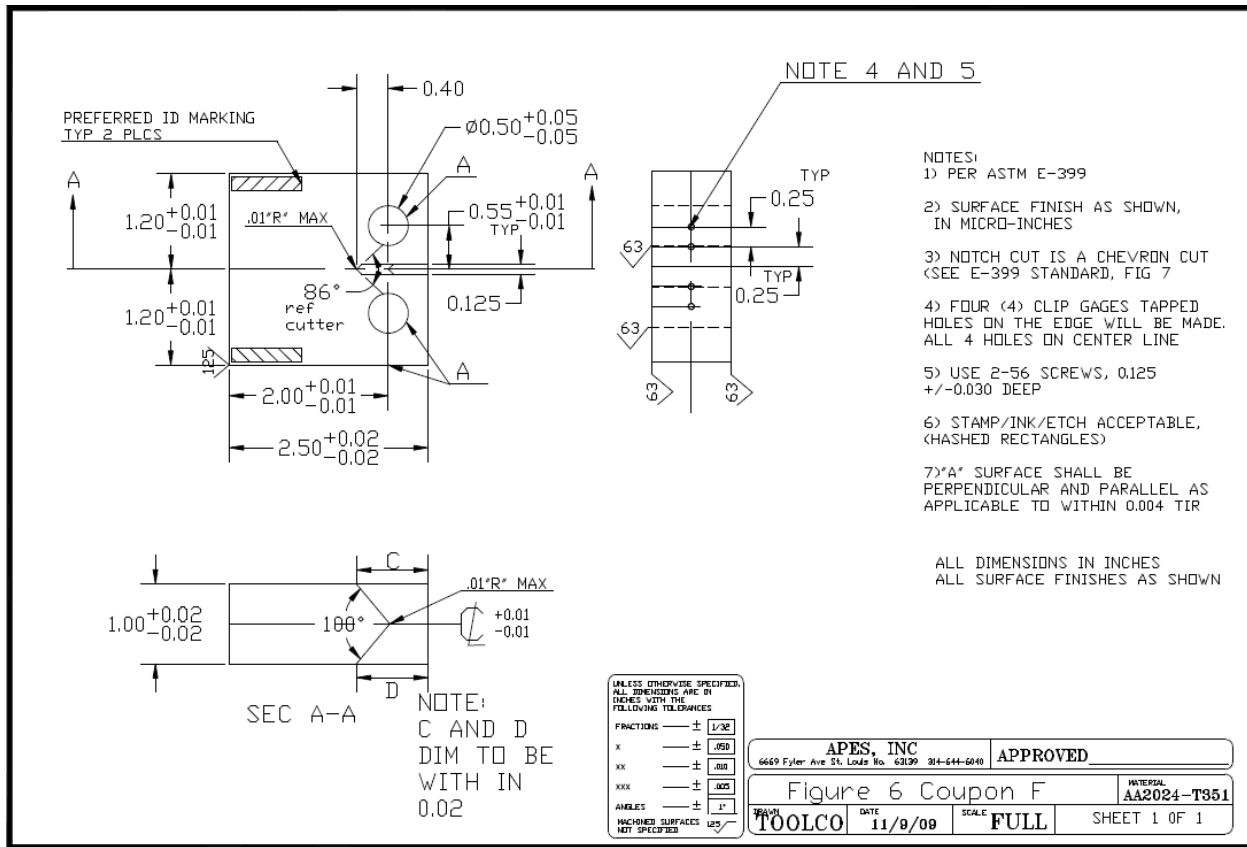


Figure 13. APES Fracture Toughness Coupon

3.1.3.2 Test Standard

The fracture toughness was measured according the standard ASTM E-399.

3.1.3.3 Results and Discussion

Fracture toughness values K_{lc} and average crack length values a for the four specimens are reported in Table 5 below. Further details are presented in the test reports for the individual specimens.

Table 5. E 399-08 Specimen Test Results

Specimen	a (inch)	P_{max} / P_Q	K_{lc} (ksi-sqrt-inch)
2F01	1.027	1.087	33.99
2F02	1.000	1.098	33.74
2F03	1.028	1.097	33.94
2F04	1.027	1.097	33.69

Note the values in the column for P_{max} / P_Q . The E-399 specification states that, among other checks, this ratio must be less than 1.1 in order for the test to be a valid K_{lc} test. The closeness of this entire column to the limiting factor of 1.1 brings up a matter that we recommend be taken up with the ASTM standards committee for possible revision and/or clarification. The E-399

procedure for determining P_Q states that a line should be drawn tangent to “the initial linear portion of the record.” This tangency line then has its slope multiplied by a 0.95 factor to construct a second line that is, in general, used to compute P_Q at the location where the second line intersects the autographic data record. Nowhere is the ‘initial linear portion of the record’ defined. The standard states that ‘slight initial nonlinearity of the record’ occurs frequently and is to be ignored, but no further instructions are given. Note: it is apparent through our discussions with other E-399 mechanical testers (US Naval Academy and UC-Davis researchers) that the E-399 is not a very reliable test, and that the J-integral test (ASTM E-1820, Ref. [9]) is more reliable and which results should be used to compute the fracture toughness here.

The problem with an undefined “initial linear portion of the record” is illustrated here for the test results of only one coupon. Figure 14 shows the autographic record for specimen 2F01. All four specimens in Table 5 exhibited similar behavior, in that the autographic data record is convex throughout the entire region from 0 kips through 4 or 4.5 kips. Four different initial tangency lines A, B, C, and D were drawn through this data record (they are not shown on Figure 14 for clarity) by computing the best-fit slope of all data points (A) from 0 kips to 1 kip, (B) from 0 kips to 2 kips, (C) from 0 kips to 3 kips, and (D) from 0 kips to 4 kips. Per the ASTM E-399 standard, 95% of each of these slopes was then used to draw the four lines of Figure 14 through the (0,0) origin. As can be seen from the inset of Figure 14, each line results in a different value for P_Q . Table 6 shows the results of each of these four scenarios in computing K_{Ic} .

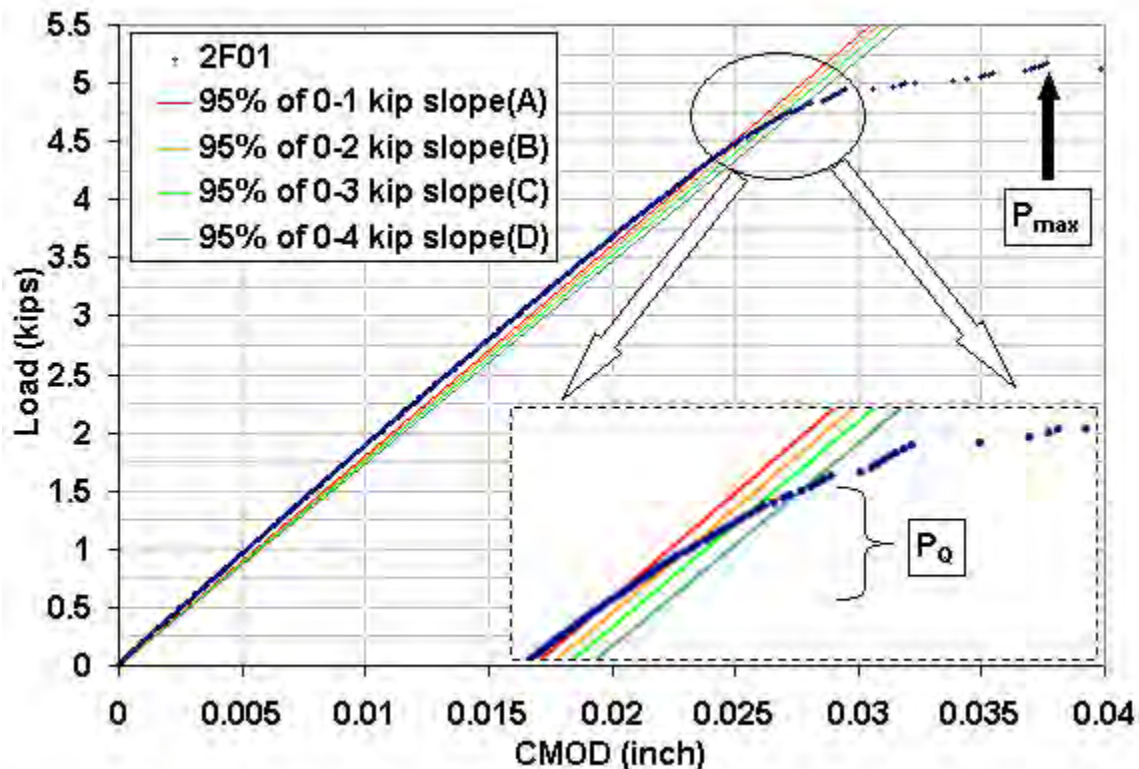


Figure 14. Four 95% Slope Curves and Their Varied P_Q Intersections, Computed From Four Different Initial Tangencies

Table 6. Results of Four Tangency Scenarios for Specimen 2F01. $P_{max} = 5.17$ kips

Scenario	2F01 Data Used	$P_Q (=P_5)$ (kips)	P_{max} / P_Q	Valid Test?
Tangency A	< 1.0 kips	4.42	1.17	NO
Tangency B	< 2.0 kips	4.6	1.12	NO
Tangency C	< 3.0 kips	4.71	1.10	YES
Tangency D	< 4.0 kips	4.81	1.07	YES

3.1.3.4 Conclusions

The fracture toughness of 1.0 in. thick Aluminum Alloy 2024-T351 was measured and reduced using ASTM E-399 procedures. The method for computing the tangency line of “the initial linear portion of the record” can be a challenge, as the validity of the test is based on what appears to be a reasonable guess as to the value of this “initial linear portion.” All four specimens exhibited similar behavior to 2F01, in the sense that none of the tests would have been deemed valid if only data <1 kip or <2 kips were used to construct the tangency. It may be true that this issue has only recently arisen due to modern autographic computer recording techniques where it is simple to capture data at very high frequencies (10 Hz was used in this test), however a few simple tests of this theory that intentionally reduced the number of data points were inconclusive.

4 Modeling Fatigue in Cold-worked Holes

4.1 Test: Open Hole, Non Cx Fatigue Tests (Part of Task 1)

The fatigue lives of the centered hole (non Cold Work) specimens tested in this program were predicted before any fatigue tests were completed; this exercise serves as a reference, a study of the our best analysis models for predicting cold working effects in mid-2010. Though the specimens in this program were tested only at 25 ksi, life predictions over a range of applied stresses were made.

4.1.1 Specimen Geometry

All specimens were machined from 0.25 inch plate, purchased from Aero Specialties Material Corp., Deer Park, NY, 10/6/09. All plates were certified AMS4037/QQA-250/4. In addition to the geometry shown in Figure 15, there is a 0.25 inch diameter hole drilled into the center of each coupon (drill plus ream without cold work.).

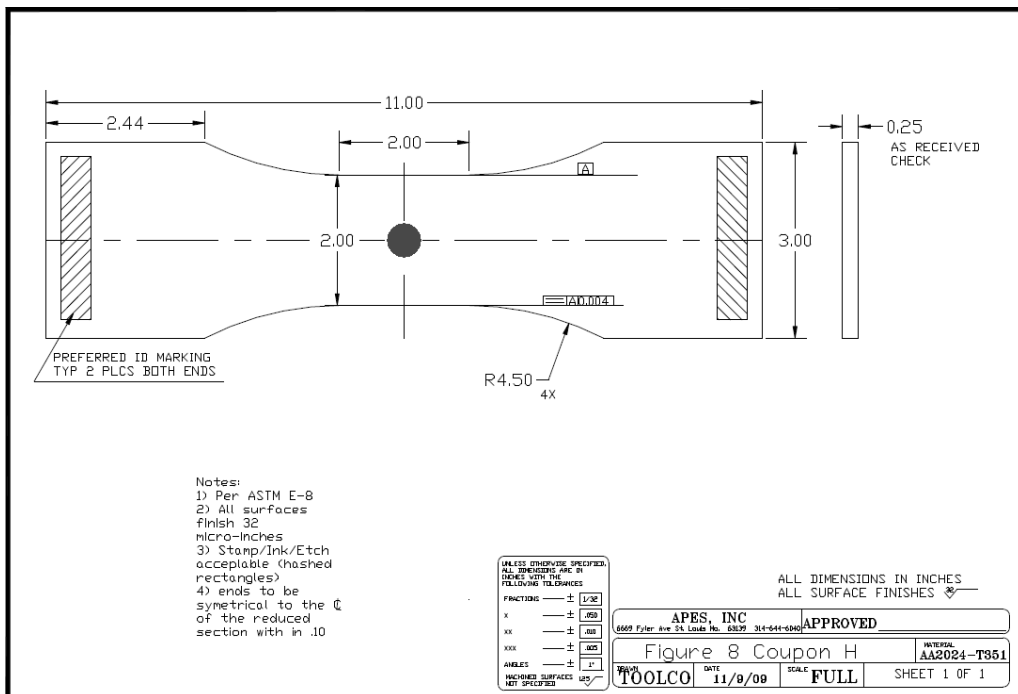


Figure 15. APES Cold Work Specimen Geometry

4.1.2 Material

All specimens were manufactured from 0.25 inch Aluminum Alloy 2024-T351 plate. Two types of data are needed to perform a crack growth prediction: initial discontinuity states (the distribution of expected initial flaw sizes) and the material crack growth rates. The sources of these two data types and the magnitudes of the corresponding data types are discussed below.

4.1.2.1 Initial Discontinuity State

The distribution of Initial Discontinuity States (IDS) were obtained in the APES DUST program through a subcontract with NRC-Canada, Ref. [10]. NRC-Canada completed a fatigue test

program of 19 coupons, and measured the size of the ‘failure flaws’ on each coupon; their findings are summarized in NRC-C report, Ref. [11]. The NRC-C coupon geometry is shown in Figure 16.

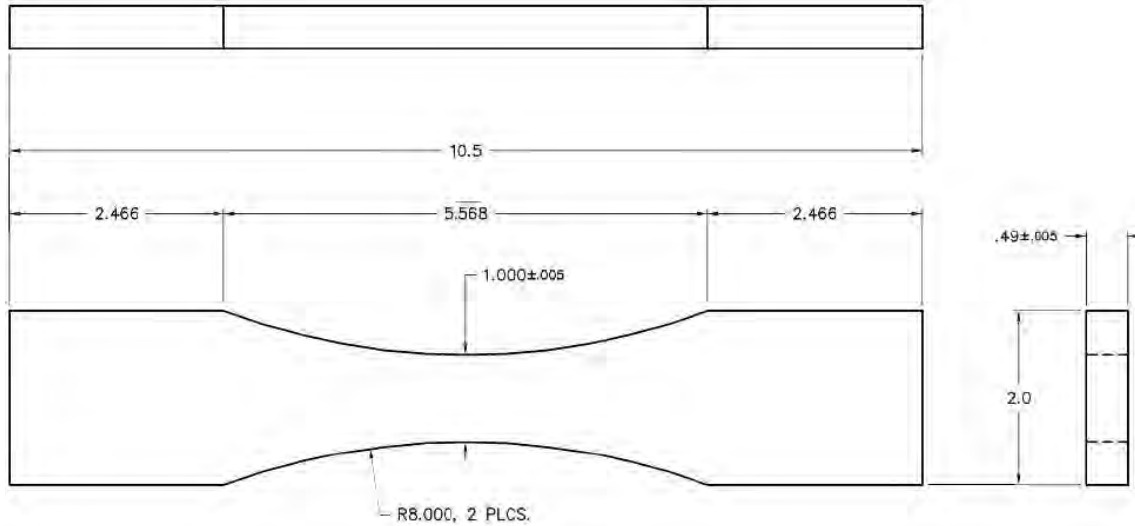


Figure 16. NRC-C Specimen Geometry. All dimensions in inches

NRC-C fatigued to failure 15 coupons aligned in L direction and 4 coupons in T direction. Five (5) coupons each were loaded with 40 ksi, 44 ksi, and 48 ksi (net section stress). In the T direction, 2 coupons each at 40 ksi and 48 ksi were fatigued to failure. Subsequently, the “failure flaws” were measured on each fracture surface. In all tests but one, the failure flaw occurred on the 0.5-inch edge in the net section; one failure flaw occurred on the top of the coupon, in the 1 inch width of the net section.

The fatigue cycles to failure along with the measured failure flaws (called IDS) were used in an IDS-MACS matching procedure that requires the tuning of a material crack growth rate to the IDS distribution. The procedure is roughly the following: 1) Read the “best choice” material crack growth rate (CGR) and load spectrum into the appropriate AFGROW crack growth model, and 2) compute the Matched Analytical Crack Size (MACS) by making a succession of AFGROW predictions—run AFGROW simulation with a initial crack size ‘guess,’ compare to the experimentally measured number of cycles to failure, and adjust the initial crack size lower (higher) if the AFGROW computed failure is lower (higher) than the experimental cycles to failure. The entire MACS distribution is then compared to the entire, experimentally measured IDS—if there is a ‘significant’ difference between the two distributions, the CGRs are adjusted (in ΔK regions below 3 ksi-in $^{0.5}$) and the new MACS distribution computed. The tuning continues until the MACS and IDS roughly match. The resulting distribution is summarized in Table 7 below.

Table 7. Distribution of Initial Discontinuity State (IDS)

Cumulative Distribution Function (CDF)	Computed MACS, in.	Measured IDS, in.	Cumulative Distribution Function (CDF)	Computed MACS, in.	Measured IDS, in.
0.026316	0.000603	0.000289	0.552632	0.000960	0.000985
0.078947	0.000613	0.000495	0.605263	0.000990	0.000991
0.131579	0.000762	0.000536	0.657895	0.001018	0.001027
0.184211	0.000813	0.000703	0.710526	0.001049	0.001057
0.236842	0.000815	0.000751	0.763158	0.001059	0.001174
0.289474	0.000824	0.000758	0.815789	0.001173	0.001186
0.342105	0.000915	0.000897	0.868421	0.001376	0.001198
0.394737	0.000921	0.000962	0.921053	0.001419	0.001298
0.447368	0.000930	0.000967	0.973684	0.001872	0.001452
0.500000	0.000959	0.000985			

The distribution in Table 7 can then be used to compute the probabilistic distribution of fatigue lives for other stresses and crack scenarios. For the analyses summarized in this report, fatigue life predictions are made with the 10th, 50th, and 90th percentile IDS, Table 8.

Table 8. Initial Discontinuity States Used in Fatigue Life Predictions

CDF (P)	IDS, in.
0.10	0.000673
0.50	0.000959
0.90	0.001402

A histogram of the MACS computed data in Table 7 is shown in Figure 17 below. The MACS display a narrow band around MACS=0.00105 in. In Figure 17, the bin sizes are constant at 0.0001 in.; the abscissa (EIFS, in.) value represents the median of the bin—for instance, the value of 0.32 in the 0.00105 in. bin means that 32% of the computed MACS for the 19 coupons fell between 0.0010 and 0.0011 in. The mean of the 19 EIFS computations was 0.0010 in.; the coefficient of variance 30%.

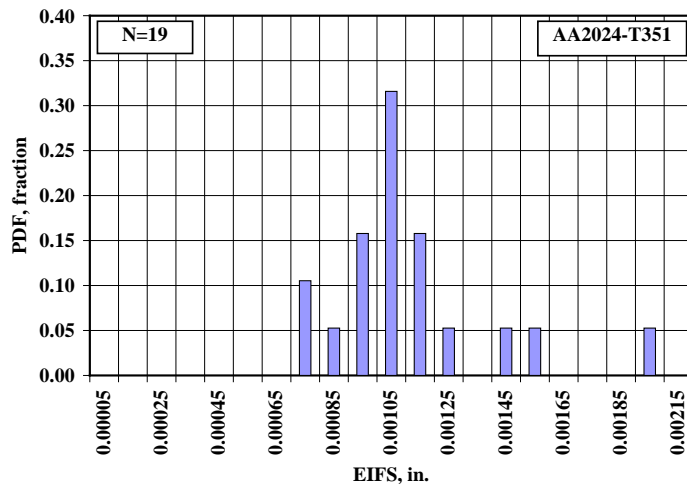


Figure 17. MACS Probability Density Function (Histogram)

4.1.2.2 Material Crack Growth Rates

The final ‘tuned’ material crack growth rates obtained in the MACS-IDS matching procedure briefly described above are used in the fatigue life predictions summarized in this report. Only the $R = 0$ and $R = 0.5$ CGRs are shown in Figure 18 below.

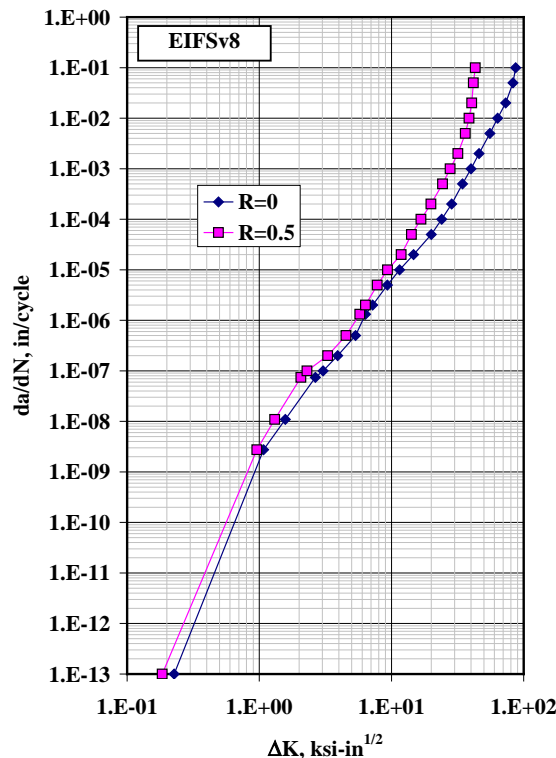


Figure 18. Crack Growth Rates, AA2024-T351. EIFSv8.lkp

4.1.3 AFGROW Crack Model

The CX Plus-Up test coupon is a centered, open hole; therefore, the AFGROW crack growth model Single Corner Crack at Hole is used in these predictions, Figure 19. The load spectrum is constant amplitude (CA), $R = 0$.

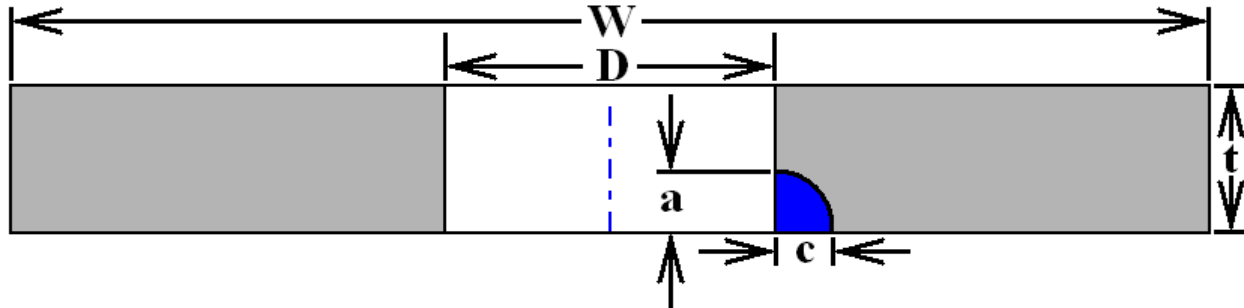


Figure 19. Fatigue Crack Scenario

4.1.4 Results and Discussion

4.1.4.1 Fatigue Life Predictions

The fatigue life predictions for open hole specimens are shown in Figure 20 and Figure 21. In Figure 20, fatigue lives were computed for a spectrum of IDS: 1) IDS ($P=0.1$)=0.00067 in., 2) IDS ($P=0.5$)=0.00096 in., and 3) IDS ($P=0.9$)=0.0014 in. In Figure 20, in addition to the IDS used in Figure 20, fatigue lives were computed for four (4) additional IDS: 1) IDS=0.005 in., 2) IDS=0.01 in., 3) IDS=0.025 in., and 4) IDS=0.05 in. Note that the 0.005 in. flaw size is the Joint Specs, Ref. [12] accepted damage tolerant flaw for a cold worked hole (from A3.12.1, “Small imperfections equivalent to an .005 inch radius corner flaw resulting from these operations are assumed to exist in each hole of each element in the structure and provide the basis for the requirements in paragraphs d, e, and f, below...”) 0.01 in. flaw size is a traditional durability flaw; and 0.05 in. is a traditional damage tolerant flaw (the remaining flaw, 0.025 in., has no special significance, other than it is between the traditional durability and damage tolerant flaws). The span of lives at a given maximum stress is small in Figure 20, relative to spans seen in Figure 21. For instance, in Figure 20, at 25 ksi, the span of lives from the 10% to the 90% IDS is 0.15 orders of magnitude (23,901 to 33,774 cycles), while in Figure 20, at 25, the span of lives is about 0.75 orders of magnitude (5,959 to 33,774 cycles). Because of the relative magnitudes of the initial flaws (0.00067 in. to 0.05 in.), this is to be expected.

4.1.4.2 Remaining Life Predictions

The remaining life from an initial flaw size was computed and is shown in Figure 22. The “remaining life” is defined as the number of cycles from a particular crack size subtracted from the number of cycles at coupon failure. The maximum stress has been varied from 10 to 30 ksi. One way to interpret these curves is to select a particular maximum stress, for example, 25 ksi, then interpolate the curves for various initial crack sizes, shown in Table 9 below. Table 9 then can be used to estimate for a given detectable crack size (say a damage tolerance flaw of 0.05 inches) what is the remaining life (in this instance, 5,685 cycles). This may be due to a smaller range of IDS or ‘failure flaws’ that lead to coupon failure: for this 2024-T351; at 20 ksi for instance, there is only a 40% difference between the lowest life (49,712 cycles) and the highest

life (70,636 cycles). Note that it is hard to make a direct comparison between the results here and with MIL-HDBK-5 data, since there is no $K_{t(\text{net})} = 2.8$ in MIL-HDBK-5, while all experimental data here is for coupons with $K_{t(\text{net})} = 2.8$.

Table 9. Remaining Life at Maximum Stress of 25 ksi

Initial Crack, in.	Remaining Life, cycles
0.00067	33,774
0.00096	28,523
0.00140	23,842
0.00500	12,367
0.01000	9,701
0.02500	7,337
0.05000	5,685

The last figure, Figure 23, charts the evolution of the crack aspect ratio from the initial flaw's aspect ratio (1.0) to the aspect ratio when the crack transitions from part-through to through (transition is defined as the bore flaw size growing to 90% of the coupon's thickness).

4.1.4.3 Conclusions and Recommendations

The fatigue lives of the centered hole (non Cold Work) specimens tested in Cold Work Plus-Up Program were predicted. Basic material data such as initial discontinuity states and material crack growth rates were obtained in a previous APES program and used in these analyses. Life predictions over a range of applied stresses were made. The next fatigue life prediction will examine the fatigue lives of cold worked coupons.

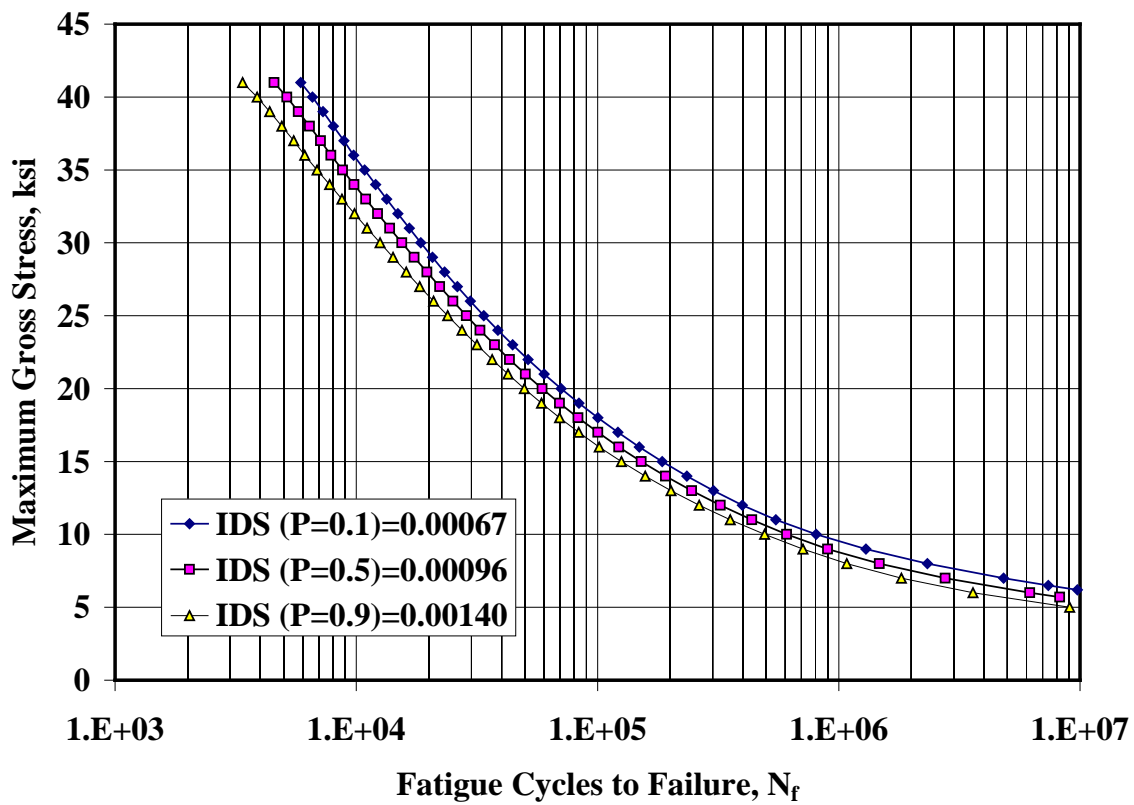


Figure 20. Fatigue Life Predictions. Open Hole. AA2024-T351

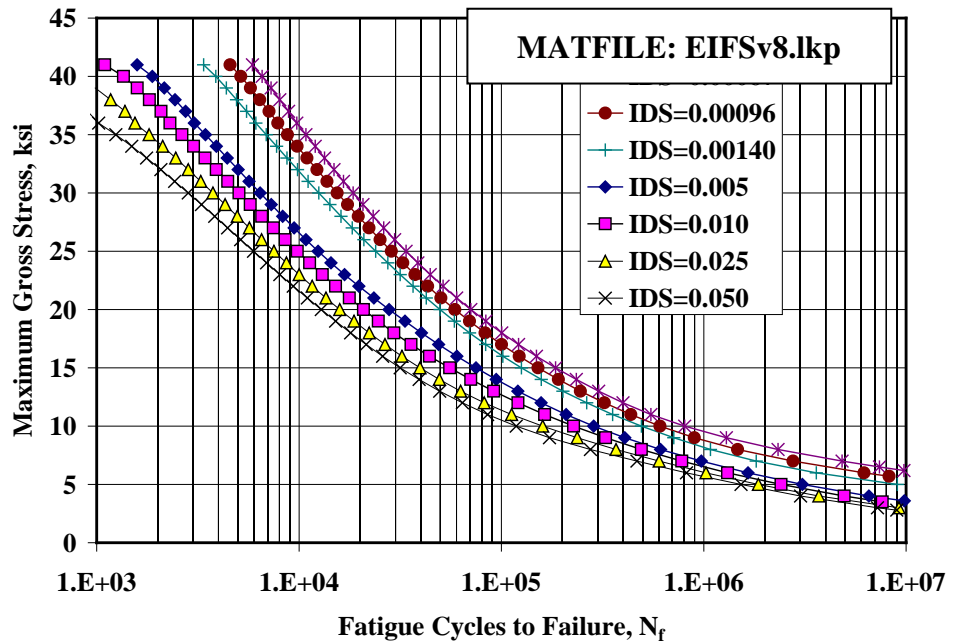


Figure 21. Fatigue Life Predictions. Open Hole. AA2024-T351

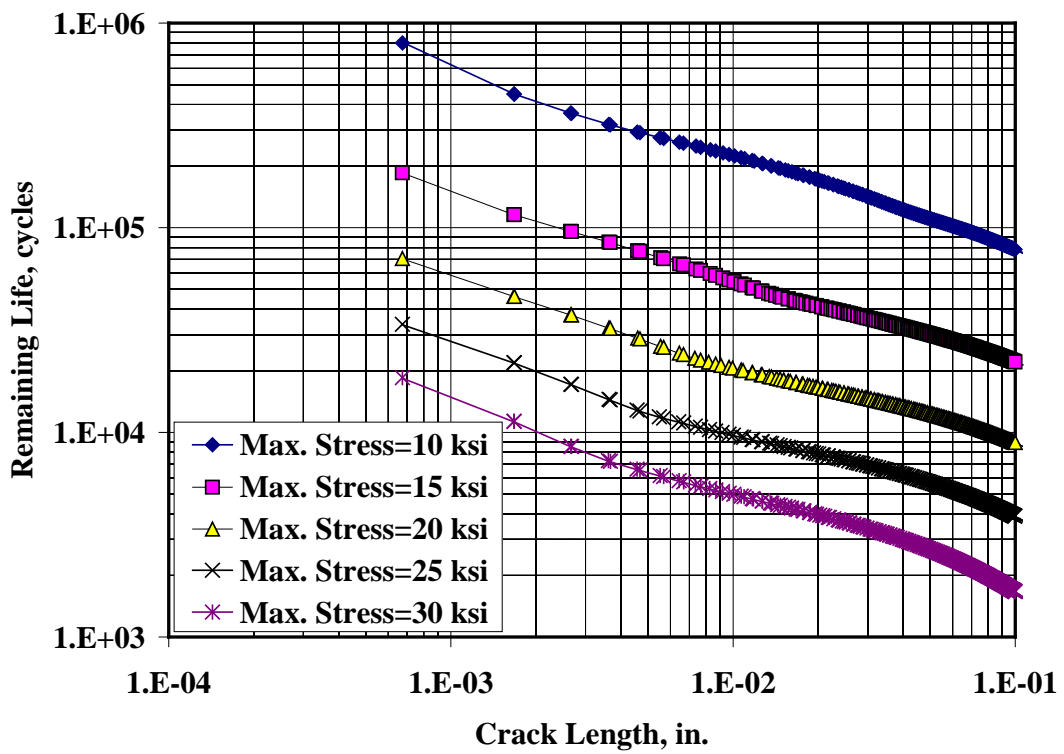


Figure 22. Remaining Life. Open Hole. AA2024-T351

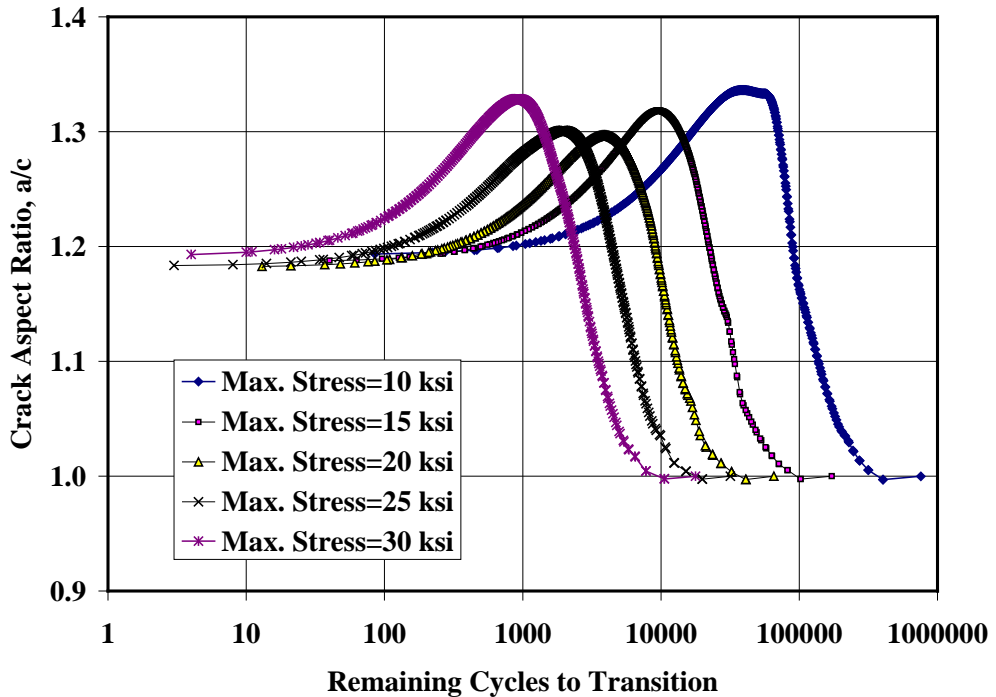


Figure 23. Crack Aspect Ratio to Through Crack Transition as a Function of Maximum Applied Stress. Open Hole. AA2024-T351

4.1.5 Digital Image Correlation, Open Hole Coupons

The AP/ES Digital Image Correlation (DIC) system was used to measure strains on the surfaces of a dog bone coupon with a centered, open hole. Strains were measured at tension load of 0 ksi, (to establish a ‘noise floor’), 12. ksi, and 15.0 ksi. In addition, the coupon geometry and load was simulated with the finite element method. Encouraging agreement between the DIC and FEM was found, with variations well within the measured repeatability as determined by the noise floor measurements. Further development of the DIC experimental techniques is warranted to improve the present “noise floor”.

4.1.5.1 Model

A single dog bone coupon, 2H11, was speckled painted and mounted in the MTS fatigue test frame. The coupon has a 0.25 in. diameter hole centered in the 2 in. wide gage section of the coupon, Figure 24. One face of the gage section was painted with a speckle pattern, to allow the DIC measurements.

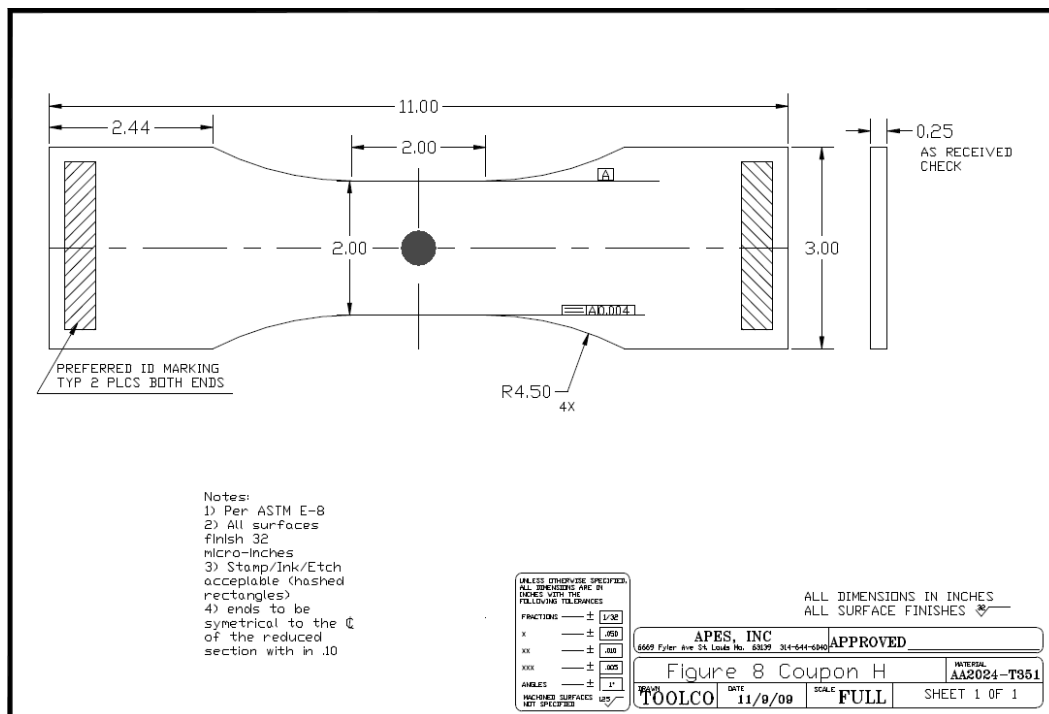


Figure 24. Dogbone Coupon Design

The dogbone coupon of Figure 24 was also analyzed with finite element software StressCheck; this report compares those FE results with the DIC measurements.

4.1.6 Results and Discussion

4.1.6.1 Noise Floor

The “noise floor” is the measurement of typical noise in the DIC strain measurements. The noise is then the expected variation in the strain measurements; any variation smaller than the noise cannot be counted as real. DIC images were taken with zero load applied, and strains computed

along several (in this case, 9) line profiles in the DIC image; these results are shown in Figure 25 below. It appears the noise level is about +/-0.0005 in/in, or about 500 microstrain. With Young's modulus of about 10,000 ksi, the stress uncertainty is on the order of 5 ksi.

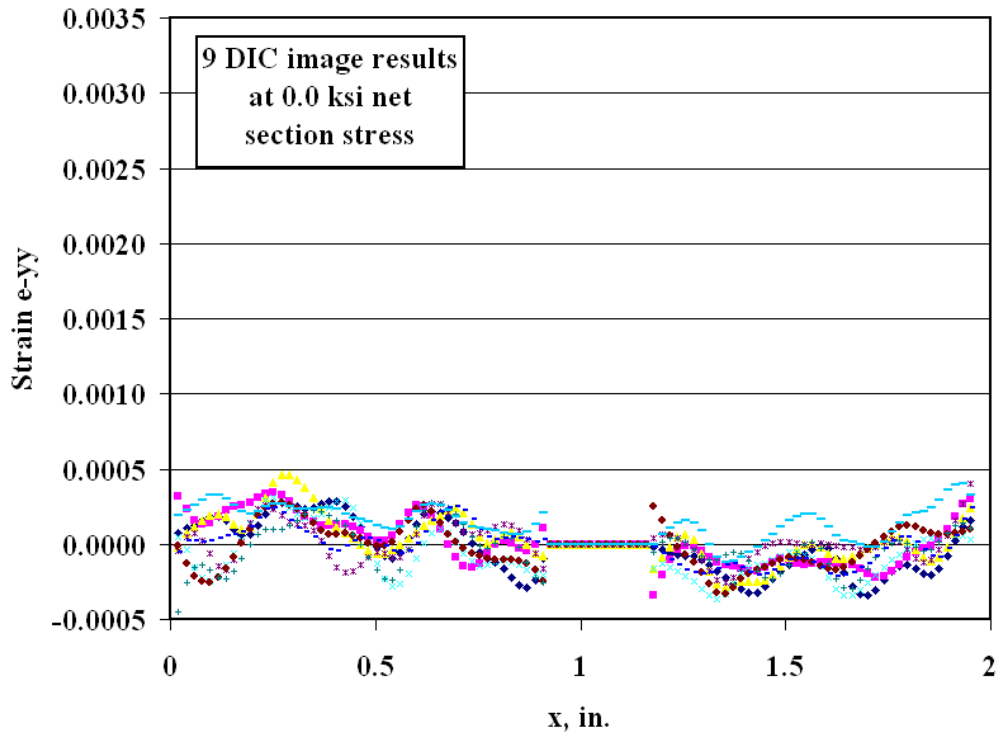


Figure 25. Measurement of DIC Noise Floor for a Non-Cx Hole

There are several sources of uncertainty in these DIC measurements: 1) out of plane displacements—if the surface being imaged moves more than 0.0001 in. relative to the undeformed surface, the image processing software can have problems interpreting the images 2) the DIC camera is visually aligned with the surface with the speckle pattern; the image processing software can have problems if the camera lens isn't perpendicular to the surface, and 3) the image processing software has to compute spatial derivatives of the displacement field; smoothing can help reduce the effect naturally occurring measurement noise has on the computation of the spatial derivative—if the displacement field is not smooth, noise in the displacements can cause spurious (in other words, not real) strains when the spatial derivatives are computed.

4.1.6.2 Strains at 12.5 ksi Load

Strains were computed with the DIC and with the FEA when the applied stress was 12.5 ksi gage (in front of the hole, not at the hole cross section). Because of challenges in the image interpretation method, often the AOI (area of interest) does not line up perfectly symmetric, nor are edges like hole rims well defined. The result can be a shifting of the hole and other features to off center of the image. It is apparent in Figure 25, for instance, that the center of the hole (the strains are zero in the hole region of the image) is not 'centered' at x=1.0 in.; therefore, the FEA results at this load are shifted to the right so that the center of the FEA hole is the same as the center of the hole in the DIC images. The correlation between the DIC measured strains and the

FEA computed strains is excellent, Figure 26. There are many oscillations in the DIC data, but these are on the order of the Noise Floor measurements noted previously.

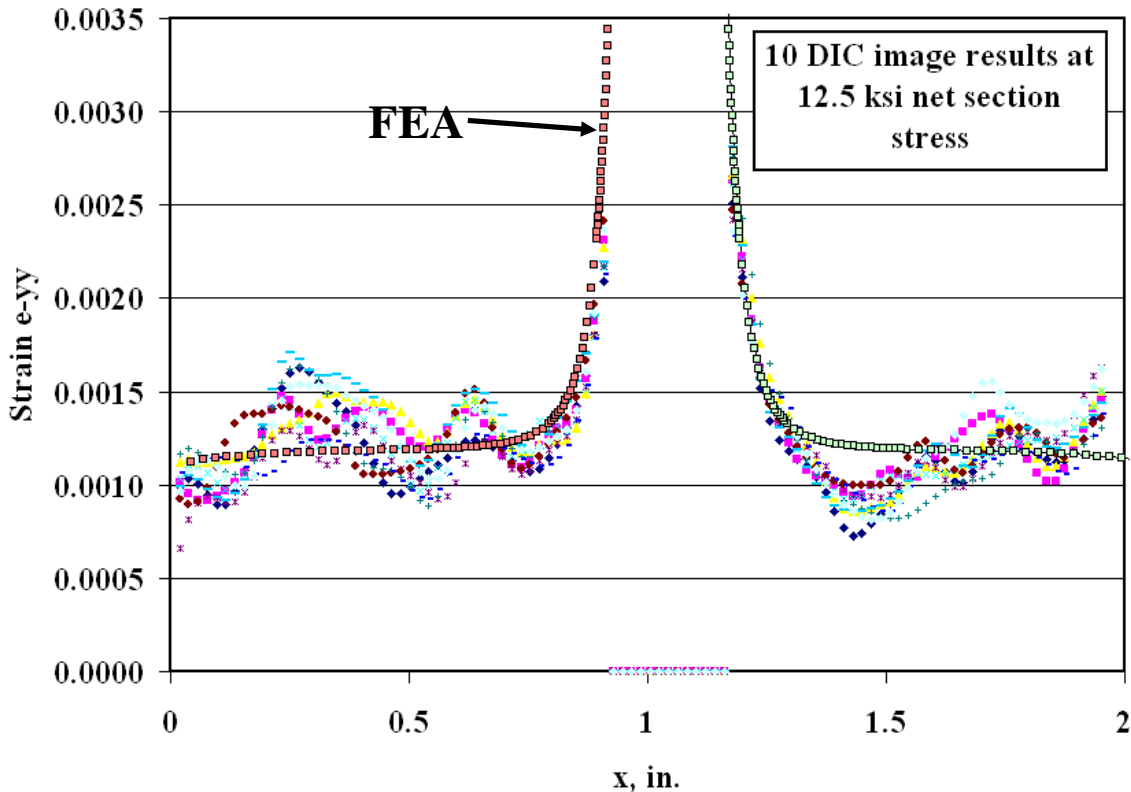


Figure 26. Comparison of FEA Computed Strains to DIC Measured Strains at 12.5 ksi

4.1.6.3 Strains at 15.0 ksi Load

Strains were computed with the DIC and with the FEA when the applied stress was 15.0 ksi gage (in front of the hole, not at the hole cross section). Again because of challenges with the image interpretation methods, the FEA results are shifted so the DIC and FEA hole centers line up. The correlation between the DIC measured strains and the FEA computed strains is again excellent, Figure 27. There are many oscillations in the DIC data, but these are on the order of the Noise Floor measurements noted in a previous section of this report.

4.1.6.4 Challenges Making Strain Measurements near Edges

There are significant challenges to measuring strains near edges; though there appears to be excellent agreement (within noise tolerances) between the DIC strain measurements and the FEA for most of the AOI, the DIC strain measurements do not peak as highly as the FEA predicts they should; for instance, at 12.5 ksi, the DIC strains peak at 0.002809 in/in, while the FEA predicts a peak at 0.0035 in/in at the hole edge. Similarly, at 15.0 ksi, the DIC strains peak at 0.00313155 in/in, and the FEA strains peak at 0.0042 in/in. Strains at an open hole have a very high gradient right at the hole edge, so that the strain concentration factor K_{te} is 3.04 right at the hole edge, but drops to 2.3 only 0.015 inches away from the hole edge; therefore if you cannot measure the

strains with the DIC right up the edge, the measured DIC strains will miss the strain concentration at the hole.

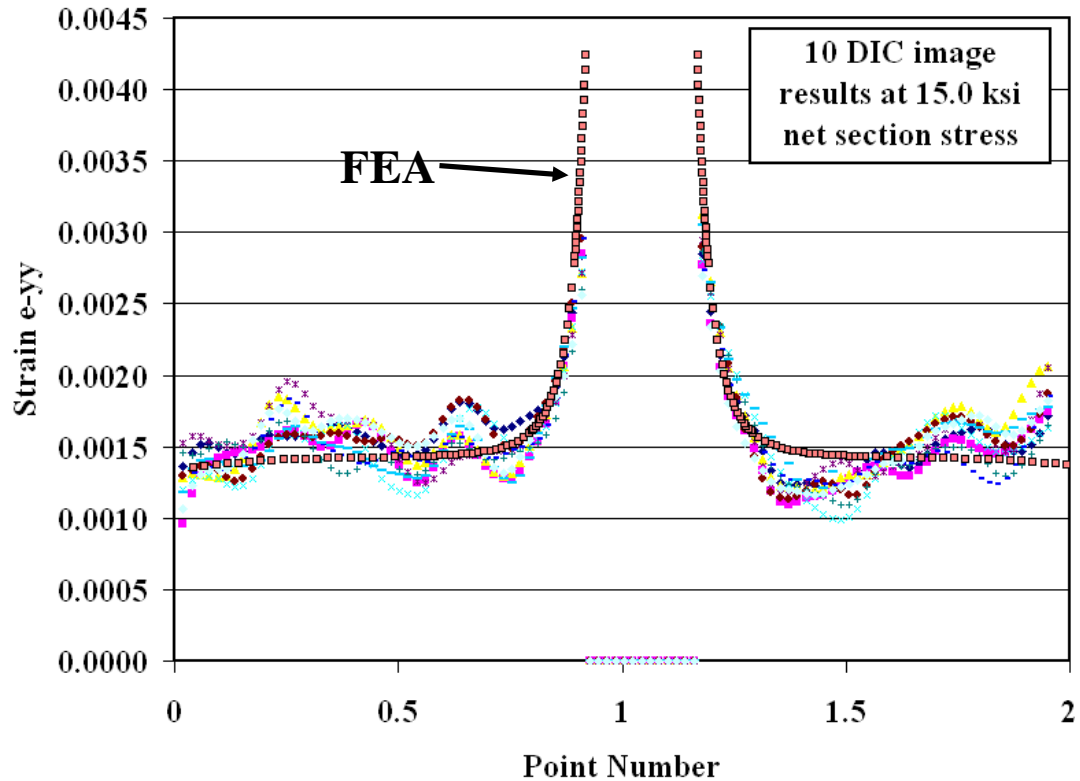


Figure 27. Comparison of FEA Computed Strains to DIC Measured Strains at 15.0 ksi

The correlation between the FEA and DIC methods indicates further refinement in methods are needed, but the results are encouraging. The relative displacement distribution shapes approaching the hole show good correlation with the FEA overlay, but suitable results were not available near the edge of the hole, nor are the results stable simulating the far field. It is likely that the DIC will not be able to produce readings all the way to the hole edge, as the dot patterns are disrupted by the cold working process. The variations far from the hole are perceived to be a function of experimental techniques and thus further refinement is needed.

4.1.6.5 Importance of Speckle Pattern and Reflectivity

Speckle patterns are of vital importance when attempting to achieve good image correlation between digital images. Eight different speckle patterns were examined in order to see how much “noise” they caused. We defined “noise” in the measurements as the difference in results between theoretically identical images. For each speckle pattern, a reference image was acquired along with nine other images, all acquired with no load on the specimen, and taken approximately one second apart. Figure 28 shows the eight speckle patterns and the areas-of-interest considered for each (highlighted in red). Statistics for the y-direction strain ε_{yy} (which is theoretically zero for all images taken) were obtained for each area-of-interest, as compared to the first reference image. These statistics included the minimum, maximum, mean, median, and

standard deviation of ε_{yy} of a dataset using every ε_{yy} correlation point in the area-of-interest. All images used a subset size of 21 and a step size of 5, meaning that every 5th pixel was used for correlation. Optimized 8-tap spline interpolations were used for all correlations, and the low-pass filter was not used, in order to maintain good spatial resolution. All speckle patterns are on specimen sections approximately 2" wide.

Figure 29, Figure 30 and Figure 31 present these results of the speckle pattern study; Figure 29 shows the basic speckle patterns, while Figure 30 and Figure 31 summarize the error measurements in histogram form. Three measures of noise were used; (1) the typical sigma error value for the nine correlations, also known as ‘confidence’ in the VIC-2D reports--lower values indicate better confidence in the correlations and smaller error, (2) the standard deviation in ε_{yy} , averaged over the nine images, and (3) the absolute maximum range in ε_{yy} , computed as the maximum ε_{yy} from all nine (9) images minus the minimum ε_{yy} from all nine (9) images.

The black speckle on bare aluminum pattern (F) shows the least noise and best correlation in all three comparisons. This is likely due to the fact that the aluminum background is highly reflective and saturates the pixels in the acquired image, providing extreme contrast between the saturated and black pixels. A potential drawback to this pattern is that the reflective patterns will likely shift as the specimen displaces. Lighting modifications (light diffusers, soft white incandescent light sources) might alleviate the problems. Patterns (D) and (E) show promise, as the black background seems to provide a more stable range of reference colors than does the white background. For reasons unknown, the white background seems to have a lot of fluctuation in greyscale measurements from image to image; it is anticipated that this is possibly affecting the spline fits and correlations.

Identical comparisons were also run using subset sizes of 31 and 41 pixels. The trends from these subset sizes are the same as for the 21-pixel subset size, though the error, standard deviation, and range are smaller across the board for the larger subset sizes. This reduced error and noise comes at the expense of spatial resolution, which will be important when measuring strain gradients. Optimizing both the speckle pattern and the subset size will provide the best results for future experiments using cold expanded holes.



Figure 28. Various Speckle Patterns Used for Noise Measurement

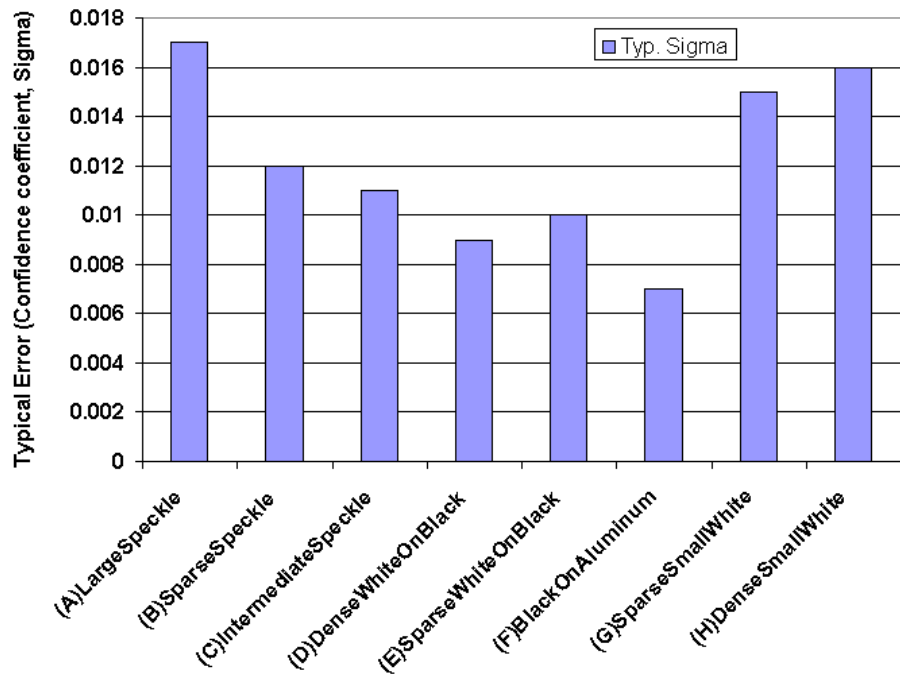


Figure 29. Typical Error (Sigma) Values for Eight Speckle Patterns

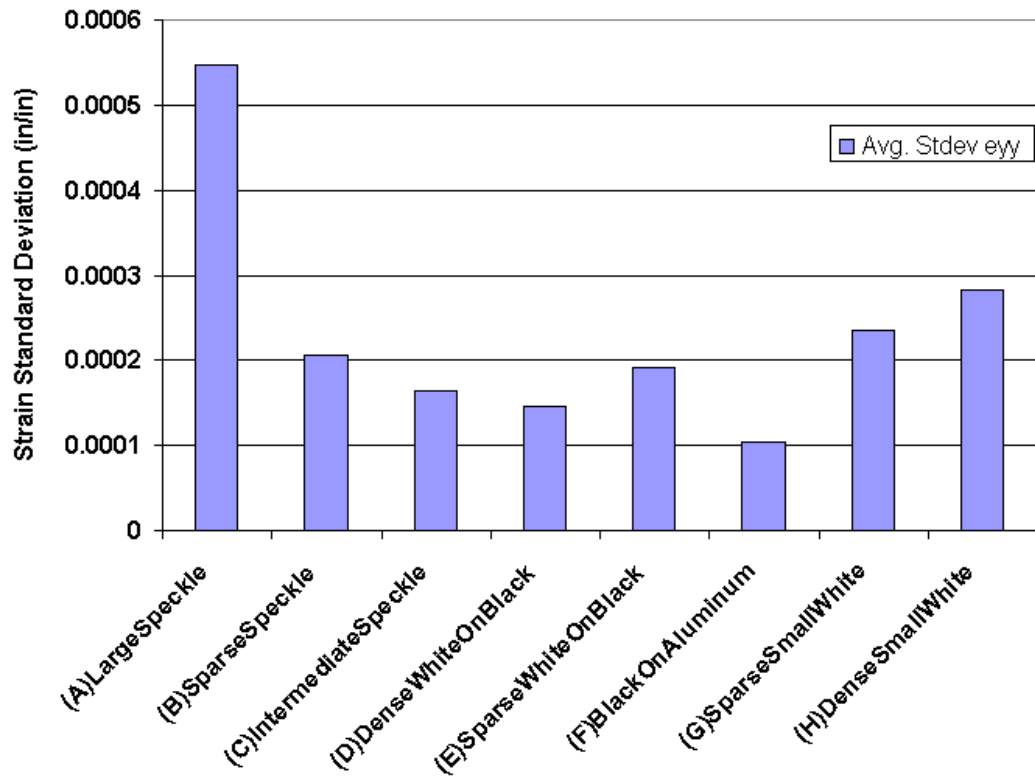


Figure 30. Average Standard Deviation in ϵ_{yy} for Eight Speckle Patterns

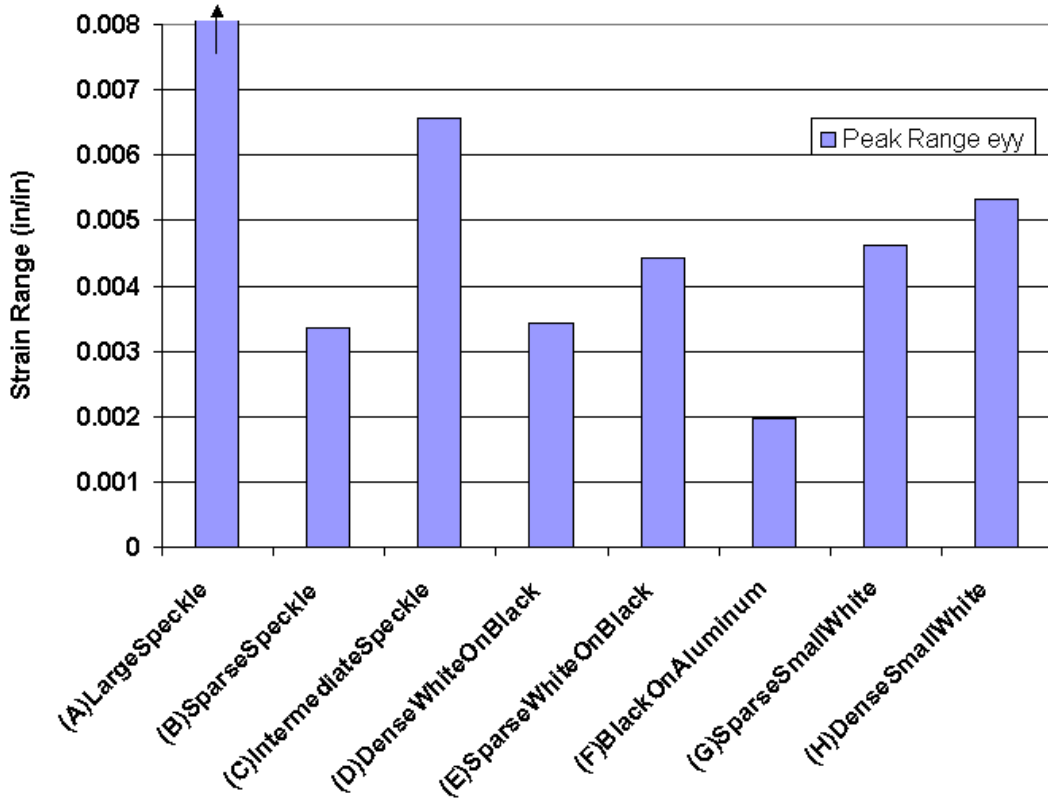


Figure 31. Peak Range of ϵ_{yy} Across All Images

4.2 Digital Image Correlation of Cold Worked Holes

DIC was used to measure the strains on the surface of a nominally 4% cold worked coupon being loaded with 27.5 ksi gage net section stress. The DIC measured strains were then compared to finite element simulations of the cold working process and subsequent applied tension of same magnitude as the test. Line profiles, one on each side (“left” and “right”) across the plane of the hole, were computed and plotted in Figure 32. The FE simulations of the cold working process alone (“Mandrel Removal”), and the cold working with applied tension, are compared in Figure 32 to the DIC measured strains. Certainly the DIC measured and FE computed strains are somewhat close to each other. Noticing the 3 DIC points near the $x=0$ origin that have strain values of 0 in./in., and that we have previously noted that the DIC image processing software has difficulty discerning precisely where the edges of the hole are. Perhaps, as Figure 33 attempts to show, the origin of the DIC measurements should be shifted to more closely line up the DIC and FE strains.

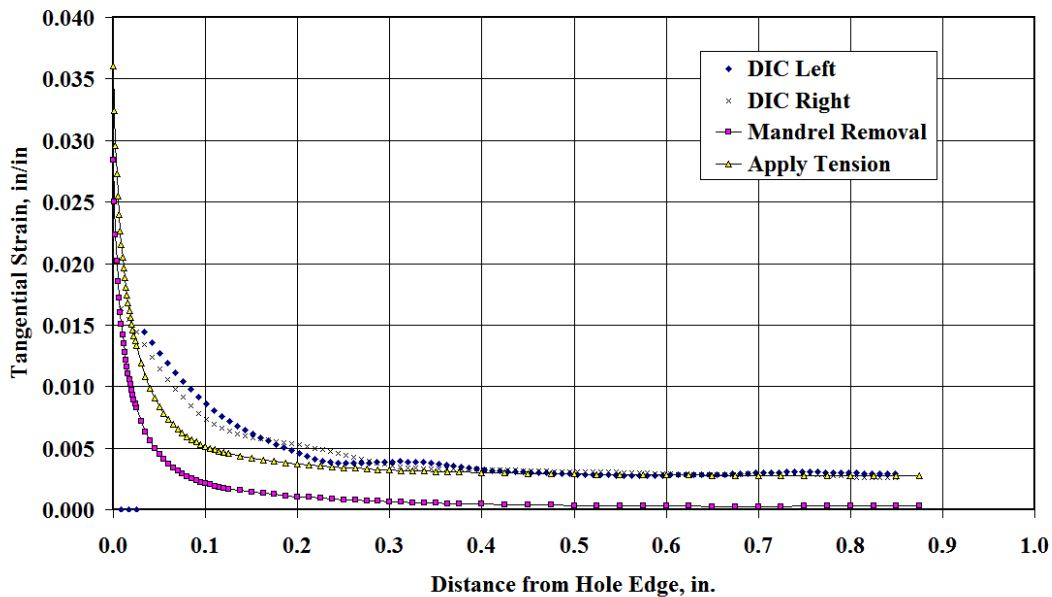


Figure 32. Correlation of DIC Measured Strain at 27.5 ksi Applied Load with FEA Simulations

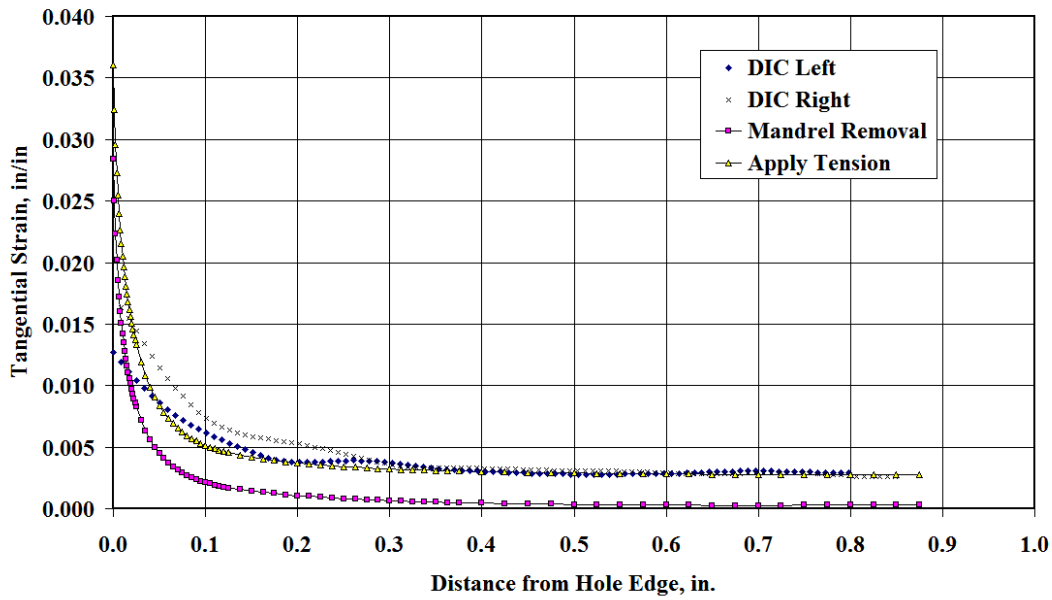


Figure 33. Correlation of Shifted DIC Measured Strain at 27.5 ksi Applied Load with FEA Simulations

Whether or not the DIC strains are shifted, the DIC strains appear ‘softer’ than the FEA strains, in that they do not exhibit as severe a peak strain and the overall strain gradient is softer than in the FEA simulations. This may indicate an inability of the FEA material stress-strain curve to represent the stress-strain behavior during cold working.

4.3 Fatigue Testing of Cold-worked Coupons (Task 2)

Each of the three (3) non cold worked coupons went through the following procedure:

- Hole drilled
- EDM notched
- pre-cracked
- final ream

Fatigue to failure; traveling microscope used to periodically monitor and record crack lengths

Each of the first 4 cold worked coupons (2H08, 2H09, 2H10 and 2H14) went through the following procedure (this is CX Process 1):

- Hole drilled
- Cold worked (nominal) 4%
- EDM notched
- pre-cracked
- final ream
- Fatigue to failure; traveling microscope used to periodically monitor and record crack lengths

Each of second 4 cold worked coupons (2H15, 2H16, 2H17, 2H18, and 2H19) went through the following procedure (this is CX Process 2):

- Hole drilled
- EDM notched
- pre-cracked
- Cold worked (nominal) 4%
- final ream
- Fatigue to failure; traveling microscope used to periodically monitor and record crack lengths

During each fatigue test, the fatigue cycling load was periodically stopped so that any cracks that appear on the hole bore or on any of the surfaces could be measured and recorded. Table 10 summarizes the pre-crack measurements and fatigue lives for the coupons tested.

Table 10. Summary of Fatigue Behaviors of AA2024 non CX (2H20/2H33/2H34) and CX Coupons (all others). Each coupon had EDM notch and pre-cracking procedure, though the EDM-pre-crack-CX sequences differed

Coupon	Surface EDM, in.	Bore EDM, in.	Surface Pre- crack, in.	Bore Pre- crack, in.	Total Fatigue Life, Cycles
2H20	0.01191	0.02052	0.02628	0.03418	22,847
2H33	0.01104	0.02054	0.02914	0.03640	20,597
2H34	0.01287	0.01994	0.02472	0.03482	18,616
2H08	0.01222	0.01954	0.02810	0.03486	121,312
2H09	0.01241	0.0217	0.02166	0.04136	65,890
2H10	0.01191	0.01874	0.02200	0.03204	126,587
2H14	0.01238	0.01844	0.02032	0.02936	180,066
2H15	0.01206	0.01644	0.01838	0.03556	176,893
2H16	0.01123	0.01904	0.02286	0.07736	137,640
2H17	0.01206	0.02098	0.04972	0.05872	110,553
2H18	0.01145	0.02112	0.04808	0.07680	131,931
2H19	0.01169	0.01953	0.05132	0.06248	138,257

The measured crack propagation of three (3) non CX coupons and nine (9) cold worked coupons is summarized in Figure 34 below. The total life of each individual coupon is used to normalize the intermediate number of cycles (to summarize, 2H20/33/34 are non CX, 2H08/09/10/14 are CX Process 1, and 2H15/16/17/18/19 are CX Process 2). The crack propagation behaviors in the Non CX Coupons (2H20/33/34) collapse well; while the crack propagation behaviors of the various CX Coupons have some qualitative variations. The crack propagation behaviors of Coupons 2H08, 2H10, and 2H14 are qualitatively close, each with three (3) distinct regions: rapid propagation, followed by much slower but still steady increase in crack lengths on the surface, and each measurements that look like the beginning of rapid propagation that is characteristic of fast fracture. It's possible that 2H09 has the same qualitative behavior, which would have been apparent if cracks would have been apparent prior to 45% of the total life of 2H09. An additional coupon, 2H07, was tested, but results aren't shown here because 2H07 had a badly placed EDM notch.

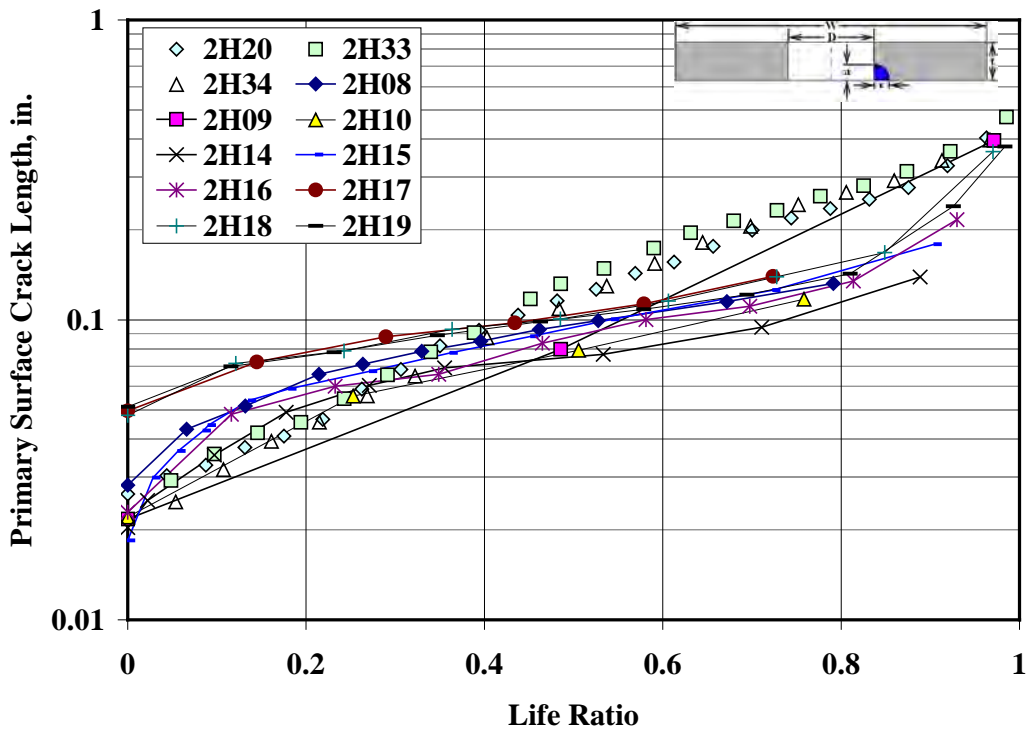


Figure 34. Comparison of Crack Propagation Normalized to Total Life. The Non CX Coupons (2H20/33/34) Collapse Well; the CX Coupons Have Some Qualitative Variations

Coupons 2H15, 2H16, 2H17, 2H18, and 2H19 were cold worked and tested to failure. These coupons reversed the order of the pre-cracking and cold working from the first batch. In this batch of 5, the EDM and pre-cracking occurred as the first two steps in the testing process, THEN the coupons were cold worked and reamed to final diameter (last month, the cold working occurred first, then the EDM and pre-cracking). The last 5 entries in Table 10 summarize the pre-crack measurements and fatigue lives for the coupons tested in the second batch.

Similar to the procedure used for coupons 2H08/09/10/14 in the first batch, during the fatigue tests of each of coupons 2H15/16/17/18/19, the fatigue cycling load was periodically stopped so that any cracks that appear on the hole bore or on any of the surfaces could be measured and recorded. The total life of each coupon (2H15/16/17/18/19) is used to normalize the intermediate number of cycles in Figure 34. The crack propagation behaviors in all but three of the CX Coupons collapse well; the exceptions seem to be coupons 2H17, 2H18, and 2H19, which do not appear to be outliers in any other measure: total life, EDM notch sizes, or pre-crack dimensions. Though 2H17/18/19 stand out as quantitatively different from the other 6 coupons, the crack propagation behaviors of all CX coupons are qualitatively close, each with three (3) distinct regions: rapid propagation, followed by much slower but still steady increase in crack lengths on the surface, and each measurements that look like the beginning of rapid propagation that is characteristic of fast fracture.

There was one trend we noticed that appeared to be counter-intuitive: it's obvious from a cursory examination of the fatigue lives in Table 10 that there appears to be little correlation between the fatigue lives and the initial crack lengths or initial crack area—normally one would expect that

the larger the initial crack dimensions (lengths or area), the shorter the life. This counter-intuitive trend must be due to the presence of residual stresses of cold working; 36 AFGROW simulations with no residual stress, in which initial crack dimensions were varied from 0.0002 in. to 0.01 inch and aspect ratios from 0.02 to 50 demonstrate a clear trend of increasing fatigue life with decreasing initial crack area, Figure 35 (diamonds). The measured fatigue lives (triangles in Figure 35) show no such trend.

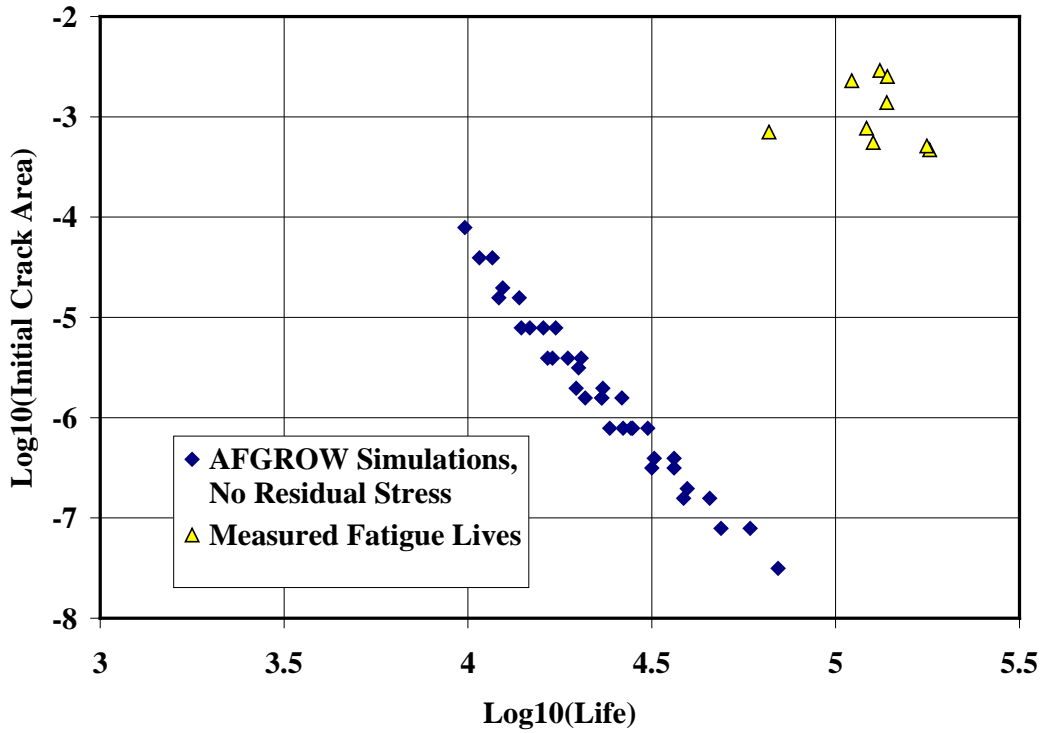


Figure 35. Simulated Fatigue Lives Increase with Decreasing Initial Crack Sizes (Area here); Measured Fatigue Lives Apparently Not Correlated with Initial Crack Sizes

It is well-known that there is variability in the cold working (CX) process itself; depending on the skill of the CX equipment operator, a nominally 4% CX hole might actually be cold worked from 3 to 5%. Such a wide variation in CX level has a dramatic effect on the variation of the residual stresses that are introduced into the hole area, and hence a dramatic effect on the measured fatigue lives. Metrology of the CX process is important if you want to quantify the variability of the CX level and the engineered residual stresses. The FTI cold working process and tooling, which includes the quality assurance measurement tools so that the operator knows the CX process was within FTI's specifications, was used for all CX processing. In addition to measurements made with those FTI Q/A tools, the physical dimensions of the holes, before and after the cold working mandrels were used to cold work the holes were measured with optical microscopy. The hole diameter of both the mandrel entrance and mandrel exit faces were measured with microscope, and the minimum specified mandrel diameter and minimum specified split sleeve thickness used to define a "Min. %CX"; a plot of the Min %CX as a function of Measured Fatigue Life is shown in Figure 36. Two interesting observations: 1) this plot reveals something that looks almost linear, that is, an increasing fatigue life with increasing

Min. %CX, which is expect (at least to a point)—the higher Min. %CX, the higher the residual stresses in the region, the higher the life and 2) there is a wide variation in Min. %CX for the same nominal CX level (4%)—from 2.26 to 3.05.

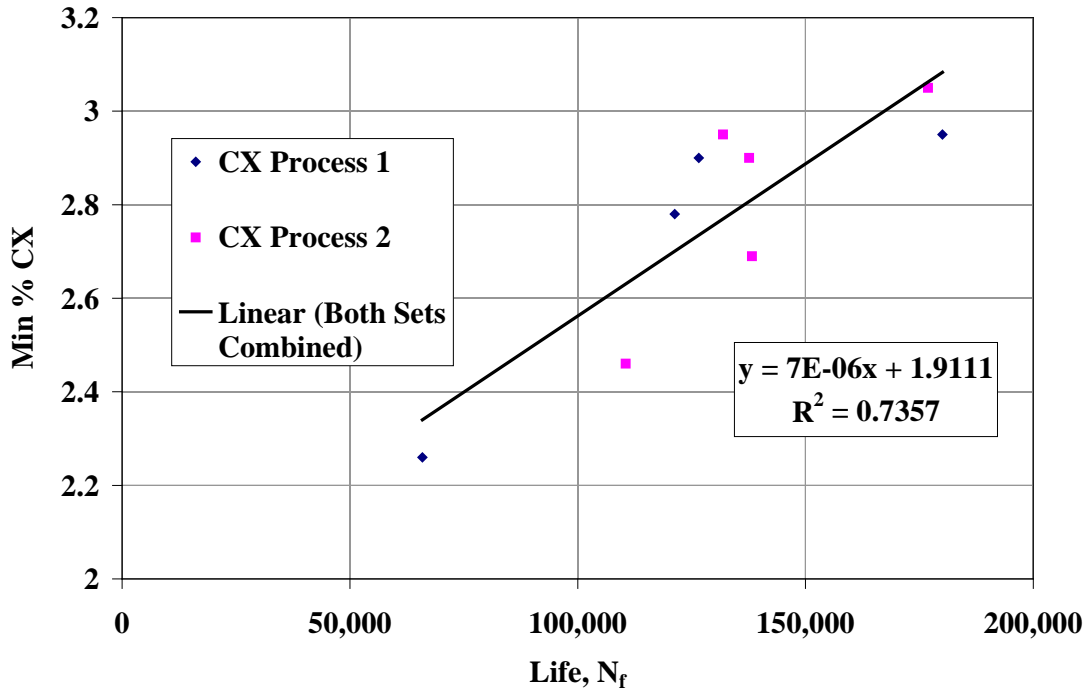


Figure 36. The Measured Fatigue Lives Increase with Increasing Cold Working Level. CX Process 1 and CX Process 2 refer to the order of cold working relative to EDM and pre-cracking process as discussed above

4.4 Modeling Fatigue in Cold-worked Coupons

Several analytical approaches are used to try to predict the effect of 4% Cold working on the fatigue lives of a dogbone coupon with a hole centered in the gage section. All results here are for a coupon with gage section 2 inches wide, 0.25 inches thick, with a 0.25 inch diameter hole, loaded by 25 ksi in the gross section of the gage section and bulk stress ratio $R = 0.1$.

4.4.1 Introduction

The results of several analytical approaches to modeling of crack growth life in cold worked holes are summarized here:

- AFGROW Residual Stress Modeling
- Weight Functions with Corner Crack Controlled by Independent Stresses
- Weight Functions with Corner Crack at Hole

In addition to the nine (9) coupons with EDM notches (crack starters) which results are shown in Table 10, eight (8) coupons were tested with naturally occurring cracking (no EDM notches, in other words). The fatigue test results of the naturally occurring cracks are shown in Table 11.

Table 11. Test Data for Coupons with Naturally Occurring Cracks

Coupon	CX	Stress, ksi	Stress Ratio	Life, cycles
2H01	Non CX	25	0.0	44,121
2H03	Non CX	25	0.0	37,915
2H04	Non CX	25	MB18	91,469
2H06	Non CX	25	0.0	39,020
2H05	CX 4%	25	0.0	195,695
2H54	CX 4%	28	0.1	160,039
2H35	CX 4%	22.5	MBDIC	181,845
2H36	CX 4%	28.75	MBDIC	765,380

These measured (AKA “Actual”) lives, in addition to the EDM notched coupons, will be used to compute the P/A (Predicted Lives/Actual Lives) in the analyses below. For all analyses discussed here, the applied far field stress and stress ratios are as shown in Table 10 and Table 11. and the crack scenario is single corner crack at a hole centered in a rectangular plate, with dimensions $W = 2.0 \text{ in.}$, $D = 0.25 \text{ in.}$, and $t = 0.25 \text{ in.}$. All materials are AA2024-T351, we use the AP/ES database 2024-T351 crack growth rates for all analyses (EISv8.lkp).

4.4.2 Modeling

4.4.2.1 Verification of Weight Function Approach

The Golden weight function method, Ref. [13], requires derivation of six weight function coefficients; therefore six equations are needed to derive those six coefficients. For this project, the weight functions were analytically derived for the case of a corner crack in a rectangular plate, and the case of a single corner crack at a hole centered in an infinite plate. The six equations are: 1) two each (for a total of four) for the corner crack in plate and corner crack at hole, for the Stress Intensity Factors for crack tips located on the surface and the hole bore surface, 2) the second derivative of the first weight function set to zero, and 3) the second weight function is set to zero. Note that for either constant (pure tension) or linearly varying stress (pure bending), this is a relatively quick derivation. However, for the case of a polynomial (such as stress at a hole, which is quadratic or higher in order), this can be a lengthy, complex derivation that must be done correctly to compute weight functions that yield SIFs close to the reference SIFs. Once the weight function coefficients are calculated, the Stress Intensity Factors for any input stress distribution can be calculated. If the weight function approach is consistent, it should return the AFGROW calculated Stress Intensity Factor solution for the corresponding stress distribution. For instance, the AFGROW solution should be returned for a corner crack located at a hole in an infinite plate, if the input is the stress distribution at the net section of a hole centered in an infinite plate (the so-called Timoshenko solution). Here, the weight function was verified by calculating the Stress Intensity Factors for a single corner crack located at a hole in a finite plate, by using the corresponding stress distribution for a hole centered in a finite plate. When the weight functions are computed, the output is the Geometry Factors for part-through and through cracks; these Geometry Factors are then used in a life prediction analysis. For an initial circular flaw of radius 0.0015 in., the key transition and final calculated parameters are found in Table 12.

Table 12. Verification of the Weight Function Method for Single Corner Crack at a Hole in an Infinite Plate

Calculated Parameter	Weight Function Prediction	AFGROW Prediction	$\Delta, \%$
Transition a	0.2451	0.2450	-0.029
Transition c	0.2064	0.2057	-0.336
Cycles to Transition	14,892	14,691	-1.368
Final a	0.2451	0.2450	-0.029
Final c	0.4587	0.4422	-3.731
Cycles to Failure	15,813	15,638	-1.119

Note that if the INFINITE plate stress solution was used to compute the Geometry Factors, the weight functions compute a life of 16,922 cycles, or 8% higher than AFGROW predicts.

4.4.2.2 AFGROW Modeling of Single Corner Crack at Hole

For a reference, the growth of a single corner crack from a non cold worked hole was simulated by AFGROW for constant amplitude and variable amplitude (marker band 18) tests, Table 13.

Table 13. AFGROW Reference Modeling, Non CX Coupons. MB18==Marker Band 18

Initial Flaw, in.	CDF	Stress, ksi	Stress Ratio	Life, cycles	P/A
0.000676	0.1	25	CA, R=0	33,692	0.8350
0.000959	0.5	25	CA, R=0	28,587	0.7084
0.001402	0.9	25	CA, R=0	23,898	0.5922
0.000676	0.1	25	MB18	54,251	0.5931
0.000959	0.5	25	MB18	45,570	0.4952
0.001402	0.9	25	MB18	38,340	0.4192

What initial flaw size would translate to a life of 40,352 cycles? A single (circular) corner crack of radius 0.00048 in. will yield a life of 40,402 cycles, within 0.5% of the average experimental life. For the same initial flaw size, but using MB18 marker band spectrum, AFGROW predicted the life to be 65,430 cycles, 28% smaller than the experimentally measured life.

4.4.2.3 Effect of Propagation Angle on AFGROW Life Predictions

The results of a bit of an exercise are discussed here, namely the effect of the angle on the crack front used to predict the coupon's life. AFGROW in the Single Corner Crack at a Hole model uses two SIFs to drive the elliptical corner crack. The Single Corner Crack at a Hole model is the Newman Raju solution described in Ref. [14]—this solution is a curve fit of a number of finite element simulations; the solution is function of several parameters: a/c , a/t , c/b , c/r , and ϕ . ϕ is the elliptic angle. AFGROW uses then the Newman Raju SIFs at two different ϕ ; by default, crack c is driven by the SIF for $\phi = 5$ deg. and crack a is driven by the SIF for $\phi = 80$ deg. The default angles can be changed for a particular AFGROW simulation—the effect

of changing the default ϕ is documented here. Simulations at default angle pairs 5/80 and 5/45 are performed; all applied stresses were 25 ksi, all stress ratios 0.0. Simulations are performed for various initial flaw sizes and without (Table 14) and without (Table 15) cold working residual stresses. The change in the angle for crack “a” from 80 degrees to 45 degrees causes the non cold worked coupon lives INCREASE, while causing the cold worked lives to DECREASE by changing the angle from 80 to 45. Note that the very same “residual SIF” is computed by AFGROW, independent of the angle used to compute the Newman Raju SIF.

Table 14. Effect of Default Angles on AFGROW Life Predictions, Non CX Coupons. Actual Life is 40,352 cycles

Initial Flaw, in.	CDF	Angle Crack c	Angle Crack a	Life, cycles	P/A
0.000676	0.1	5	80	33,692	0.8350
0.000959	0.5	5	80	28,587	0.7084
0.001402	0.9	5	80	23,898	0.5922
0.000676	0.1	5	45	44,396	1.1002
0.000959	0.5	5	45	37,733	0.9351
0.001402	0.9	5	45	32,103	0.7956

Table 15. Effect of Default Angles on AFGROW Life Predictions, CX Coupons. Actual Life is 195,695 cycles

Initial Flaw, in.	CDF	Angle Crack c	Angle Crack a	Life, cycles	P/A
0.000676	0.1	5	80	627,483	3.2064
0.000959	0.5	5	80	503,585	2.5733
0.001402	0.9	5	80	336,257	1.7183
0.000676	0.1	5	45	286,340	1.4632
0.000959	0.5	5	45	232,627	1.1887
0.001402	0.9	5	45	173,508	0.8866

This exercise is relevant to the testing in this program as the observed cracking on the fracture faces appears to be, in general, driven by the propagation of the crack along the surface and at 45 degree angle from the crack origin—in general, at these stress levels, the crack does not appear to propagate far up the hole bore, appearing to stop and ‘wait’ for the surface and internal crack fronts to grow large enough so that the primary crack merges with the secondary cracks that have stopped at the bore.

4.4.2.4 AFGROW Residual Stress Modeling

AFGROW has four (4) methods for adjusting the Stress Intensity Factors for stress states that are deviations from the stress states of the menu models: 1) Beta correction factor, 2) Stress correction factor, 3) Residual stress, and 4) Residual Stress Intensity Factor. We had measurements of the residual stress due to Cold Working from contour method measurements

made by Hill Engineering in July, 2010; therefore the first approach is to use the residual stress directly by reading into AFGROW's residual stress interface. The residual stress distribution (blue diamonds) used in all analyses is shown in Figure 37 below; note the residual stress is that measured on the mandrel Entry Plane.

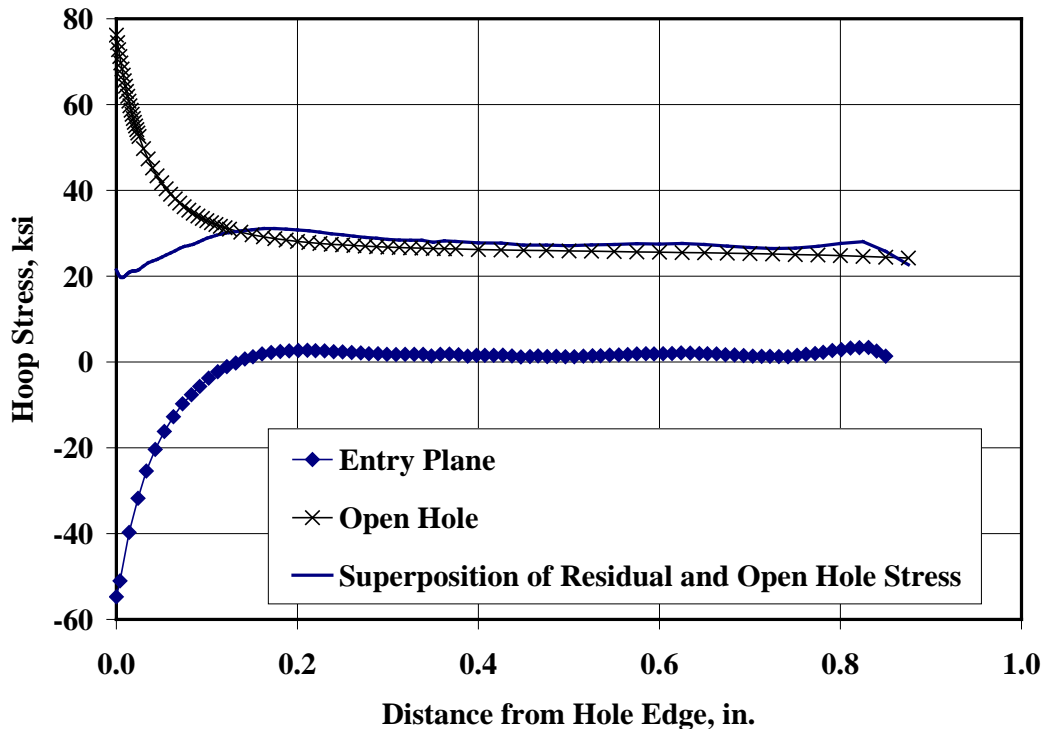


Figure 37. Residual Stress Distribution Measured by Hill Engineering with Contour Method

The results will be separated into two groups of coupons: the coupons with EDM notches shown in Table 10 and the coupons with naturally occurring cracks in Table 11. Since the EDM notches and subsequent pre-crack lengths were measured directly, the pre-crack lengths will be used as the initial crack lengths in the analyses in the Table 10 data; as the initial crack lengths were not known in the coupons with naturally occurring crack, the predicted lives were computed for a range of crack lengths, $IDS(P=0.1)=0.000676$ in., $IDS(P=0.5)=0.000959$ in., and $IDS(P=0.9)=0.001402$ in.

The predictions for the EDM notch coupons are found in Table 16.

Table 16. Predictions of EDM Notch Coupon Lives

Coupon	Initial Surface Crack, in.	Bore Surface Crack, in.	Actual Life, Cycles	Predicted Life, Cycles	P/A
2H20	0.02628	0.03418	22,847	23,972	1.0492
2H33	0.02914	0.03640	20,597	23,431	1.1376
2H34	0.02472	0.03482	18,616	23,919	1.2849
2H08	0.02810	0.03486	121,312	290,626	2.3957
2H09	0.02166	0.04136	65,890	269,639	4.0923
2H10	0.02200	0.03204	126,587	303,198	2.3952
2H14	0.02032	0.02936	180,066	313,843	1.7429
2H15	0.01838	0.03556	176,893	292,383	1.6529
2H16	0.02286	0.07736	137,640	156,912	1.1400
2H17	0.04972	0.05872	110,553	204,135	1.8465
2H18	0.04808	0.07680	131,931	155,059	1.1753
2H19	0.05132	0.06248	138,257	193,074	1.3965

The P/A results from cold working coupons in this table (the bottom 9) are plotted in Figure 38 below as a function of the Cumulative Distribution Function, CDF. The mean P/A is about 1.74, with a range from 1.14 to 4.09.

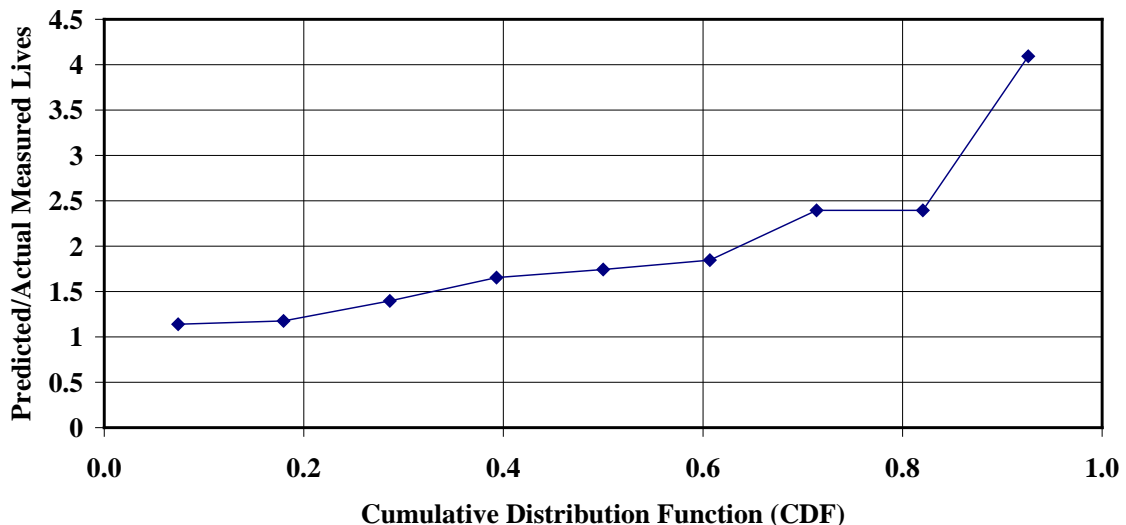


Figure 38. Ratio of Predicted/Actual Lives for Coupons with EDM Notches

A range of initial crack lengths were used to predict the lives of the coupons with naturally occurring cracks, as the initial crack lengths were unknown. The AFGROW results are summarized in

Table 17 below for three (3) initial flaw sizes for each coupon.

Table 17. Predictions of Coupons with Naturally Occurring Cracks

Coupon	Bore		Actual Life, Cycles	Predicted Life, Cycles	P/A
	Initial Surface Crack, in.	Surface Crack, in.			
2H01	0.000676	0.000676	44,121	147,197	3.3362
2H03	0.000676	0.000676	37,915	147,197	3.8823
2H04	0.000676	0.000676	91,469	226,423	2.4754
2H05	0.000676	0.000676	195,695	1,433,018	7.3227
2H06	0.000676	0.000676	39,020	147,197	3.7723
2H35	0.000676	0.000676	181,845	2,862,800	15.7431
2H36	0.000676	0.000676	765,380	>5000000	>6
2H54	0.000676	0.000676	160,039	370,519	2.3152
2H01	0.000959	0.000959	44,121	121,185	2.7467
2H03	0.000959	0.000959	37,915	121,185	3.1962
2H04	0.000959	0.000959	91,469	186,016	2.0337
2H05	0.000959	0.000959	195,695	1,186,758	6.0643
2H06	0.000959	0.000959	39,020	121,185	3.1057
2H35	0.000959	0.000959	181,845	2,034,897	11.1903
2H36	0.000959	0.000959	765,380	>5000000	>6
2H54	0.000959	0.000959	160,039	317,968	1.9868
2H01	0.001402	0.001402	44,121	97,153	2.2020
2H03	0.001402	0.001402	37,915	97,153	2.5624
2H04	0.001402	0.001402	91,469	147,849	1.6164
2H05	0.001402	0.001402	195,695	876,611	4.4795
2H06	0.001402	0.001402	39,020	97,153	2.4898
2H35	0.001402	0.001402	181,845	1,199,335	6.5954
2H36	0.001402	0.001402	765,380	3,348,364	4.3748
2H54	0.001402	0.001402	160,039	257,337	1.6080

The results from this table are plotted in Figure 39 below as a function of the Cumulative Distribution Function, CDF. The mean P/A is about 3, with a range from 1.6 to 15.7.

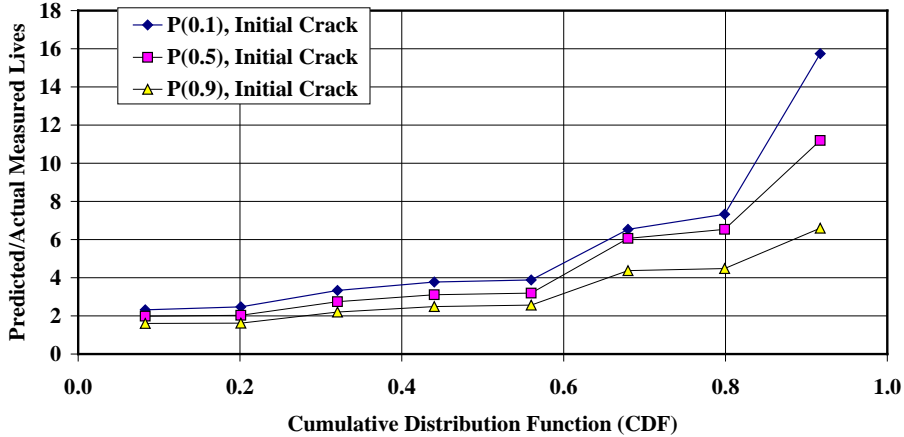


Figure 39. Ratio of Predicted/Actual Lives for Coupons with Naturally Occurring Cracks
The computed lives are larger than the experimentally measured life of all the coupons we tested.

4.4.2.5 Effect of Propagation on AFGROW Life Predictions

AFGROW in the Single Corner Crack at a Hole model uses two SIFs to drive the elliptical corner crack. The Single Corner Crack at a Hole model is the Newman Raju solution described in Ref. [14]—this solution is a curve fit of a number of finite element simulations; the solution is function of several parameters: a/c , a/t , c/b , c/r , and ϕ . ϕ is the elliptic angle. AFGROW uses then the Newman Raju SIFs at two different ϕ ; by default, crack c is driven by the SIF for $\phi = 5$ deg. and crack a is driven by the SIF for $\phi = 80$ deg. The default angles can be changed for a particular AFGROW simulation—the effect of changing the default ϕ is documented here. Simulations at default angle pairs 5/80 and 5/45 are performed; all applied stresses were 25 ksi, all stress ratios 0.0. Simulations are performed for various initial flaw sizes and without (Table 18) and without (Table 19) cold working residual stresses. The change in the angle for crack “ a ” from 80 degrees to 45 degrees causes the non cold worked coupon lives INCREASE, while causing the cold worked lives to DECREASE by changing the angle from 80 to 45. Note that the very same “residual SIF” is computed by AFGROW, independent of the angle used to compute the Newman Raju SIF.

4.4.2.6 Weight Function with Corner Crack Controlled by Independent Stresses

First, the geometric factors β were computed for a corner crack in a rectangular plate using the Golden Weight Function method, Ref. [13]. Next, the stress from the residual stress SUPERPOSED with the open hole stress was used to drive the two SIFs of the surface and depth cracks independently—the surface crack is driven by the superposed open hole and residual stress distributions (the solid line in Figure 37 above), while the depth crack is driven by the K_{σ} of the hole (the $x=0$ value of the superposed stress in Figure 37).

Table 20 contains the results of these simulations, which are only for the 4% cold worked coupons. Again, there are two groups of results: the EDM notched coupons, and the coupons with naturally occurring cracks—the initial crack lengths of the EDM notched coupons were as measured, and the initial crack lengths of the coupons with naturally occurring cracks for a range

of IDS, $\text{IDS}(P=0.1)=0.000676$ in., $\text{IDS}(P=0.5)=0.000959$ in., and $\text{IDS}(P=0.9)=0.001402$ in. Only the Constant Amplitude, $R=0$, tests were used in this Table.(of which we have one (1) coupon test finished) cycles.

Table 18. Corner Crack with Independent Stress Drivers

Coupon	Initial Surface Crack, in.	Bore Surface Crack, in.	Actual Life, Cycles	Predicted Life, Cycles	P/A
2H08	0.02810	0.03486	121,312	44,728	0.3687
2H09	0.02166	0.04136	65,890	47,147	0.7155
2H10	0.02200	0.03204	126,587	58,806	0.4646
2H14	0.02032	0.02936	180,066	66,804	0.3710
2H15	0.01838	0.03556	176,893	61,173	0.3458
2H16	0.02286	0.07736	137,640	25,703	0.1867
2H17	0.04972	0.05872	110,553	16,745	0.1515
2H18	0.04808	0.07680	131,931	13,046	0.0989
2H19	0.05132	0.06248	138,257	15,309	0.1107
2H05	0.000676	0.000676	195,695	2,455,328	12.5467
2H05	0.000959	0.000959	195,695	1,402,149	7.1650
2H05	0.001402	0.001402	195,695	890,127	4.5485

The EDM notch coupon lives are consistently under-predicted by the method, while substantially over-predicting the life of the one coupon with naturally occurring cracks.

4.4.2.7 Weight Function with Corner Crack at Hole with Shifted Stress

First, the geometric factors β were computed for a single corner crack at a hole centered in a rectangular plate using the Golden Weight Function method, Ref. [13]—the Golden weight functions require two independent crack models; the ones chosen are the corner crack in a rectangular plate and the single corner crack at a hole were chosen to derive the weight function coefficients. For these coefficients, the Geometry factors for the residual stress SUPERPOSED with the open hole stress were computed, and subsequently used in life predictions. The cracks on the failed coupons tended to nucleate some distance away from the corners—to reflect the stress distribution that the cracks would likely experience, the virtual origin of the hole bore is shifted away from the actual hole bore (0.1625 in. here), and the weight functions computed for the shifted stress distribution, which is plotted in Figure 40 below. Note that the shifted stress distribution starts near where the residual stress becomes (slightly) tensile, and is small in magnitude compared to the open hole stress.

The geometry factors for this shifted stress distribution are computed, the Stress Intensity Factors computed, and subsequently, these Stress Intensity Factors are used in life predictions for the three crack sizes, Table 21 below.

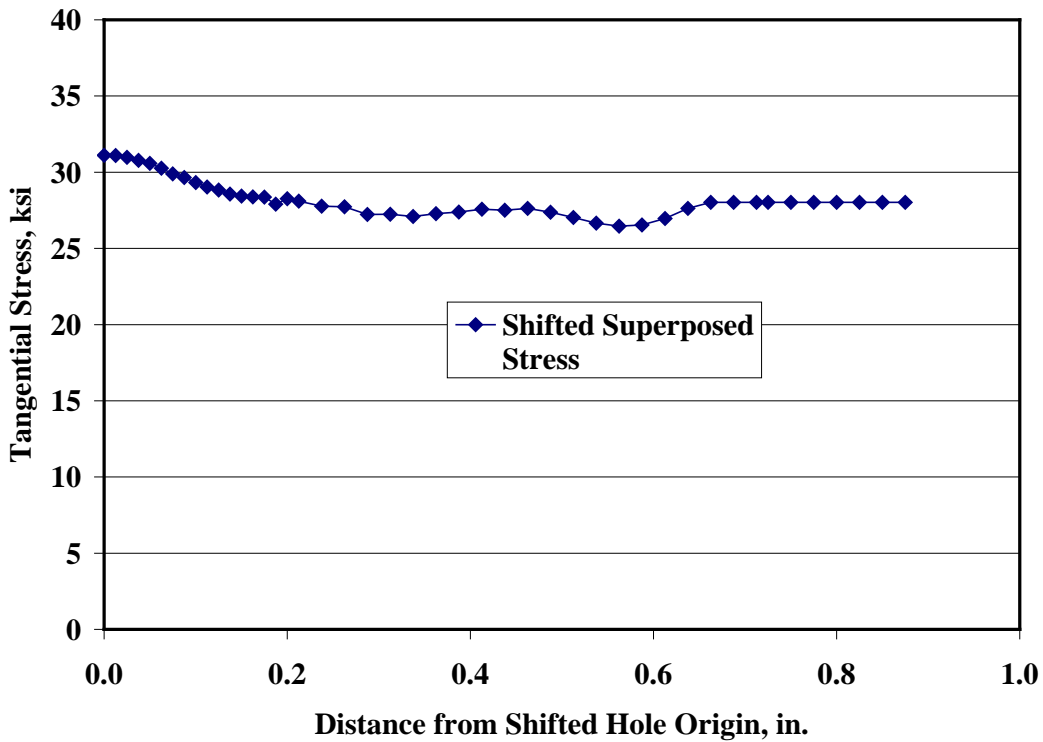


Figure 40. Shifted Stress Distribution

Table 19. Corner Crack at Hole with Superposed Residual and Open Hole Stress

Coupon	Initial Surface Crack, in.	Bore Surface Crack, in.	Actual Life, Cycles	Predicted Life, Cycles	P/A
2H08	0.02810	0.03486	121,312	16,016	0.1320
2H09	0.02166	0.04136	65,890	16,559	0.2513
2H10	0.02200	0.03204	126,587	19,132	0.1511
2H14	0.02032	0.02936	180,066	20,938	0.1163
2H15	0.01838	0.03556	176,893	19,648	0.1111
2H16	0.02286	0.07736	137,640	11,033	0.0802
2H17	0.04972	0.05872	110,553	8,300	0.0751
2H18	0.04808	0.07680	131,931	7,037	0.0533
2H19	0.05132	0.06248	138,257	7,788	0.0563
2H05	0.000676	0.000676	195,695	400,605	2.0471
2H05	0.000959	0.000959	195,695	303,861	1.5527
2H05	0.001402	0.001402	195,695	228,936	1.1699

The results are again a mixed bag; the EDM notch coupon lives are consistently unpredicted by the method, while over-predicting the life of the one coupon with naturally occurring cracks.

4.4.3 Conclusions

Three analytical approaches were tried to predict the effect of 4% cold working on the life of a dogbone coupon: 1) AFGROW Residual Stress Modeling, 2) Weight Functions with Corner Crack Controlled by Independent Stresses, and 3) Weight Functions with Corner Crack at Hole with Shifted Stress. The first method, AFGROW Stress Modeling worked reasonably well, while the other two methods Weight Functions with Independent Stresses and Weight Functions with Corner Crack at Hole with Shifted Stress, worked poorly. Note that the experimental data set used to correlate with these predictions is extremely limited, as only one test has been completed, with a life of 195, 695 cycles. We would normally expect a large scatter to be present in any experimental data set that is statistically relevant, and anticipate the 1st and 3rd methods would look even better against a larger experimental database, but the 2nd method still would be too conservative.

5 Application of Superposition to Verify the Need for Relaxation and Redistribution Effects (Task 5)

In order to demonstrate the relevance of stress redistribution, analyses demonstrating the use of superposition to evaluate crack growth through cold-worked holes were performed. Finite element analyses were performed to determine the Mode I Stress Intensity Factors, K_I , using the same initial flaw size, geometry, and loading conditions as tested in Task 2 on both a cold-worked and pristine specimens. This analysis included measurement and analysis of crack growth for crack lengths along the entire length of the specimen so that a K_{res} vs. crack length curve can be determined.

5.1 Literature Review

There is some evidence in the literature that the residual stresses caused by cold working can be “relaxed” by tension or compressive loads. For instance, Nadri et al Ref. [15] measured and computed the residual stresses of cold working after various compression loads were applied; the stresses were measured on the surfaces of the mandrel entrance and exit sides, using x-ray diffraction. The stresses were also computed with finite elements, for the same load conditions, using ABAQUS. An incomplete definition of the material constitutive relation was given by Nadri, therefore, only qualitative comparisons with Nadri et al results were possible.

For the StressCheck simulations, the 4% cold working of a hole was modeled in the dogbone specimen design from this Program. The gage section was 2 inches wide; the hole radius was 0.125 inches. The mesh for all simulations reported here, unless otherwise specified, is shown in Figure 41 below.

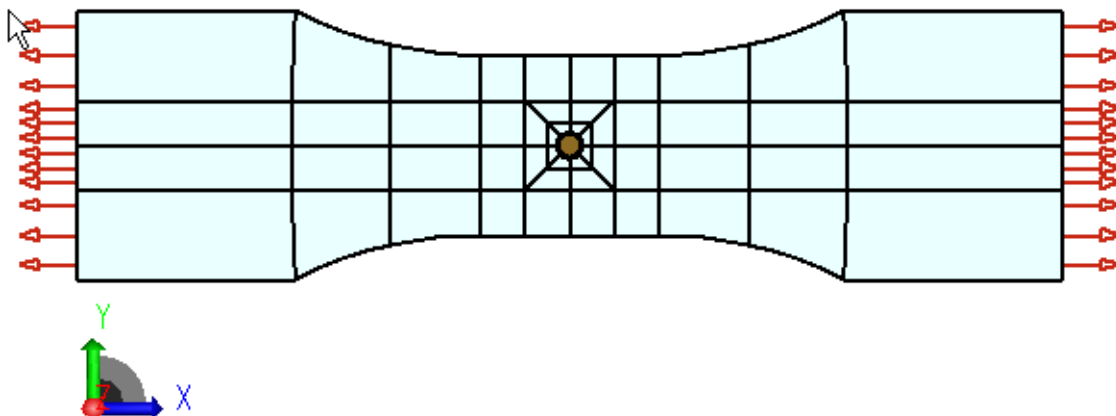


Figure 41. StressCheck Finite Element Mesh

The choice of plastic material constitutive relation can have anywhere from no influence to a substantial influence on the results. StressCheck’s suite of plasticity relations includes elastic-perfectly plastic, “Ramberg-Osgood” (so-called “power law”), and bilinear. In addition, the user can choose isotropic or kinematic hardening (or a mix of the two), but only with the bilinear plasticity relation. We used the bilinear relation, which allowed a full range of hardening from isotropic to kinematic to be simulated, Table 22. These parameter values were derived from the monotonic stress strain tests conducted during this Program.

Table 20. Bilinear Material Parameters

Parameter	Value
Young's Modulus	10,625 ksi
Tangent Modulus	35 ksi
Yield Stress	57.3 ksi
Hardening	Kinematic, $\beta=1$

For all load cases, the 4% cold working of the hole was simulated first. This simulation requires two steps: insertion of the mandrel, and removal of the mandrel. Subsequently, a single compressive (tension) load is applied, and then released. Stresses from the hole edge to the edge of the gage section are computed for the entire range of applied loads.

Nadri, et al both measured and computed residual stresses of not only the cold working process, but also the residual stresses as they were affected by compression overloads. X-ray diffraction (XRD) was used to measure the surface stresses on the inlet and outlet sides, though only the outlet side is discussed here. The finite element software ABAQUS was used to simulate the cold working process and compression overloads. Figure 42 is a comparison of the XRD and finite element results on the “outlet face” (AKA “exit face”) of the coupons, for the cold working process (marked “0 kN” in the legend) and for the compression overload (marked “-50kN” in the legend). Based on the Nadri geometry given in the cited reference, -50kN is equivalent to -28.55 ksi. There appears to be excellent agreement between the finite element and XRD results, after the initial cold working and the compression overload. For reference, Nadri et al measured stresses in AA024-T351 plate, Young's Modulus 10,428 ksi, yield stress 50 ksi. This compares to the material relations we used in the simulations here, 10,625 ksi and 57.3 ksi, respectively. The Nadri et al reference did not mention the type of plasticity model used, nor if the kinematic or isotropic hardening (or a mix) was simulated. The Nadri hole radius was approximately 0.172 in.

The Nadri XRD measurements show a “bottoming out” of the cold working residual stresses at about -47 ksi (-321 MPa), a little bit larger than the yield stress, at a distance of 0.040 in. (1 mm) from the hole edge. When a compressive overload is applied and released, the minimum stress shifts to -18 ksi (-123 MPa) at a distance of 0.167 in. (4.25 mm). The Nadri finite element simulations in Figure 42 demonstrated behavior, qualitatively and quantitatively similar to the XRD measurements.

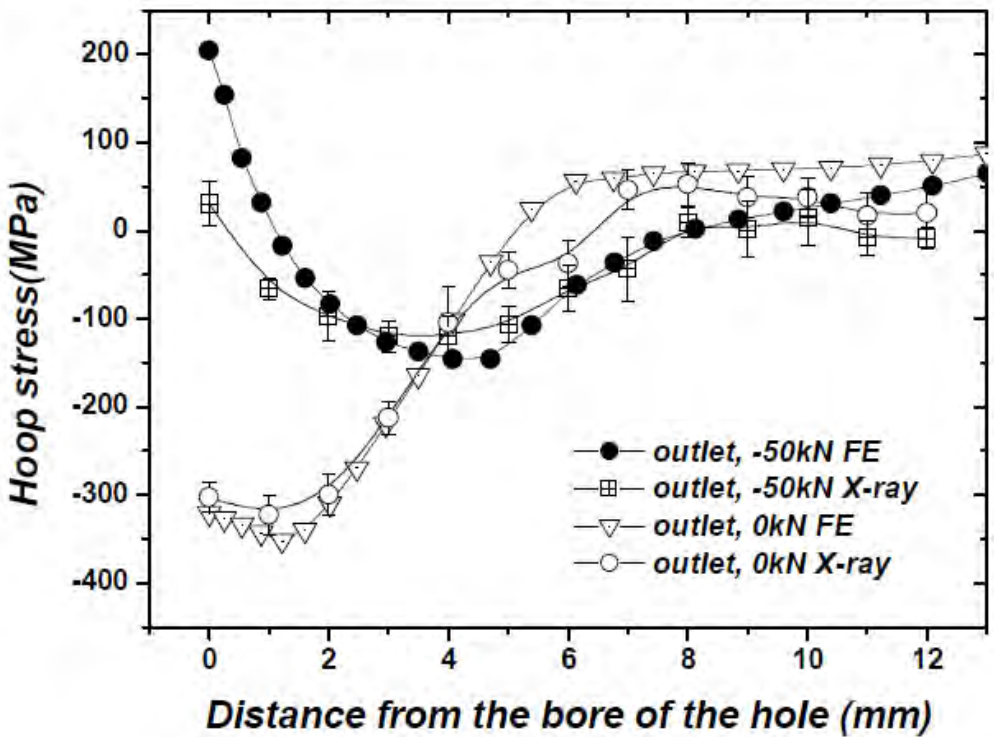


Figure 42. Relaxation of Residual Hoop Stresses by Compression Load as Measured by XRD and Computed by Finite Element Method. Outlet Face. 100 MPa=14.5 ksi

The p -version finite element software StressCheck was used to simulate cold working process and the compression overload. For comparison, a tension overload (instead of the compression overload) was also simulated. The magnitude of the compression and tension overloads was 27.5 ksi, less than 5% lower than the magnitude of the Nadri overload simulations. Figure 43 summarizes the hoop stress S_{tt} for the following loads: mandrel in, mandrel out (cold working process finished), compression applied and compression released. 4% cold working was simulated. After the mandrel is inserted the hoop stress behaves ‘almost’ as expected; if the stress had been entirely elastic, you would expect a large non-zero, positive hoop stress at the hole edge, but in this case, the material around the hole is deforming plastically, so that a negative hoop stress is predicted at the hole edge. This behavior is counterintuitive; however, if you consider that the von Mises failure theory is used in the plasticity simulations, then it is clear that if the radial stress (one of the principal stresses in the von Mises stress calculation) becomes large enough, say for a very large displacement of the hole in cold working, the hoop stress has to go into compression. This behavior is obvious in the 4% CX here.

After the mandrel is removed, a large zone of compression residual stress remains near the hole edge, eventually becoming positive (tension) approximately 1 radius from the hole edge. The maximum compressive stress for this particular material is -61 ksi, 7% higher magnitude than the tension yield stress. A 27.5 ksi compressive overload drives the hoop stress further down, extending the download sloping range of the hoop stress from 0.02 in. to 0.095 in. from the hole edge. The interesting behavior occurs when the compressive load is released; the hoop stress responds by increasing to 27.4 ksi at the hole edge, dropping down to -29 ksi as it bottoms out, then increases until it becomes again positive (tension) at a distance a little bit larger than the hole radius.

The hoop stress has a completely different behavior when the tension overload was applied and released, Figure 44. The 4% cold working was again simulated; hoop stresses are exactly the same as the compression overload results. After the tension overload is applied, the hoop stress goes up an amount exactly equal to the elastic hoop stress at an open hole centered in a plate. The hoop stress is high, but still less than 2/3rds of the yield stress for all points. After the tension is released, the hoop stress returns exactly to where it was before the tension overload was applied, that is, right after the cold working process ended.

According to the literature, the residual stresses caused by cold working can be relaxed by tension and compression loads. In this study, the residual stresses caused by 4% cold working are first computed with StressCheck; subsequently, the residual stresses are “relaxed” by simulation of a tension or compression overload. We found that the hoop stresses after cold working and after the compression overload were applied were qualitatively similar to the Nadri XRD measurements and FEA computations. We also found that residual stress could easily be relaxed with compressive overloads in StressCheck, but could not be relaxed for large tension loads.

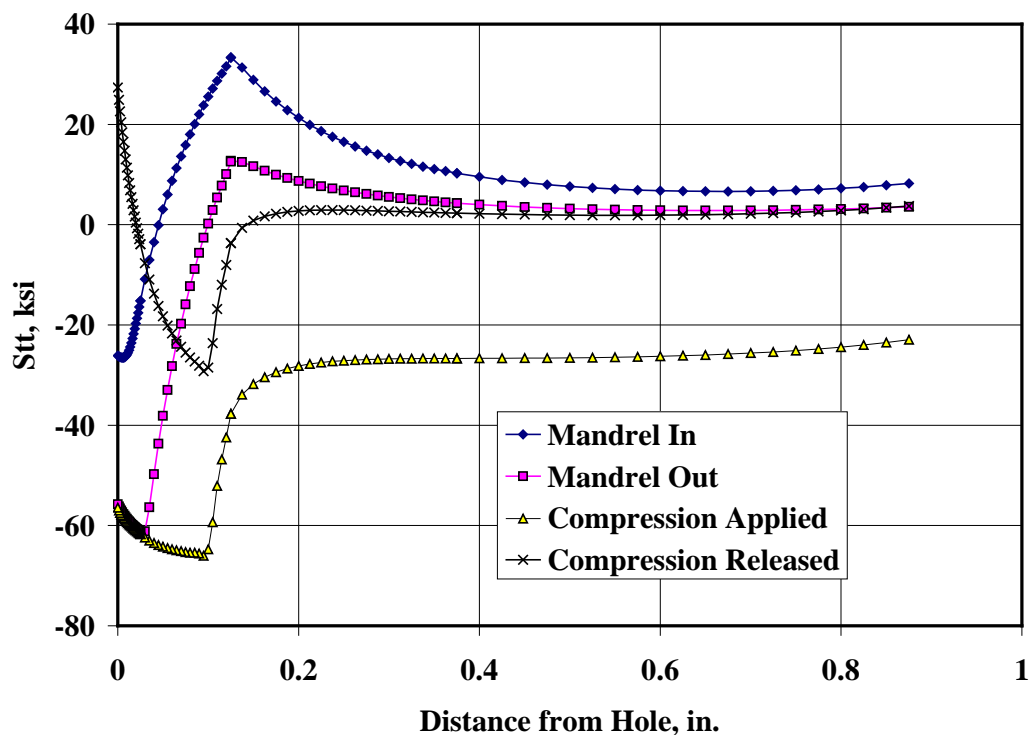


Figure 43. Relaxation of Residual Stresses by Compression Loads

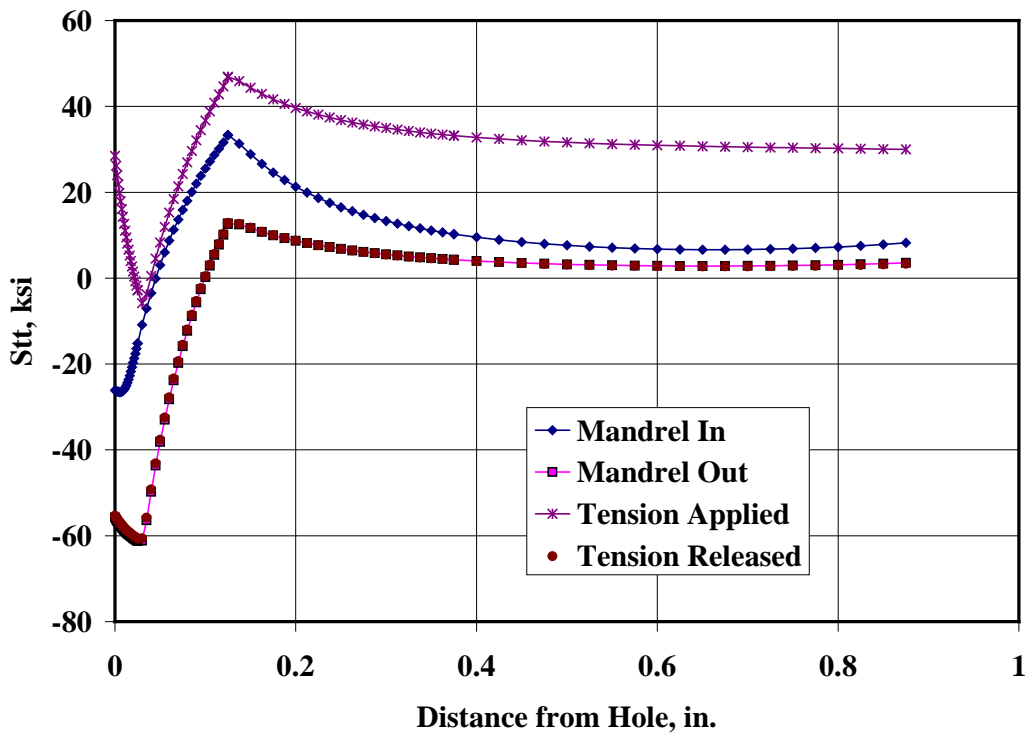


Figure 44. Relaxation of Residual Stresses by Tension Loads

5.2 Prediction of non CX coupon lives

A retro-diction of the AA2024 non CX coupon lives is summarized here. The fatigue load was 25 ksi gross stress (directly upstream of the hole) with stress ratio R=0.0. Each coupon was notched with EDM, pre-pre-cracked to approximately 0.025 in. X 0.035 in., finally reamed to 0.25 in. diameter, to correspond approximately to the final ream diameter of a 4% CX hole. All three (3) coupons failed in the neighborhood of 20,000 cycles. Two life “retro-dictions” (so-called because the life predictions were made with the a priori knowledge of the actual lives) were tried—each life prediction used the surface and bore crack measurements as initially measured with the traveling microscope at cycle 0. The first model, Model A in Table , made no effort to account for possible residual stresses that might be present due to the high gross stress, 25 ksi (which yielded a $K_t\sigma \approx 80$ ksi , almost 40% above the 0.2% yield for this material, 58 ksi); the predicted lives were close to 7,000 cycles for all, about 1/3rd of the measured lives. The second model, Model B, used a residual stress computed with StressCheck as input to the AFGROW residual stress interface (Table A-3 in the Appendix of this report), and predicted the lives again from the initial measured crack length. The results were more encouraging, Table 23, in which the predictions were within 28% of all measured lives.

Table 21. Summary of Retro-dictions

Coupon	Surface	Bore Pre-	Fatigue Life,	Model A	Model B
	Pre-crack, in.			Retro-diction, No Residual Stress, cycles	Retro-diction, Residual Stress, cycles
2H20	0.02628	0.03418	22,847	7,073	23,972
2H33	0.02914	0.03640	20,597	6,896	23,431
2H34	0.02472	0.03482	18,616	7,104	23,919

The end states (the measured and predicted lives) are very important, of course, however, we think that being able to predict the crack “path” is almost as important; a typical result, this for coupon 2H33, is shown in

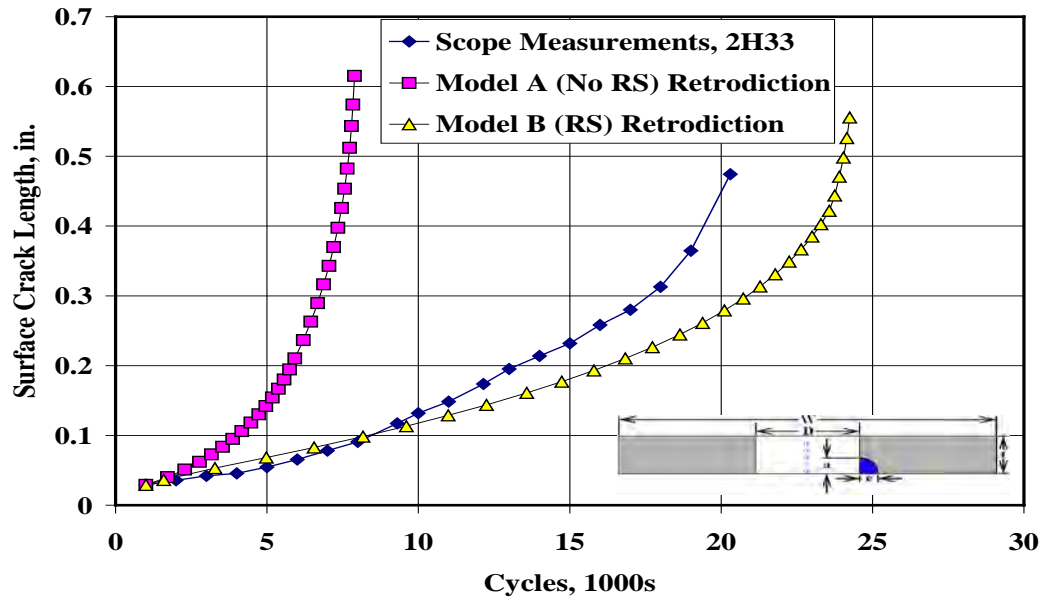


Figure 45, demonstrating a reasonably accurate life prediction capability is obtained when the residual stress is accounted for in the model.

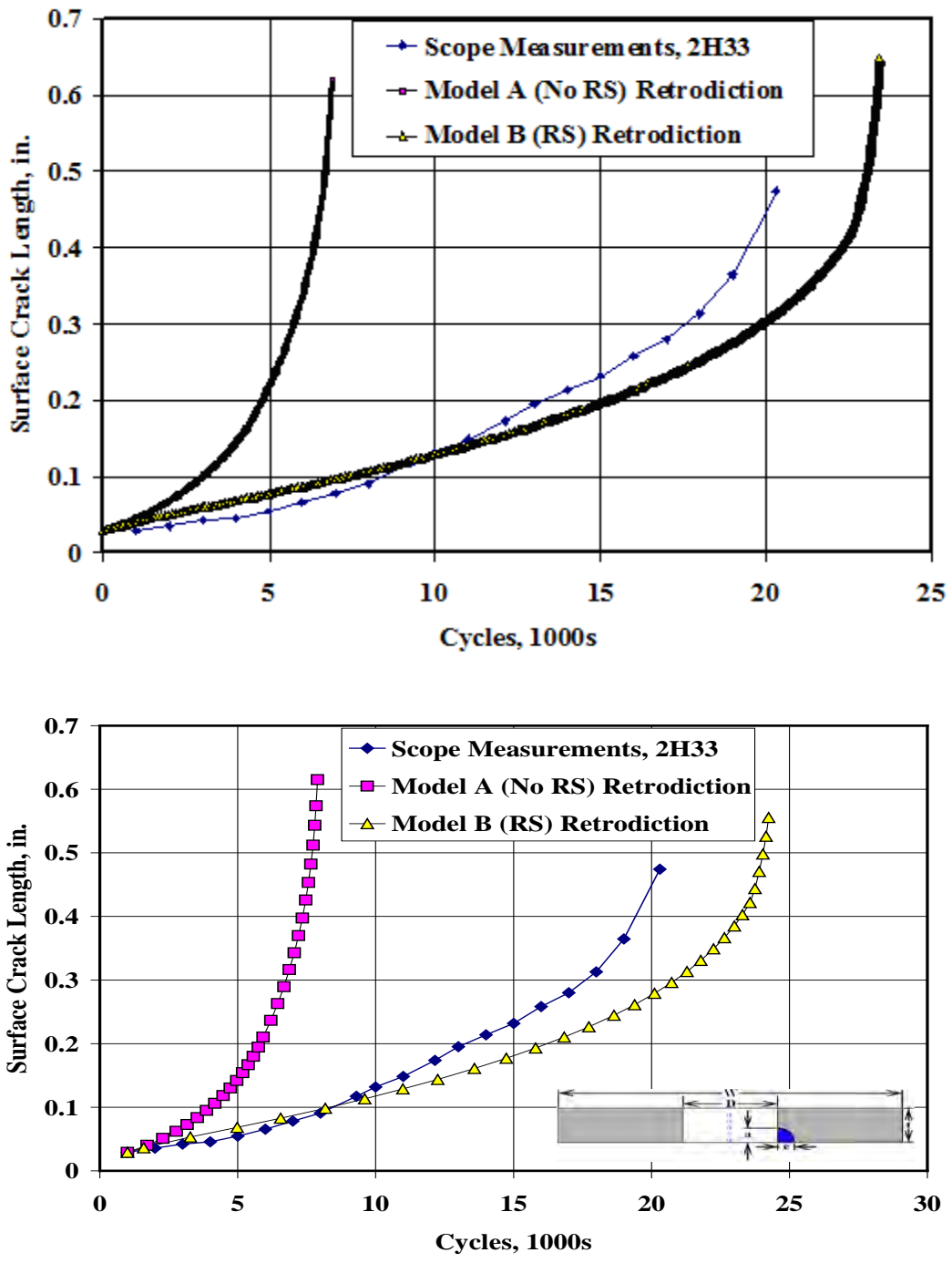


Figure 45. Comparison of Two Prediction Methods to the Measured Surface Crack Lengths, Coupon 2H33

5.3 Calculation of Residual Stress Intensity Factors from Traveling Microscope Measurements

The traveling microscope measurements made during Task 2 were used to compute the crack growth rates for the measured crack lengths (surface and bore). This section documents the methods used to compute the residual Stress Intensity Factors K_{res} , and the retro-dictions of crack propagation in the coupons with naturally occurring cracks, that were tested prior to the coupons with traveling microscope measurements.

5.3.1 Modeling

5.3.1.1 Coupon Design

The coupon is made of AA2024-T351 0.25 inch plate, and is a dogbone, tapering from 3 inches to 2 inches wide at the narrowest (gage) section, Figure 46. A 0.25 inch hole is drilled in the center of the gage section. If the hole is cold worked, the cold working (CX) level is nominally 4%.

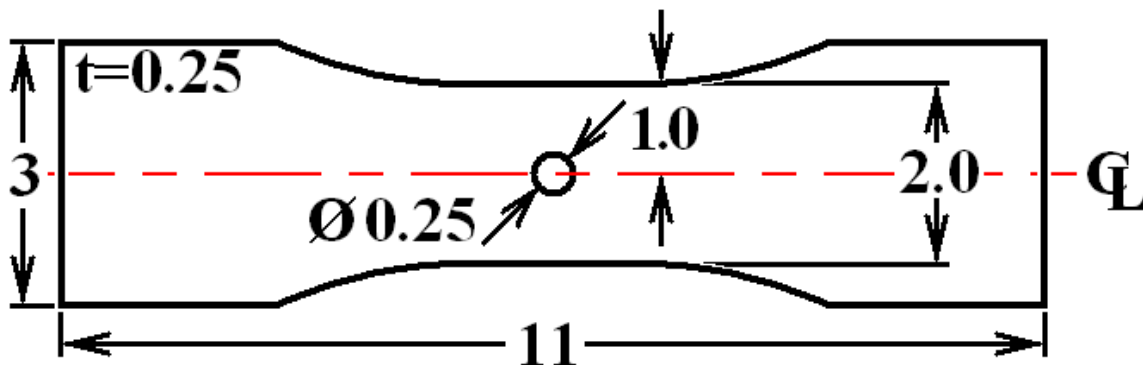


Figure 46. Schematic of Coupon Design. All dimensions are in inches

5.3.1.2 Material

The material is aluminum alloy 2024-T351, with a Young's modulus of $E = 10,625 \text{ ksi}$; this value of Young's modulus was measured in monotonic stress-strain tests conducted earlier in this program.

5.3.1.3 Traveling Microscope Measurements

A Gaertner traveling microscope was used to periodically record the crack growth (lengths and aspect ratios) of a crack that develops from the corner of the hole in the coupon schematically represented in Figure 46 above. After the hole was drilled, one of two procedures was used to finish processing the coupon: 1) if applicable, the coupon was cold worked nominally 4%, an EDM notch cut, the coupon pre-cracked, then the hole reamed to its final diameter (as specified by the FTI procedure for 4% cold working) or 2) an EDM notch cut, the coupon pre-cracked, the coupon cold worked to nominal 4% if applicable, and the hole cut to final reaming diameter. After the final ream, a constant amplitude load cycle of 25 ksi, $R=0$ was applied until the coupon failed. Crack growth measurements were generally made every 1,000 cycles if the coupon was not cold worked, and every 16,000 cycles if the coupon was cold worked. The matrix of coupons prepared one of these two ways and then tested to failure is shown in Table 24 below.

Table 22. Test Matrix for Traveling Microscope Measurements

Coupon	Applied Stress, ksi	Stress Ratio	Measured Life	Processing
2H20	25.00	0.00	22,847	No Cx, EDM, Pre-crack, FinalReam
2H33	25.00	0.00	20,597	No Cx, EDM, Pre-crack, FinalReam
2H34	25.00	0.00	18,616	No Cx, EDM, Pre-crack, FinalReam
2H14	25.00	0.00	180,066	4% Cx, EDM, Pre-crack, FinalReam
2H10	25.00	0.00	126,587	4% Cx, EDM, Pre-crack, FinalReam
2H09	25.00	0.00	65,890	4% Cx, EDM, Pre-crack, FinalReam
2H08	25.00	0.00	121,312	4% Cx, EDM, Pre-crack, FinalReam
2H15	25.00	0.00	176,893	EDM, Pre-crack, 4% Cx, FinalReam
2H16	25.00	0.00	137,640	EDM, Pre-crack, 4% Cx, FinalReam
2H17	25.00	0.00	110,553	EDM, Pre-crack, 4% Cx, FinalReam
2H18	25.00	0.00	131,931	EDM, Pre-crack, 4% Cx, FinalReam
2H19	25.00	0.00	138,257	EDM, Pre-crack, 4% Cx, FinalReam

There appears to be only a small effect of the processing procedure, as the average lives varied only from 123,464 cycles (for coupons first cold worked, then pre-cracked) to 139,055 cycles (for coupons first pre-cracked, then cold worked). However, there was a larger variation in the standard deviation, varying from 38% for the coupons that were first cold worked to 17% of the average for the coupons first pre-cracked.

5.3.1.4 AFGROW Simulations

5.3.1.4.1 Crack Model

The crack scenario is AFGROW's Single Corner Crack at Hole model, Figure 47.

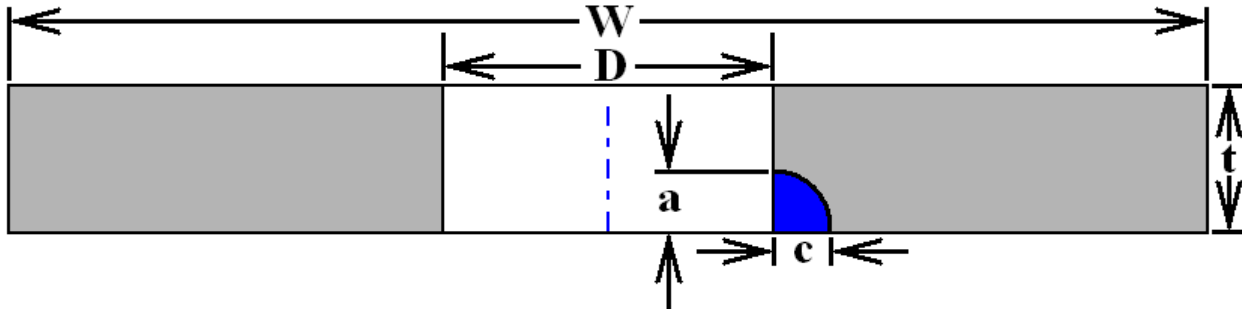


Figure 47. Schematic of Fracture (Crack) Plane. $W = 2.0 \text{ in.}$, $D = 0.25 \text{ in.}$, $t = 0.25 \text{ in.}$

AFGROW models were used for both the K_{res} computations and for retro-dictions of the EDM notched and naturally occurring crack coupons.

5.3.1.4.2 Crack Growth Rates

The crack growth rates represent the APES state of the art curve fits for AA2024-T351, Figure 48. These crack growth rates were obtained from an MACS-IDS matching procedure that used

measured failure flaw sizes and coupon lives to calibrate the material crack growth rates and initial (computed) flaw sizes. The basic procedure idea is that several coupons of a material are tested to material, and post-failure fractography is used to identify failure origins and the size of the flaw at the failure origin. The distribution of “failure flaws” or Initial Discontinuity States (IDS) is compared to the distribution of “Equivalent Initial Flaw Size (EIFS)” that are computed using known fatigue crack growth curves. The distribution of computed EIFS is compared to the measured IDS, the fatigue crack growth rates adjusted, a new EIFS distribution is computed, compared to the IDS, the fatigue crack growth rates adjusted again, and the matching procedure continues until the distributions of the computed EIFS and the measured IDS are reasonably close. The MACS-IDS matching procedure is discussed in a paper by Mills, et al [18], that accompanied the proceedings of the Aircraft Structural Integrity Program (ASIP) Conference of 2004, which was held in Memphis TN.

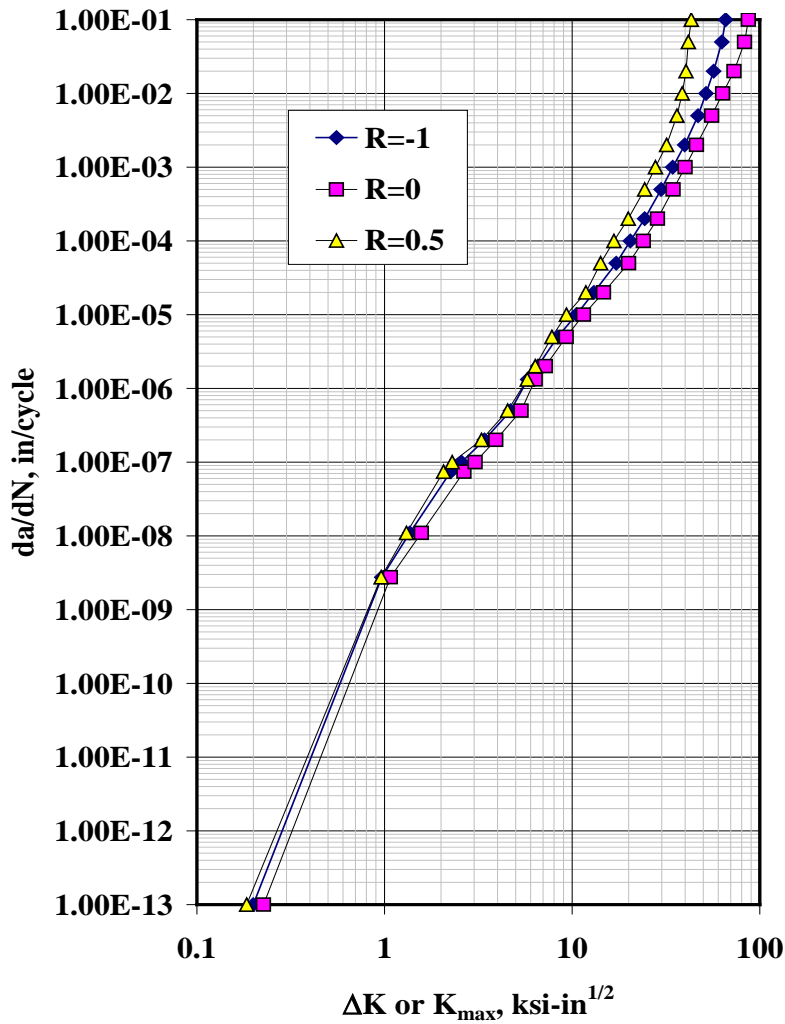


Figure 48. Crack Growth Rates for AA2024-T351, EIFSv8.lkp. All Values of Stress Intensity Factor (x-axis) are ΔK if $R \geq 1$, K_{\max} if $R < 1$

5.3.1.4.3 AFGROW Inputs

AFGROW simulations executed in an Excel VBA worksheet which calls an AFGROW input file (.dax), the load spectrum (.sp3), the material crack growth rate file (.lkp), and the residual stress file (.sd3) and computes coupon lives. Initial flaw sizes for the simulations are the pre-crack dimensions measured in the fatigue tests with the traveling microscope.

5.3.1.5 Residual Stress Intensity Factors Estimates

The residual Stress Intensity Factors (K_{res}) in both non cold worked and cold worked coupons were computed by using the average crack growth rates (da/dN) of the measured crack lengths and the AFGROW computed SIFs for the same crack lengths. AFGROW uses the residual stress intensity factors (K_{res}) in the following way: the K_{res} is added to each cycle SIF, K_{max} and K_{min} :

K_{min} :

$$\Delta K = (K_{max} + K_{res}) - (K_{min} + K_{res}) = K_{max} - K_{min} \quad (1)$$

This leads to the conclusion that the difference between K_{max} and K_{min} , which can be computed from the applied stress levels and the measured crack lengths, do not change in a given load cycle. However, the effective stress ratio, R_{eff} , does vary because of the K_{res} :

$$R_{eff} = \frac{(K_{min} + K_{res})}{(K_{max} + K_{res})} \quad (2)$$

The procedure to calculate the K_{res} is complicated by the stress ratio effect in fatigue crack growth rate (FCGR) data—if you plot the measured FCGR against ΔK , which stress ratio do you use to compute the reduction in SIF needed to get the correct FCGR? For instance, coupon 2H08 at measured crack lengths $c = 0.07116$ in. and $a = 0.08384$ in. has computed $da/dN = 1e - 6$ in./cycle. At those crack lengths, AFGROW reports $\Delta K = 15.693$ ksi-in $^{1/2}$ at $R = 0$. At this FCGR, ΔK can vary from $\Delta K = 5.37$ ksi-in $^{1/2}$ at $R = 0.5$ to from $\Delta K = 10.93$ ksi-in $^{1/2}$ at $R = -1$ —in this instance, the residual SIF K_{res} can vary from $K_{res} = 10.323$ ksi-in $^{1/2}$ to $K_{res} = 4.763$ ksi-in $^{1/2}$. Here we assume $R = -1$; using K_{max} , the residual SIF K_{res} is the difference between the AFGROW computed SIF (that is, the crack dimensions are known—compute the AFGROW SIF using those crack dimensions), and the effective K_{max}^{eff} :

$$K_{res} = K_{max}^{AFGROW} - K_{max}^{eff} \quad (3)$$

Residual SIFs were computed for each of the three (3) non cold worked and the nine (9) cold worked coupons for both the “a” and “c” crack propagation—a quadratic curve was fit to the two sets, one for each crack tip—the resulting residual SIFs for the non cold worked coupons, Table 25, and for the cold worked coupons, Table 26, were used in the life retro-dictions that follow this section. The two key assumption are: 1) if the quadratic polynomial fit predicted a positive residual SIF, then the Residual SIF is zero (0.0), and 2) we had no knowledge of the crack growth behavior for cracks smaller than the pre-crack size (approximately 0.02 inches for each

coupon); therefore we could only make a reasonable guess as the behavior of K_{res} for cracks smaller than the pre-crack—we have chosen to use a linear ramp from crack lengths of 0.01 inches back to zero (0.0) at crack length of 0.0 inches.

Table 23. Residual K K_{res} for Each Crack Tip. Non Cold Worked

r in.	K_{res-c} ksi-in^{1/2}	K_{res-a} ksi-in^{1/2}	r in.	K_{res-c} ksi-in^{1/2}	K_{res-a} ksi-in^{1/2}
0	0	0	0.05	-4.014	-5.66105
0.001	-0.32525	-0.46681	0.06	-4.20438	-5.90928
0.002	-0.6505	-0.93363	0.08	-4.58514	-6.40574
0.003	-0.97574	-1.40044	0.1	-4.9659	-6.9022
0.004	-1.30099	-1.86725	0.15	-5.9178	-8.14335
0.005	-1.62624	-2.33407	0.2	-6.8697	-9.3845
0.006	-1.95149	-2.80088	0.3	-8.7735	-11.8668
0.007	-2.27674	-3.26769	0.4	-10.6773	-14.3491
0.008	-2.60198	-3.7345	0.5	-12.5811	-16.8314
0.009	-2.92723	-4.20132	0.6	-14.4849	-19.3137
0.01	-3.25248	-4.66813	0.8	-18.2925	-24.2783
0.02	-3.44286	-4.91636	0.875	-19.7204	-26.14
0.04	-3.82362	-5.41282			

Table 24. Residual K K_{res} for Each Crack Tip. Cold Worked

r in.	K_{res-c} ksi-in^{1/2}	K_{res-a} ksi-in^{1/2}	r in.	K_{res-c} ksi-in^{1/2}	K_{res-a} ksi-in^{1/2}
0	-7.0993	-0.9065	0.05	-10.0738	-8.2962
0.001	-7.1664	-1.07791	0.06	-10.5755	-9.48499
0.002	-7.23319	-1.24835	0.08	-11.4858	-11.5734
0.003	-7.29967	-1.41783	0.1	-12.2718	-13.2763
0.004	-7.36584	-1.58635	0.15	-13.6933	-15.8468
0.005	-7.43169	-1.7539	0.2	-14.3383	-16.0077
0.006	-7.49724	-1.92049	0.3	-13.2988	-9.1007
0.007	-7.56248	-2.08612	0.4	-9.1533	0
0.008	-7.6274	-2.25078	0.5	-1.9018	0
0.009	-7.69202	-2.41447	0.6	0	0
0.01	-7.75632	-2.57721	0.8	0	0
0.02	-8.38228	-4.15153	0.875	0	0
0.04	-9.54102	-7.01103			

The computed K_{res} from these two tables are plotted in Figure 49 and Figure 50 below.

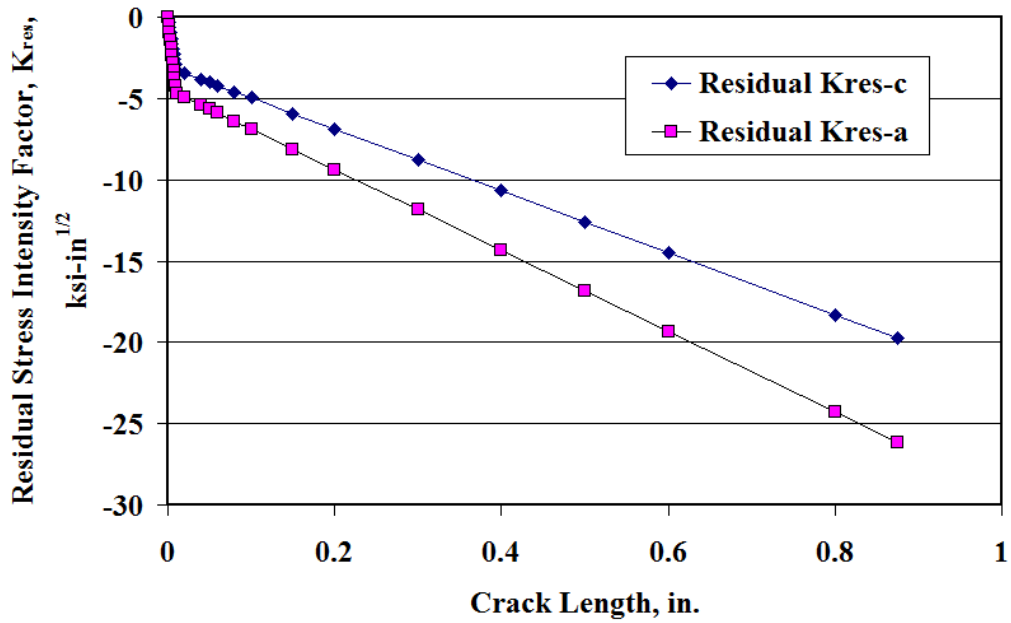


Figure 49. Residual Stress Intensity Factors for Crack-c and Crack-a. Non Cold Worked

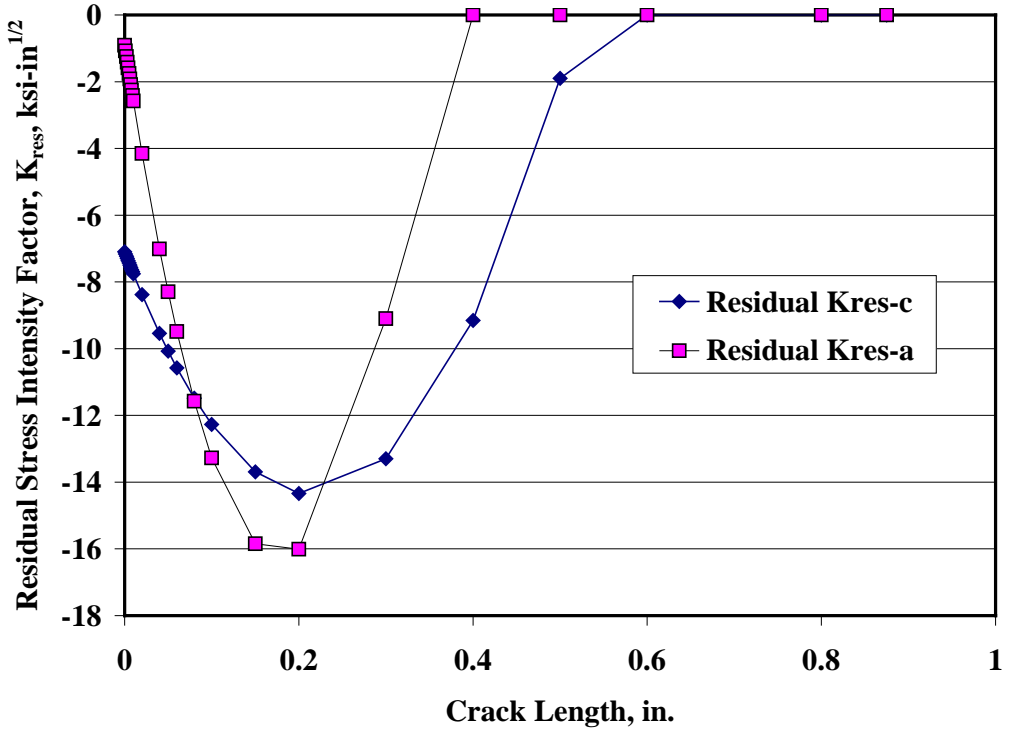


Figure 50. Residual Stress Intensity Factors for Crack-c and Crack-a. Cold Worked

5.3.2 Results and Discussion

5.3.2.1 Correlation with Pre-Cracked Coupons

The residual stress intensity factors in the previous section were used to estimate the fatigue lives of the EDM notched coupons. In principle, the correlation would be perfect; in practice, only one residual SIF distribution was used to “retro-dict” the coupon lives. The fatigue tests with pre-crack dimensions are summarized in Table 27 below. –these are non CX and CX coupons.

Table 25. Summary of Measured Fatigue Lives and Retro-dictions Using K_{res}

Coupon ID	Bore Crack, in.	Surface Crack, in.	Measured Fatigue Life, cycles	Retro-dictions, cycles
2H20	0.02628	0.03418	22,847	21,611
2H33	0.02914	0.03640	20,597	21,072
2H34	0.02472	0.03482	18,616	21,687
2H08	0.03486	0.0281	121,312	166,500
2H09	0.04136	0.02166	65,890	169,164
2H10	0.03204	0.022	126,587	173,015
2H14	0.02936	0.02032	180,066	176,031
2H15	0.03556	0.01838	176,893	175,617
2H16	0.07736	0.02286	137,640	148,239
2H17	0.05872	0.04972	110,553	146,547
2H18	0.0768	0.04808	131,931	140,498
2H19	0.06248	0.05132	138,257	144,539

The results of simulations of all cold worked coupon tests are shown in Figure 51 below. The x-axis is “Cumulative Distribution Function” (CDF); the y-axis is the “Retro-dicted/Actual (Measured)” lives.

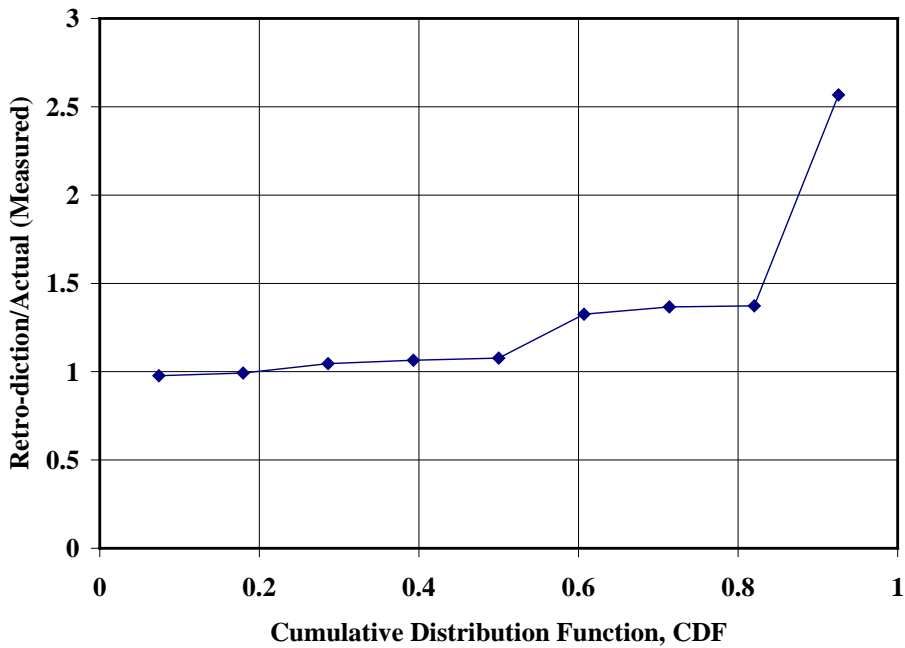


Figure 51. Correlation of Retro-dictions Using Residual SIFs to Measured Fatigue Lives. Cold Worked Coupons

5.3.2.2 Correlation with Naturally Occurring Cracks

A key indication of the ability of this Residual SIF model is to predict the lives of coupons of which crack growth was NOT measured. In this project, we had several AA2024-T351 coupons that were tested to failure; but no EDM notches were cut, that is, all failure flaws were naturally occurring cracks. Retro-dictions using the residual SIFs of Figure 49 (if non cold worked) and Figure 50 (if cold worked) were accomplished on the following coupon test results, Table 28:

Table 26. Coupon Test Results

Coupon	CX	Max. Stress, ksi	Stress Ratio, R	Spectrum	Life, cycles
2H01	No	25	0	CA	44,121
2H03	No	25	0	CA	37,915
2H04	No	25		VA, MB18	91,469
2H05	4%	25	0	CA	195,695
2H06	No	25	0	CA	39,020
2H35	No	22.5		MB-DIC	181,845
2H36	4%	28.75		MB-DIC	765,380
2H54	4%	28	0.1	CA	160,039

Because the cracks are naturally occurring, the initial crack dimensions used to compute the lives are in the range P(0.1) to P(0.9) IDS, Table 29.

Table 27. Initial Crack Dimensions. AA2024-T351 IDS

P	Crack Dimension, $a=c$, in.
0.1	0.000676
0.5	0.000959
0.9	0.001402

The retro-dictions using Figure 49 (if non cold worked) and Figure 50 (if cold worked) K_{res} for these coupons with naturally occurring cracks are summarized in Table 30.

Table 28. Retro-dictions of Coupon Lives

Coupon	Life, cycles	Retro-diction, cycles, P(0.1)	Retro-diction, cycles, P(0.5)	Retro-diction, cycles, P(0.9)
2H01	44,121	298,312	289,489	281,582
2H03	37,915	298,312	289,489	281,582
2H04	91,469	437,005	424,095	412,151
2H05	195,695	298,312	289,489	281,582
2H06	39,020	298,312	289,489	281,582
2H35	181,845	>5,000,000	>5,000,000	>5,000,000
2H36	765,380	801,863	787,959	775,238
2H54	160,039	122,831	116,912	111,232

The P/A are sorted and plotted in Figure 52 below against the “Cumulative Distribution Function (CDF)”; the only predictions that are close to the actual measured lives are for the P(0.9) crack, $a = c = 0.001402$ in.

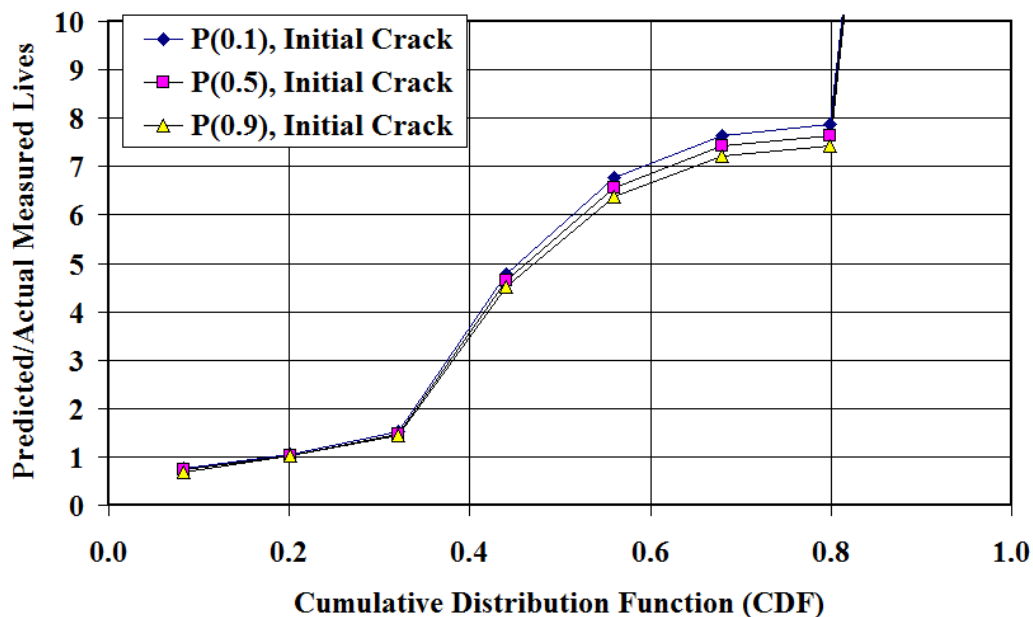


Figure 52. Correlation of Retro-dictions to Measured Fatigue Lives, Naturally Occurring Cracks

5.3.3 Conclusions

This section summarized the predictions of non cold-worked and cold-worked AA2024-T351 coupons lives that used estimates of residual K (K_{res}) derived from traveling microscope measurements. Traveling microscope measurements of crack growth rates and AFGROW computations of Stress Intensity Factors for measured crack lengths were used to compute first an effective stress ratio R_{eff} , and then a K_{res} associated with the measured crack lengths. These derived K_{res} were used in new “retro-dictions” of the coupon lives for both EDM/pre-cracked coupons and naturally occurring crack growth in AA2024.

6 Relaxation/Redistribution Effects (Task 6)

6.1 Preliminary Digital Image Correlation

In preparation for the contour method measurements of the residual stress fields in interrupted testing, cold worked coupons were imaged with DIC and strain fields computed at predetermined number of applied load cycles. Two sets of DIC images, one for the ‘left’ side of the hole (Figure 53) and one for the ‘right’ side of the hole (Figure 54) are representative. The DIC measurements appear to be showing some relaxation in the strain fields, but the differences between the initial strain fields and the strain fields at 100,000 cycles are within the “noise floor” measured earlier and reported in Figure 25.

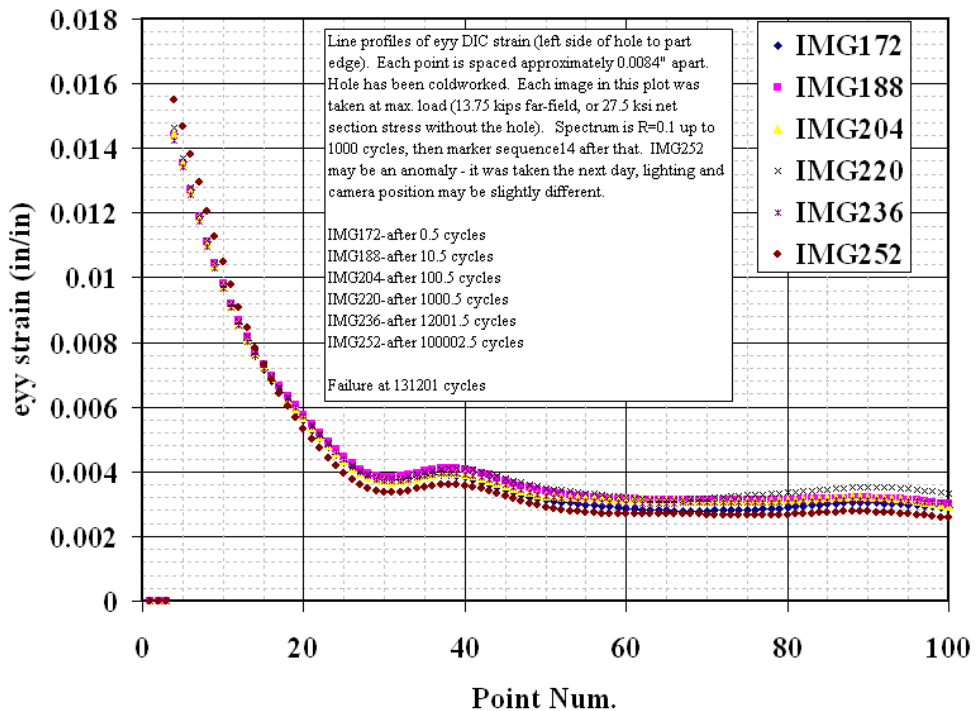


Figure 53. Strain Measured at Periodic Fatigue Cycle Intervals. eyy-left

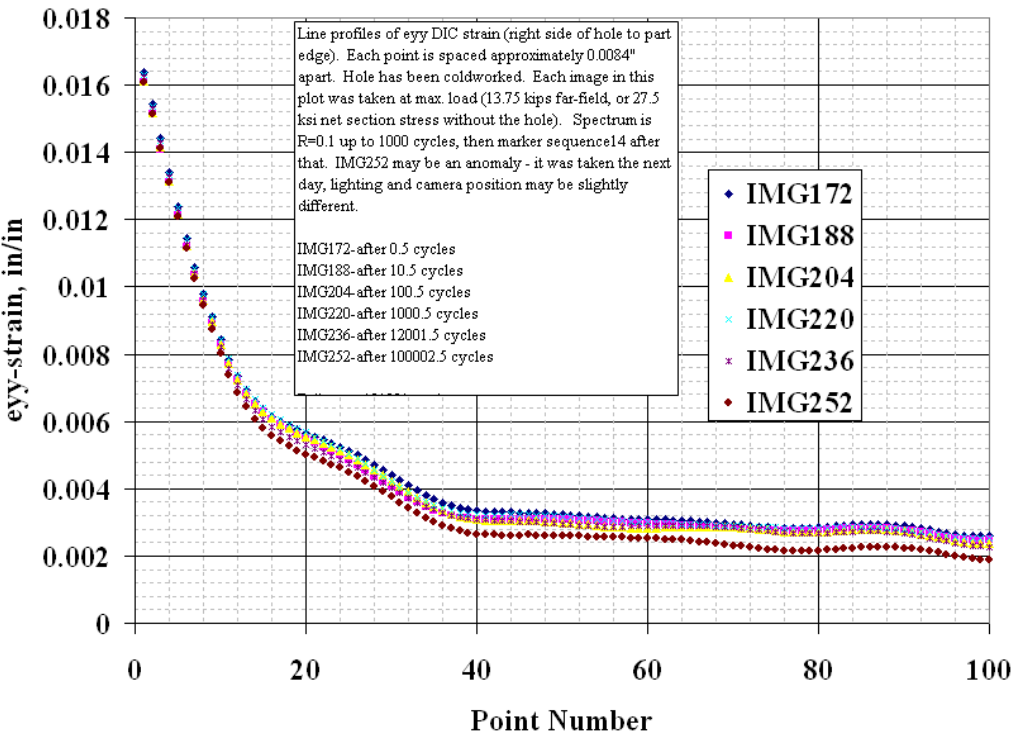


Figure 54. Strain Measured at Periodic Fatigue Cycle Intervals. eyy-right

Two-dimensional (2-D) Image Correlation (IC) system was used to investigate the potential relaxation of residual stresses induced by cold expansion of a fastener hole. The residual stresses and strains at a fastener hole due to the cold expansion process have been well documented in literature. However, persistence of those residual stresses is often a question; in other words, do these residual stresses and strains lose their effectiveness due to environmental factors, age, fatigue cycles, or other mechanism?

A fatigue test of a dogbone coupon (2H05) with a cold expanded central hole was conducted at 25 ksi net section stress, $R=0$. Collections of images for IC were captured before and after cold expansion, then again after every 10,000 applied stress cycles. The collections of images generally consisted of 6 to 12 images each, taken at approximately 6 Hz while the test machine was in a load dwell. The specific number of images in each collection varied due to noise in the camera's analog trigger voltage. For every image in every collection, the IC y-direction surface strains were obtained at 101 equally-spaced points along the extraction line, Figure 55 (note 101 equally spaced points space approximately 2 inches, minus the hole width). For every point, the mean and standard deviation of each collection were computed to help characterize the noise in the IC measurement system.

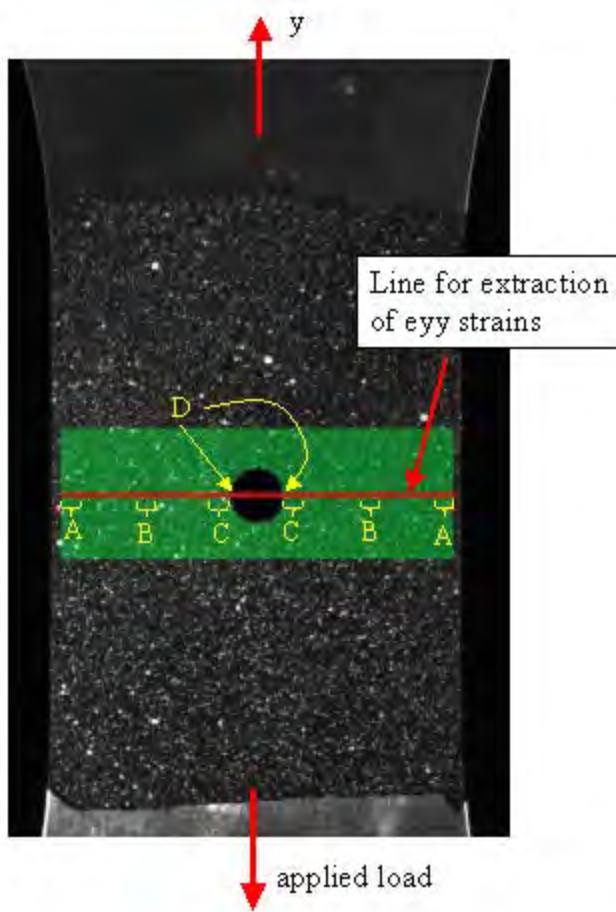


Figure 55. Location of Strain Results

Since the interest here is in relaxation, or changes, in stresses and strains as loading progressed, two different reference IC images were used. First, for all zero-load dwells interspersed during cycling, the reference was the first zero-load condition after cold expansion (zero cycles). For all 25 ksi load dwells interspersed during cycling, the reference image was the first 25 ksi load after cold expansion (one-half of one cycle). Since the strains reported by the IC system are always relative to the reference image, the results shown here will NOT show those strains due purely to cold expansion, or those strains due purely to a 0 ksi to 25 ksi half-load-cycle.

Figure 55 shows the locations of several groups of points that were examined, and were plotted in Figure 56, Figure 57, and Figure 58. In the Figure 56, Figure 57, and Figure 58 Legends, the curves marked "All points" are the mean strain (for each collection) at all 101 points that was again averaged along the extraction line. Points falling inside the hole were not used. Group A is an average of 10 points, 5 at each edge of the extraction line. Group B is an average of the 10 points, 5 between the hole and each edge of the specimen. Group C is an average of 10 points, 5 on each side of the hole. Group D is an average of the two single points next to the hole.

Results are presented in Figure 56 and Figure 57. These figures present the changes in average IC strain from each reference image, as fatigue cycles accumulate on the specimen. Figure 56 results show a slight upward bias, where the strains are increasing slightly in time. However, the magnitude of this increase is quite small, only about 0.0001 inches/inch at 100,000 cycles for

groups A and B. The typical standard deviation (1-sigma) value within each collection is also around that value, leading one to conclude that the strain changes may be within the noise of the system, and not representative of positive strain ‘creep’, which would lead to relaxation of residual stresses. It is suspected that the upward trend after 100,000 cycles is due to cracking in the specimen, which is seen more easily in Figure 57. At zero load dwell, any existing crack in the specimen is likely not fully closed due to the plastic zone around the crack front and asperities along the crack front, so it is not surprising that groups C and D (at the crack origin) show some positive strain changes.

Figure 57 shows the strain changes with cycling, measured at the peak load value (25 ksi). With this set of images, a large fatigue crack can be clearly seen on the left side of the hole in the IC images near the end of the specimen life. This crack, when held open at 25 ksi, is causing the large strain changes shown in groups C and D at 190,000 cycles in Figure 57. Most likely, it is the primary cause of all strain changes in Figure 56 and Figure 57. IC contour plot results seem to indicate a small fatigue crack on the right side of the hole beginning at around 40,000 cycles. Fatigue cracking on the left side of the hole is suggested by IC contour plots at around 110,000 cycles. Figure 58 seems to reinforce this, as the right-side results show a strain-change indication before the left side, but then the left-side crack becomes larger and dominant, and eventually causes specimen failure.

In summary, strain and residual stress relaxation does not appear to be occurring during this test, especially not at cycle counts less than 50,000 cycles. If relaxation is occurring, it is of a fairly low magnitude and may not be detectable by IC or slitting methods. The changes in strain shown in Figure 56 and Figure 57 are most likely due to fatigue cracking. A similar experiment to this one is planned using a non-cold worked specimen, to verify that the changes in strains shown here are indeed due to cracking and not due to residual stress relaxation.

A sequence of IC images can sometimes be used to observe cracking behavior. A video clip was made that cycles between two IC images: the first is at 25 ksi dwell after 180,000 cycles, the second is at 25 ksi dwell after 190,000 cycles. This clip shows the dominant left-side crack growth that occurred during these 10,000 cycles. The clip is available for download at:

<http://www.apesolutions.com/spd/clip0006.avi>--copy and paste this address into the URL window of your web browser and reply “Save” to save the file to your computer. You can watch the video file with any number of media players; we used Windows Media Player 11 and it worked fine.

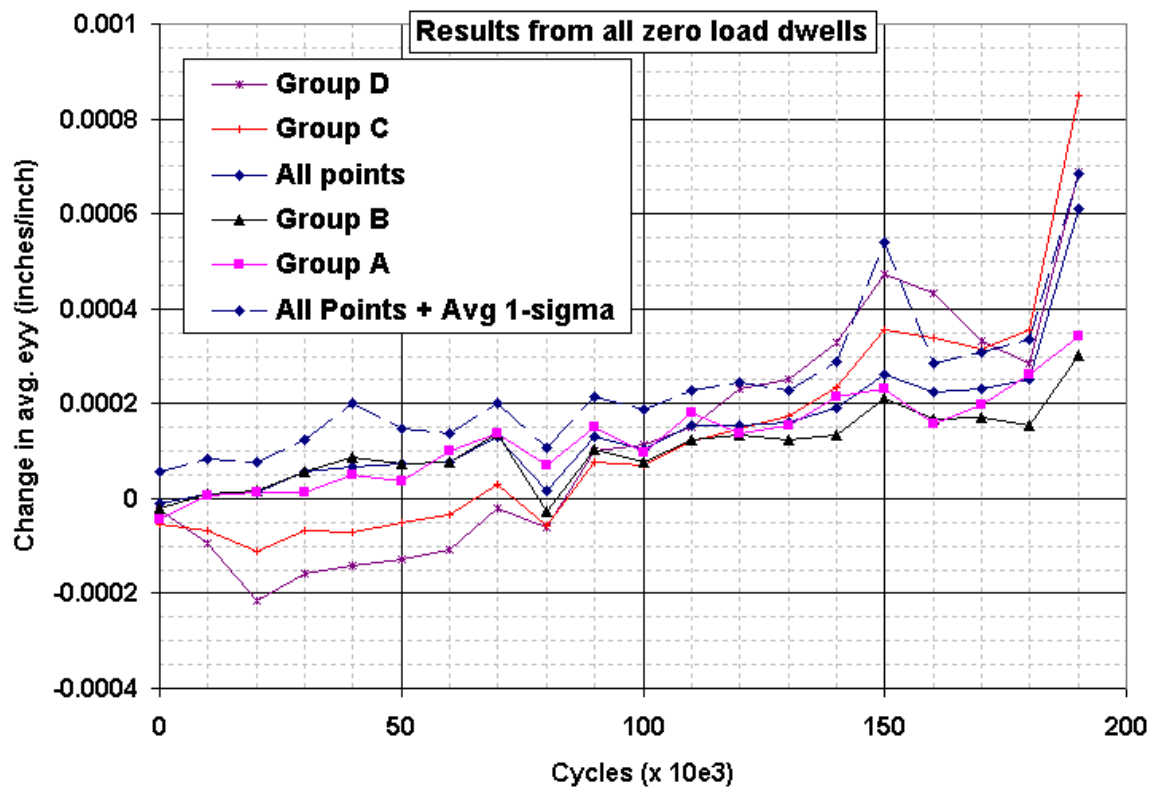


Figure 56. Strain Changes with Cycling, Measured During Zero Load Dwells

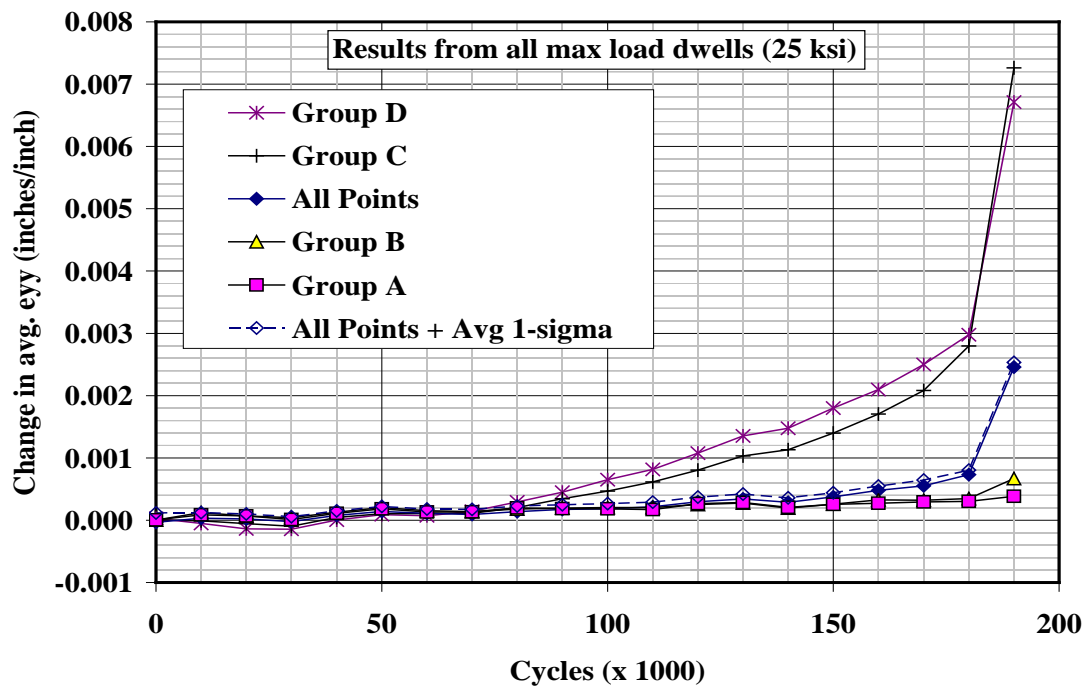


Figure 57. Strain Changes with Cycling, Measured During 25 ksi Load Dwells

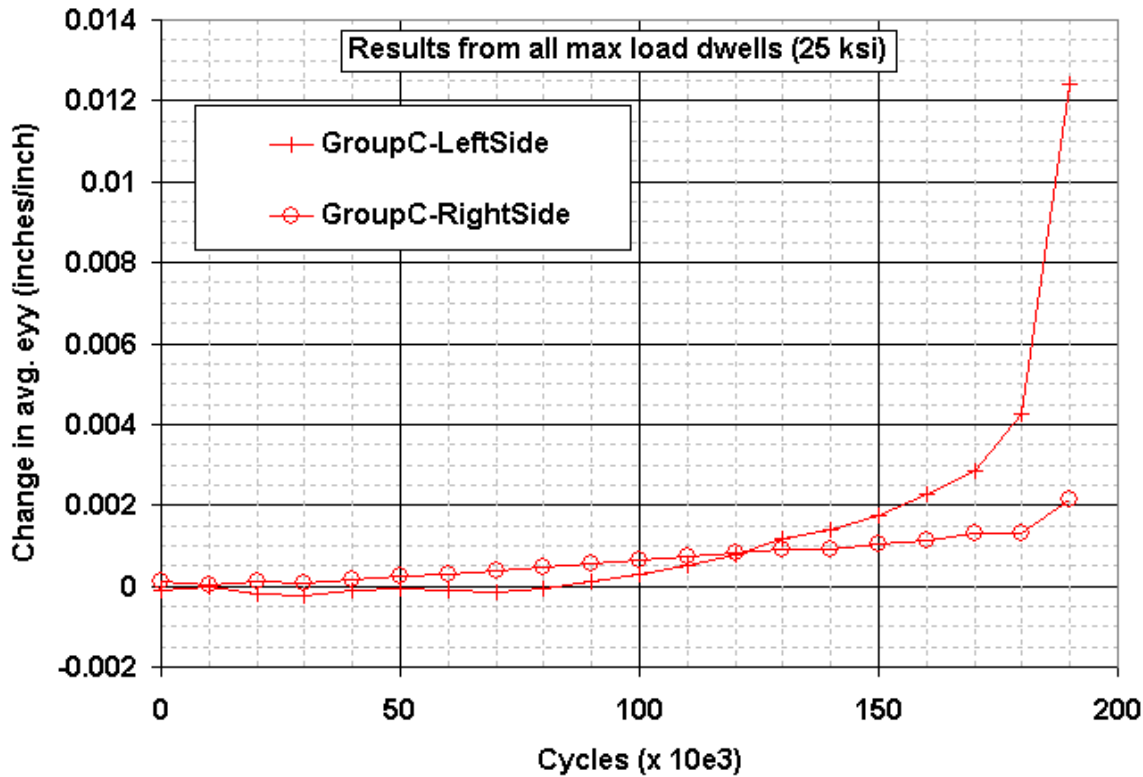


Figure 58. Strain Changes Adjacent to the Hole

6.2 Contour Method Measurements

Contour Method measurements were made on twelve (12) dogbone coupons, each with a hole centered in the gage (narrow) section. Three (3) of the coupons were not cold worked; the other nine (9) were cold worked. The non cold worked coupons were not loaded with fatigue cycles; the 9 cold worked coupons were fatigued to predetermined load cycles: 0, 100, 5,000 or 50,000 cycles. All contour method measurements were made by Hill Engineering, LLC, Rancho Cordova, CA.

6.2.1 Introduction

The Contour Method measurements were made on each coupon first by cutting a coupon with EDM at the measurement plane, then measuring the displacement of the plane with CMM, which will relax and deform outward due to the presence of residual stresses. The stresses normal to the surface can be determined for a 2D plane, in contrast to many residual stress measurements, which can measure stress only in a 1D direction. The fundamental idea of the Contour Method is that, after cutting the coupon, the measurement plane will deform slightly as it relaxes due to the residual stress on that plane. A finite element simulation uses the negative of the deformed surface as the imposed displacement boundary condition on the measurement plane, and with information about the material's constitutive behavior, the stresses that result from the application of the imposed displacement (which will deform the surface back to its original, flat shape) are assumed to be the residual stresses in the coupon before slicing the coupon up. More information about the method can be found in Ref. [16], which is one of the first, basic contour measurement references from Los Alamos.

Measurements were made on 12 dog bone coupons with cross sections typically like Figure 59. Three (3) coupons were not cold worked; the remaining nine (9) coupons were cold worked to 4%. Of the 9 coupons, three (3) were not cycled with loads, and the remaining six (6) were cycles with 25 ksi for varying number of cycles: 100, 5,000 or 50,000 cycles.

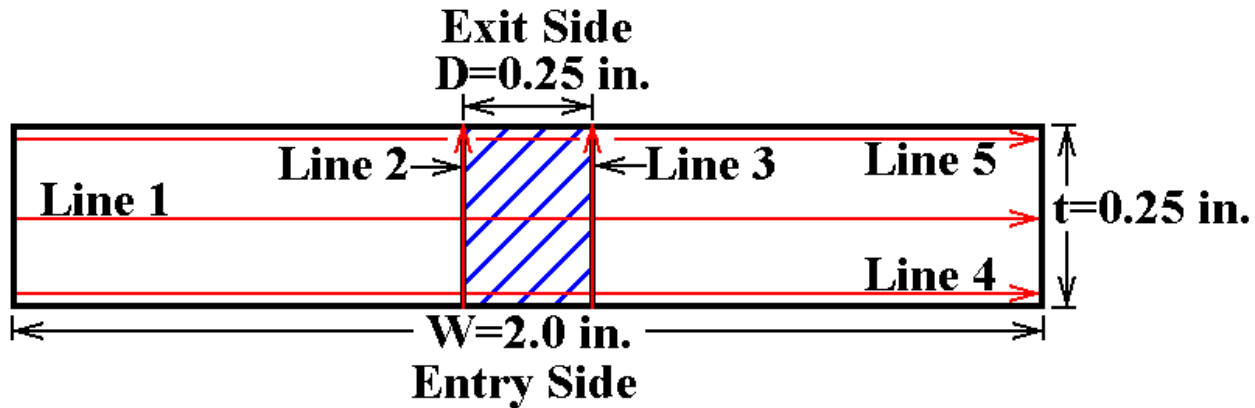


Figure 59. Measurement Plane Cross Section. Line 1 is “Mid Plane,” Line 2 is “Hole Edge Left,” Line 3 is “Hole Edge Right,” Line 4 is “Entry Side,” and Line 5 is “Exit Side”

The matrix of coupons, with corresponding cold working levels and number of fatigue cycles, is shown in Table 31.

Table 29. Coupon Matrix

Coupon		Number of	
ID	Cold Worked?	Load, ksi	Load Cycles
2H21	N	0	0
2H22	N	0	0
2H23	N	0	0
2H24	Y	0	0
2H25	Y	0	0
2H26	Y	0	0
2H27	Y	25	100
2H28	Y	25	100
2H29	Y	25	5,000
2H30	Y	25	5,000
2H31	Y	25	50,000
2H32	Y	25	50,000

Some figures below are identified in the Legends with “x2H% %” instead of “2H% %”; merely remove the “x” prefix to identify the correct coupon ID.

6.2.2 Results and Discussion

6.2.2.1 Contour Method Measurements by Hill Engineering

The Contour Method residual stress measurements are summarized in Figure 60,

Figure 61, Figure 62, Figure 63, and Figure 64 for the “Line 1,” “Line 2,” “Line 3,” “Line 4,” and “Line 5,” respectively, as identified in Figure 59 above. Each of the Figures contains the residual stress measurements for 3 coupons that have not been cold worked nor have they been loaded cyclically (these 3 coupons are representative of the “as-machined” state); 3 coupons that have been cold worked 4% (nominally) but not loaded cyclically; 2 coupons that have been cold worked 4% (nominally) and loaded cyclically for 100 cycles at 25 ksi; 2 coupons that have been cold worked 4% (nominally) and loaded cyclically for 5,000 cycles at 25 ksi; and 2 coupons that have been cold worked 4% (nominally) and loaded cyclically for 50,000 cycles at 25 ksi.

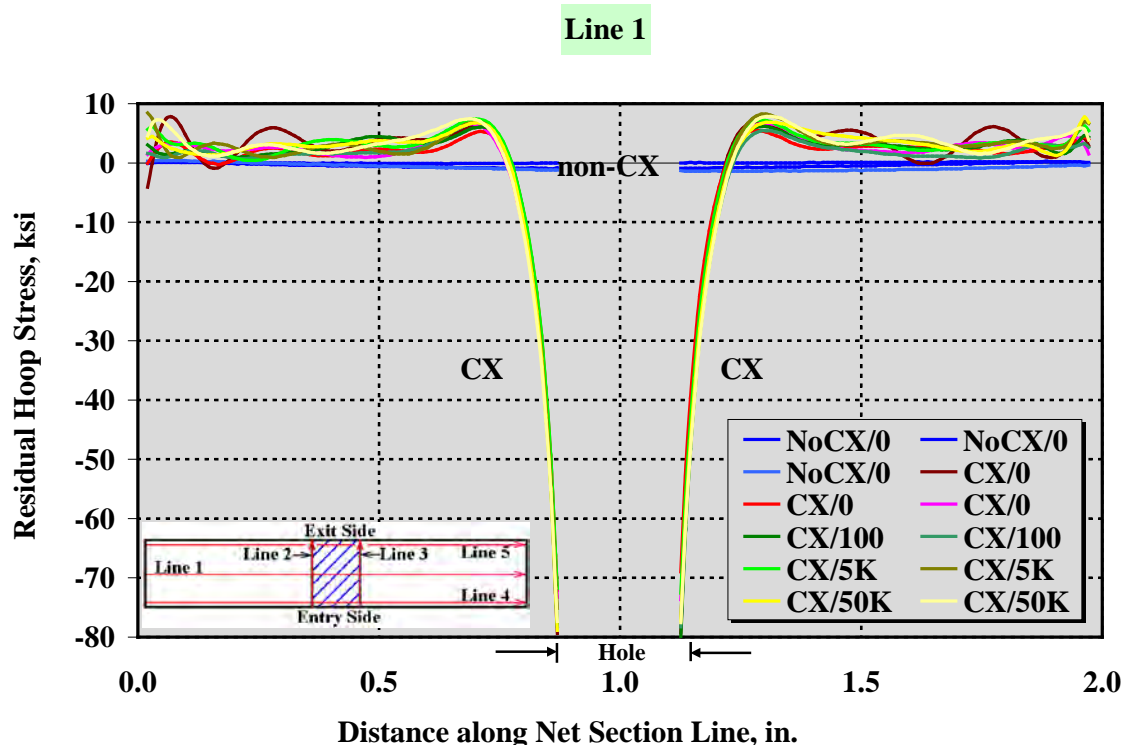


Figure 60. Mid Plane Residual Stress Measurements, Line 1. 2H21-3 are not cold worked or cyclically loaded, 2H24-6 are cold worked but not cyclically loaded, 2H27-8 are cold worked and loaded for 100 cycles, 2H29-30 are cold worked and loaded for 5,000 cycles, and 2H31-32 are cold worked and loaded for 50,000 cycles

Line 1 is the Mid Plane of the coupon, beginning at the left free edge, continuing through the hole, and extending all the way to the right free edge, Figure 60. The residual stress in non cold worked coupons, 2H21, 2H22 and 2H23, is near zero, as identified by the bluish lines in Figure 60. The residual stress in the cold worked coupons is clearly much larger than in the non cold worked coupons, as expected.

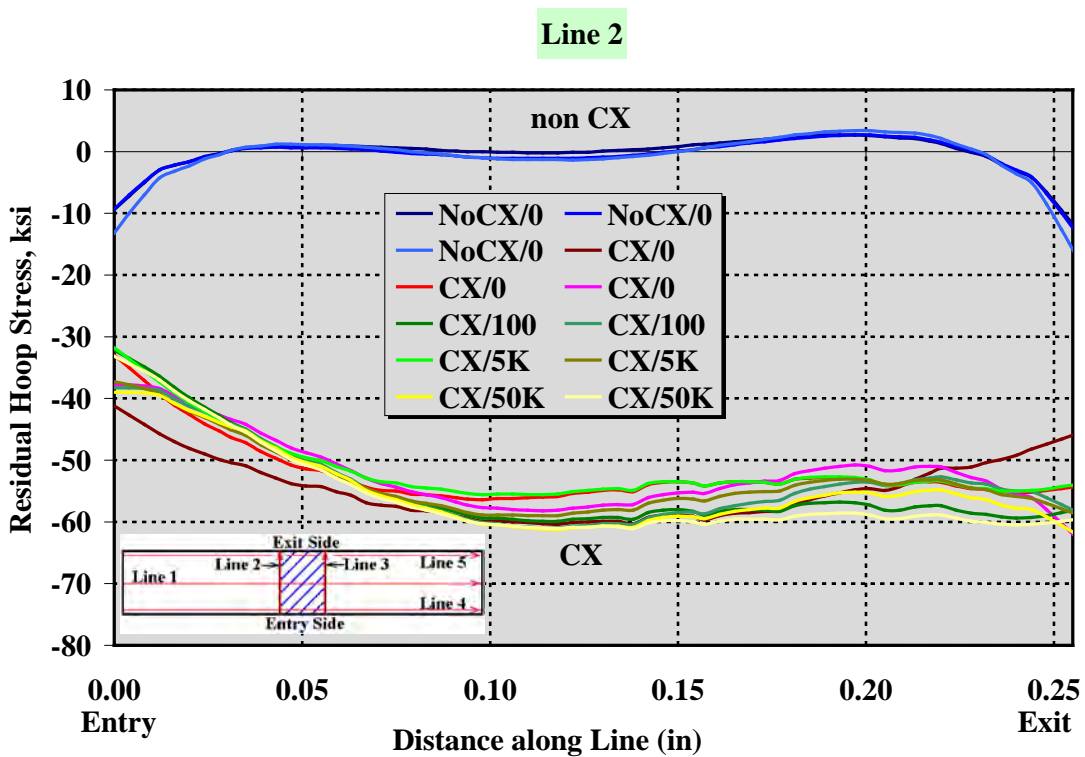


Figure 61. Left Side Bore Edge Residual Stress Measurements, Line 2. 2H21-3 are not cold worked or cyclically loaded, 2H24-6 are cold worked but not cyclically loaded, 2H27-8 are cold worked and loaded for 100 cycles, 2H29-30 are cold worked and loaded for 5,000 cycles, and 2H31-32 are cold worked and loaded for 50,000 cycles

Line 2 is the left side of the hole, running adjacent to the bore edge of the hole in Figure 59, from the mandrel “entry” side to the mandrel “exit” side; corresponding residual stress measurements are shown in Figure 61. The residual stress for the cold worked specimens is about -40 ksi near the entry side ($x = 0.0 \text{ in.}$), decreasing monotonically towards -60 ksi at the mid-plane ($x = 0.125 \text{ in.}$), and leveling off approximately -60 ksi toward the exit side. The residual stresses in the 3 non-CX coupons, 2H21, 2H22, and 2H23 are representative of the “as-machined” state of the coupon; certainly the residual stresses are of significant (compressive) magnitude at the surfaces ($x = 0.0 \text{ in.}$ and $x = 0.25 \text{ in.}$) at -10 ksi, and will likely affect growth of cracks at those surfaces.

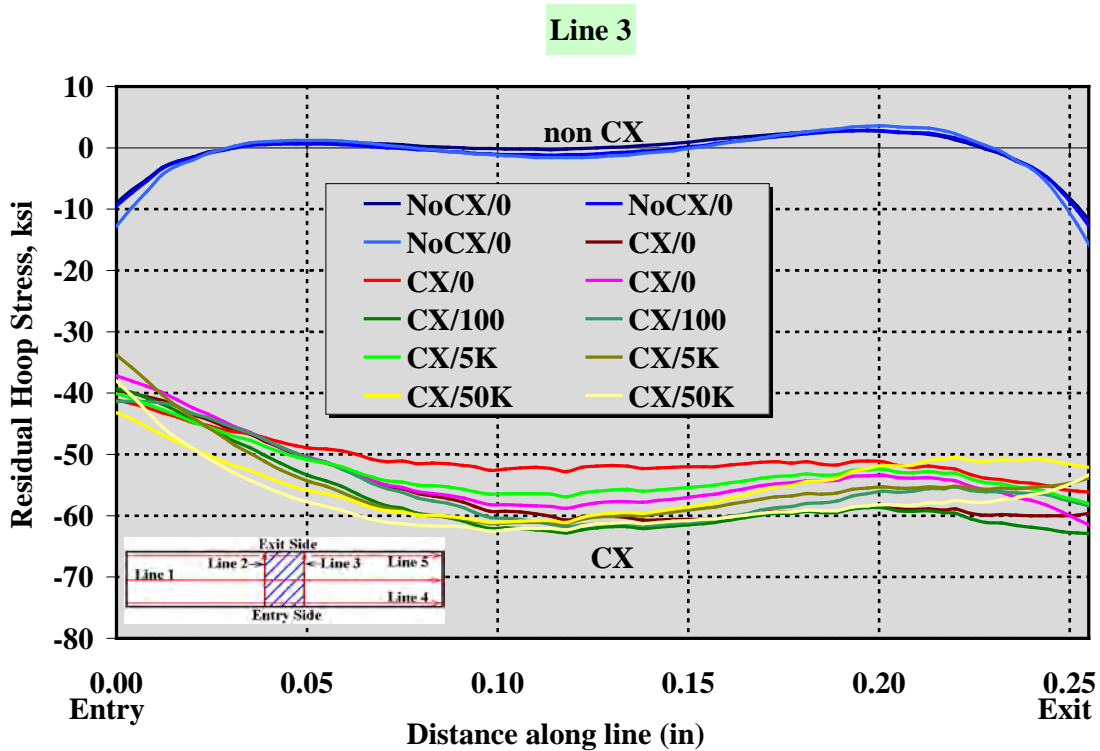


Figure 62. Right Side Bore Edge Residual Stress Measurements, Line 3. 2H21-3 are not cold worked or cyclically loaded, 2H24-6 are cold worked but not cyclically loaded, 2H27-8 are cold worked and loaded for 100 cycles, 2H29-30 are cold worked and loaded for 5,000 cycles, and 2H31-32 are cold worked and loaded for 50,000 cycles

Line 3 is the right side of the hole, running adjacent to the bore edge of the hole in Figure 59, from the mandrel “entry” side to the mandrel “exit” side; corresponding residual stress measurements are shown in Figure 62. The residual stress for the cold worked specimens is about -40 ksi near the entry side ($x = 0.0 \text{ in.}$), decreasing monotonically towards -60 ksi at the mid-plane ($x = 0.125 \text{ in.}$), and leveling off approximately -60 ksi toward the exit side. Again, the residual stresses in the 3 non-CX coupons, 2H21, 2H22, and 2H23 are representative of the “as-machined” state of the coupon; certainly the residual stresses are of significant (compressive) magnitude at the surfaces ($x = 0.0 \text{ in.}$ and $x = 0.25 \text{ in.}$) at -10 ksi, and will likely affect growth of cracks at those surfaces.

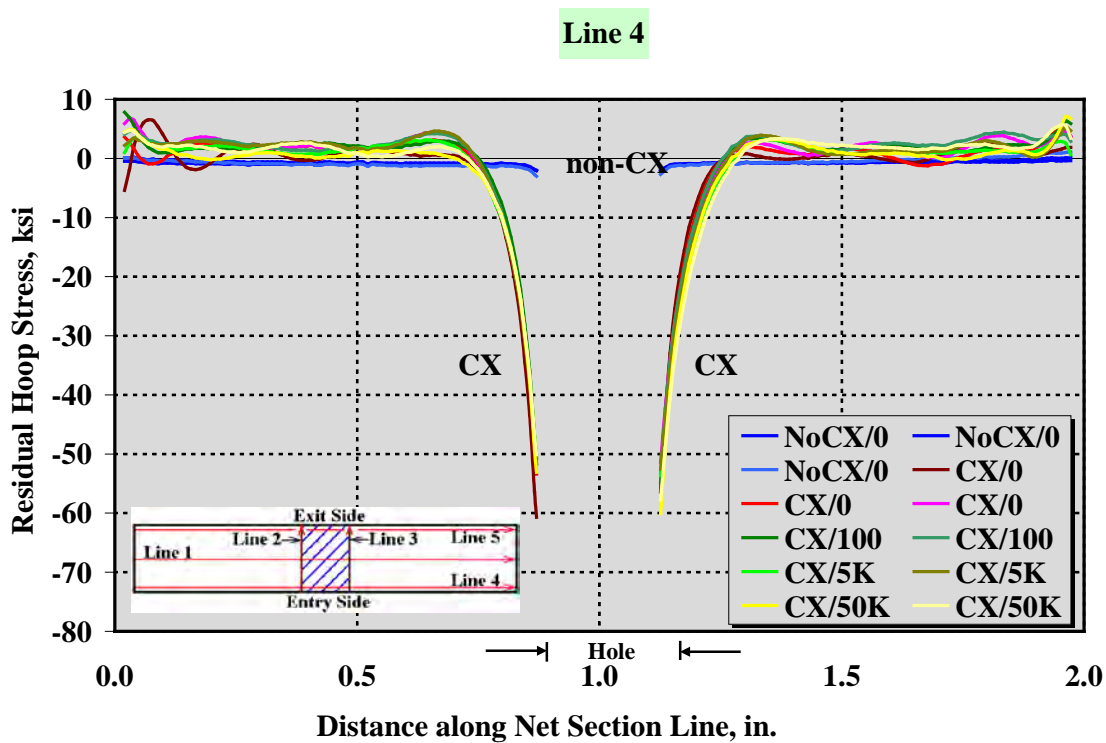


Figure 63. Residual Stress Measurements, Line 4, “Entry Side.” 2H21-3 are not cold worked or cyclically loaded, 2H24-6 are cold worked but not cyclically loaded, 2H27-8 are cold worked and loaded for 100 cycles, 2H29-30 are cold worked and loaded for 5,000 cycles, and 2H31-32 are cold worked and loaded for 50,000 cycles

Line 4 is along the “entry” side of the plate, from the left free edge to the right free edge in Figure 59, about 0.02 in. (0.5 mm) from the free surface at the entry side; corresponding residual stress measurements are shown in Figure 63.

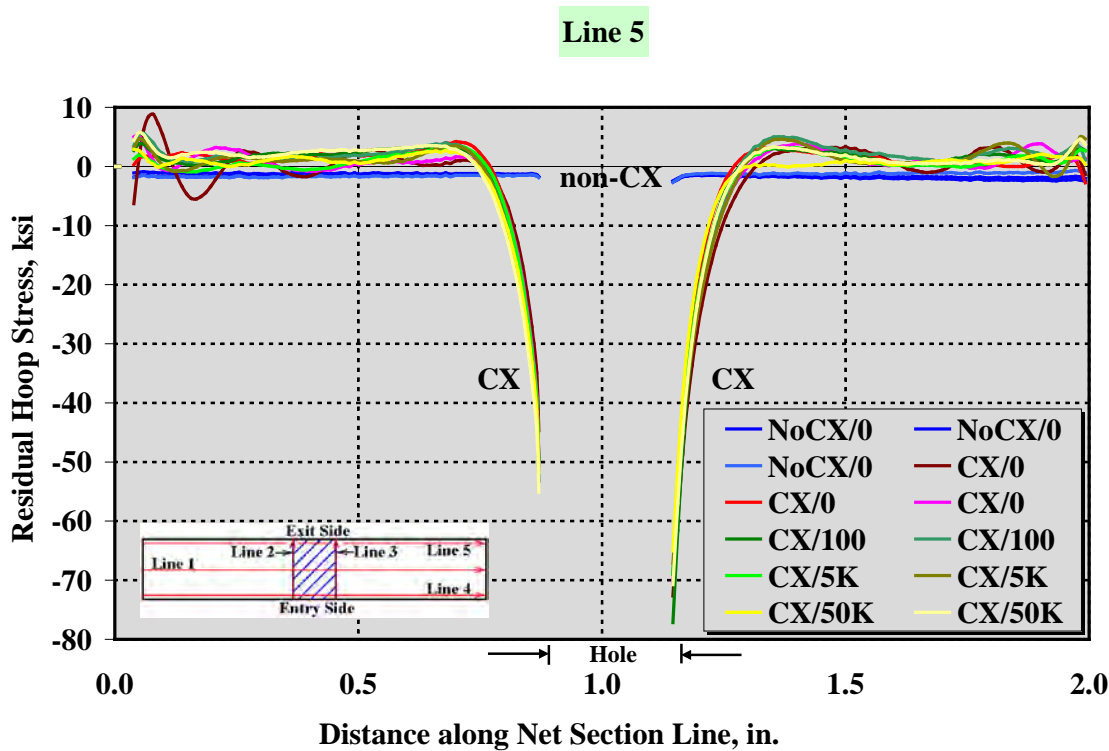


Figure 64. Residual Stress Measurements, Line 5, “Exit Side.” 2H21-3 are not cold worked or cyclically loaded, 2H24-6 are cold worked but not cyclically loaded, 2H27-8 are cold worked and loaded for 100 cycles, 2H29-30 are cold worked and loaded for 5,000 cycles, and 2H31-32 are cold worked and loaded for 50,000 cycles

Line 5 is along the “exit” side of the plate, from the left free edge to the right free edge in Figure 59, about 0.02 in. (0.5 mm) from the free surface; corresponding residual stress measurements are shown in Figure 64.

In each of Figure 60, Figure 61, Figure 62, Figure 63, and Figure 64, the residual stress in the non cold worked coupons are bluish lines, and small compared to the residual stress in the cold worked coupons, again as expected.

To illustrate the magnitude of the “background,” as-machined residual stress, the residual stress in the non cold worked coupons is plotted for both the left and right sides of the hole in Figure 65. Significant machining residual stress extends at least 0.05 in. into the coupons from each face, that is, for about 40% of the total depth when the effect of machining of sides is added. Note that typically the faces were not polished by the machine shop, but that some polishing of faces did occur to facilitate digital image correlation (DIC) measurements. At the surfaces, the CM measured about -10 ksi maximum compressive stress.

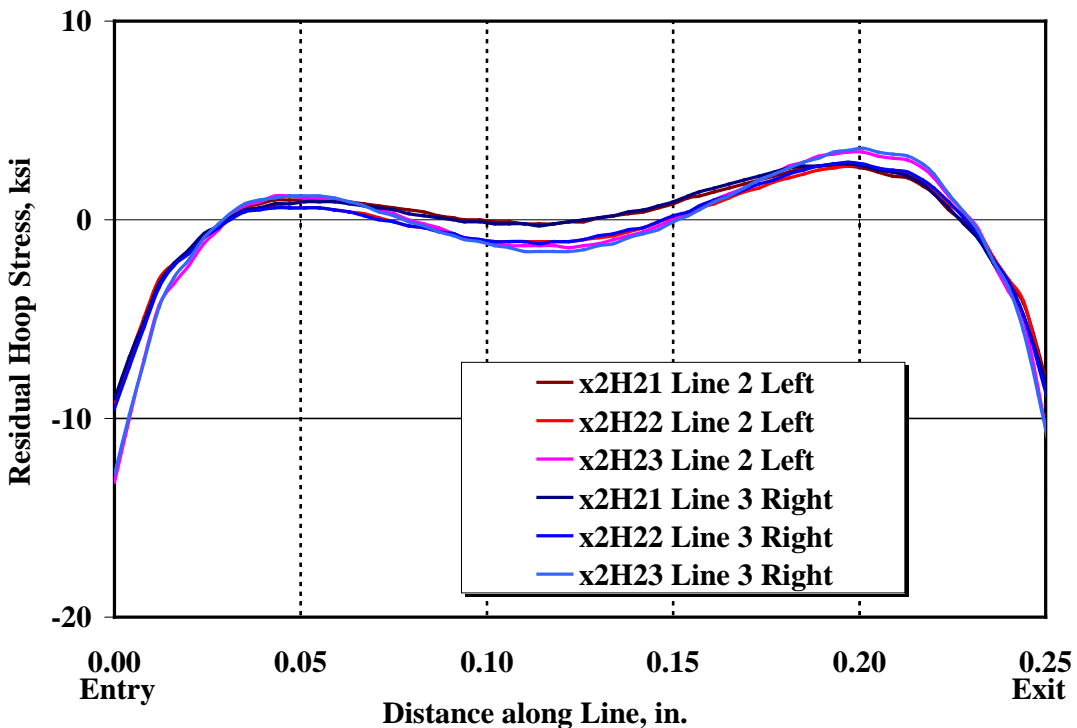


Figure 65. Both Bore Edge Residual Stress Measurements in Non Cold Worked Coupons Along Left (Line 2) and Right (Line 3) Hole Edges. 2H21-3 are not cold worked or cyclically loaded

To try to differentiate the effects of number of load cycles, the residual stress is averaged for similar loaded coupons, Figure 66. The line marked “CX 0-4% CX” is the average of the 3 cold worked coupons that were not loaded cyclically (2H24, 2H25 & 2H26); the line marked “CX 100-4% CX” is the average residual stress for the 2 cold worked coupons that were cyclically loaded with 25 ksi for 100 cycles (2H27 & 2H28); the line marked “CX 5000-4% CX” is the average residual stress for the 2 cold worked coupons that were cyclically loaded with 25 ksi for 5,000 cycles (2H29 & 2H30); and the line marked “CX 50000-4% CX” is the average residual stress for the 2 cold worked coupons that were cyclically loaded with 25 ksi for 50,000 cycles (2H31 & 2H32). It appears as if there might be an effect of load cycling, as in general the residual stress generally becomes more negative (compressive) with more load cycles on the entrance side ($x = 0.0 \text{ in.}$ in Figure 66), while becoming slightly more negative (compressive) on the exit side ($x = 0.25 \text{ in.}$ in Figure 66).

Figure 67 has a comparison of the average residual stress caused by 4% CX on the three major planes: exit, middle and entry. The entry plane (bottom face in Figure 59) has smaller residual stress at the hole edge (verifying the trend in the residual stress seen at $x = 0.0 \text{ in.}$ in Figure 67, though not the magnitudes of the residual stress on the respective planes—on the entry plane, the residual stress is about -40 ksi in Figure 67, while Figure 67 shows a residual stress of -55 ksi; similarly, on the exit plane, the residual stress is about -60 ksi in Figure 67, while Figure 67 shows a residual stress of -70 ksi), while both the middle and exit planes have similar magnitudes in residual stress.

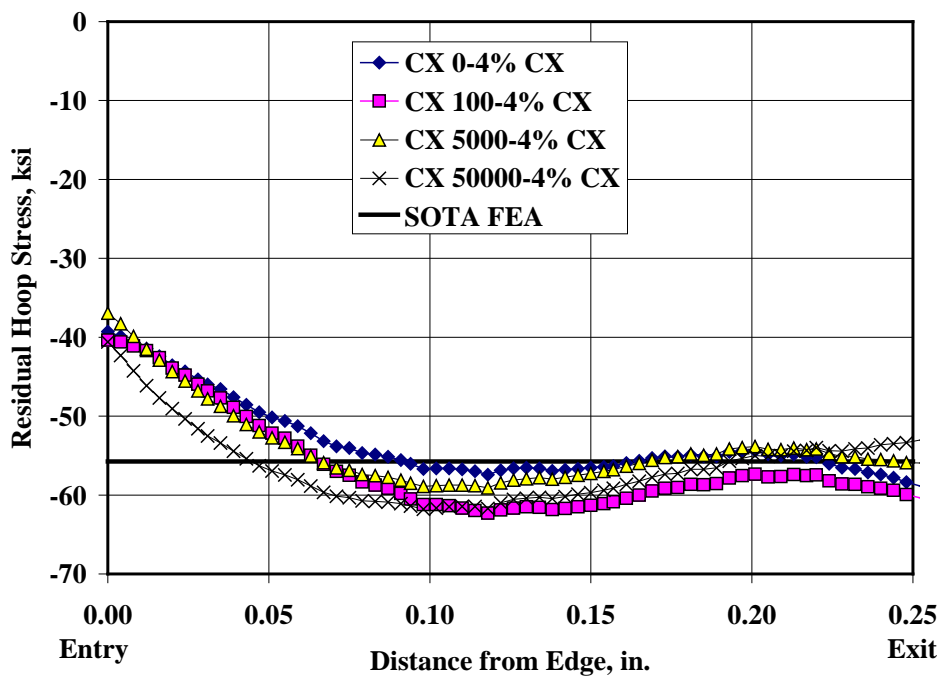


Figure 66. Averaged Relative Residual Stress Measurements as a Function of pre-Applied Load Cycles, Line 3. A StressCheck simulation, marked “SOTA FEA” of 4% CX is added for reference

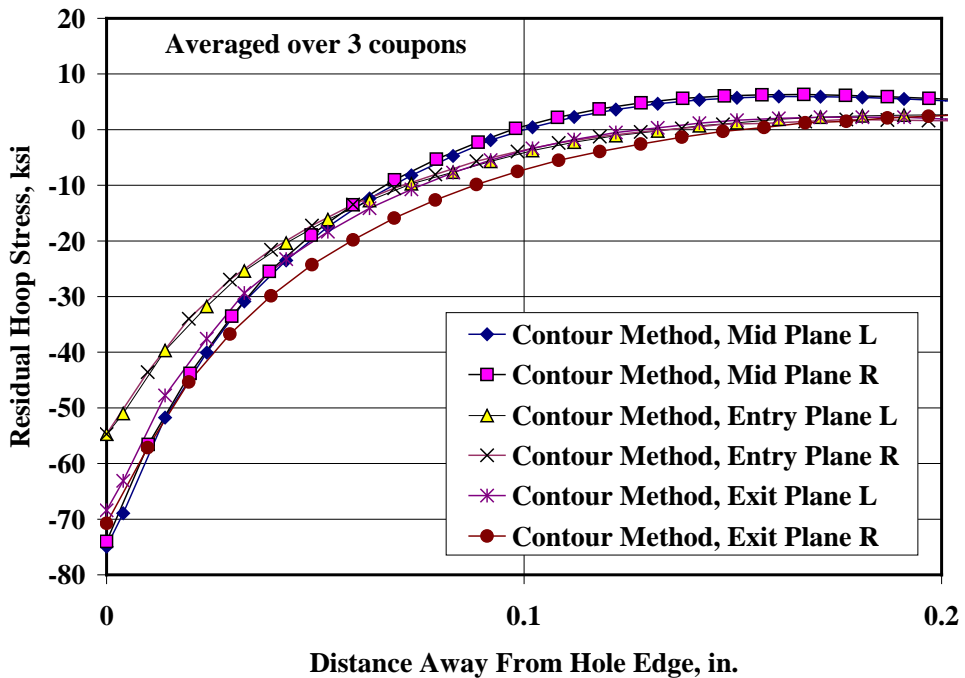


Figure 67. Averaged Residual Stress Measurements, 4% CX, No Load. Exit, Middle and Entry Planes

The effect of number of load cycles on the residual stress measurement is shown in Figure 68, which shows the average residual stress at each number of load cycles on the entry plane from the left edge of the hole bore. There appears to be little difference that can be attributed to load cycling. For reference, a StressCheck simulation of 4% CX is also shown in Figure 68—this simulation is difficult to reconcile with the CM measurements, as the qualitative behaviors of the two methods are only roughly equivalent; the FEA simulation starts lower at the hole edge, dips down (which you don't see at all in the CM measurements), then rapidly increases to the tensile region (similar to the CM measurements), peaks locally (about $x=0.15$ in.) and decreases down again to something close to zero ksi away from the hole, as the CM measurements also do.

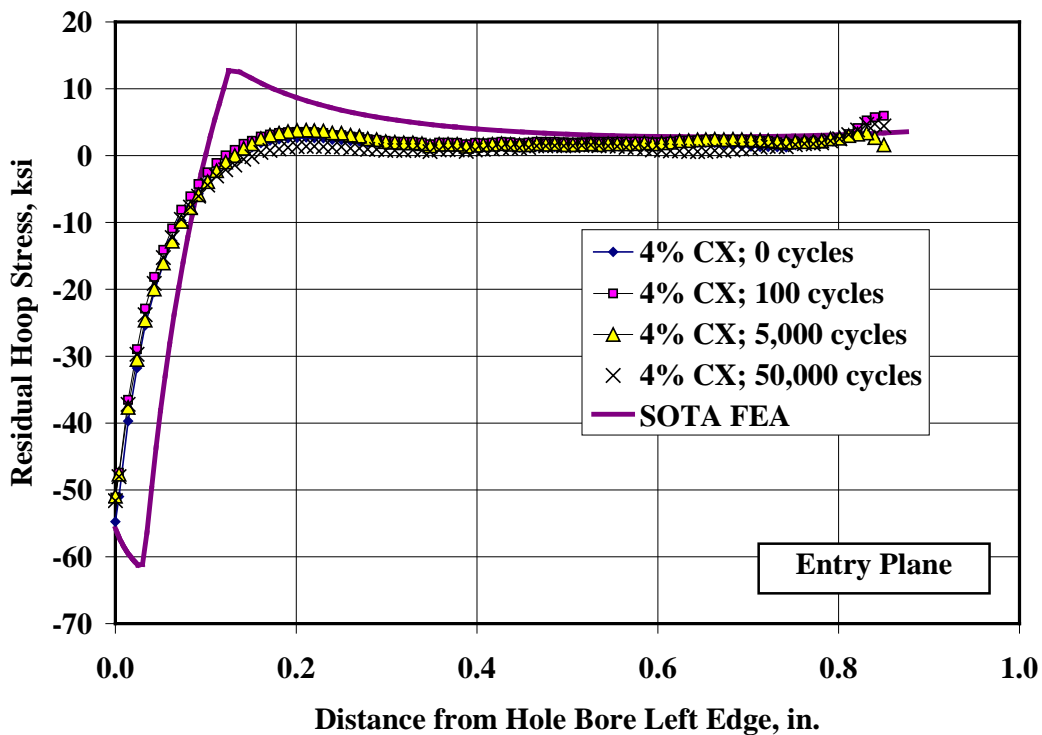


Figure 68. Residual Hoop Stress Measurements, 4% CX, Entry Plane, Variable Cycles

6.2.3 Comparison of Contour Method to X-ray Diffraction

Residual stress measurements made with the Contour Method (CM) are compared to residual stress measurements made by Nadri, et al, with X-ray diffraction (XRD), Ref. [15] in Figure 69 below. There are several factors that could explain the discrepancies between the two sets of measurements:

- 1) Though all coupons have nominally the same cold working level, 4%, measurements were made on slightly different hole sizes and section widths: the CM measurements were made on 0.25 in. diameter holes in 2 in. wide sections, and the XRD measurements were made on 0.338 in. diameter holes in 1.575 in. wide sections,
- 2) the two techniques are measuring two different regions—the CM measurements were made on the mid-plane, away from the faces (suggesting plane strain) and the XRD measurements were made on the two faces (suggesting plane stress)

- 3) both measurement techniques rely on accurate constitutive behavior descriptions, though in two entirely different ways: the CM measurements require a finite element simulation using the measured deformations of the measurement plane and make the assumption that the measurement plane has deformed elastically, and the XRD measurements require making assumptions about how the stress is related to the lattice spacing in the material, and
- 4) the XRD method uses a probe that averages stress measurements over a particular surface area, which depends on probe size (there is no way for us to know what that averaging area is, as the Nadri reference did not have that information). The CM measurements, however, are not averaged over a large area, so can be, at least in principle, more precise than XRD measurements.

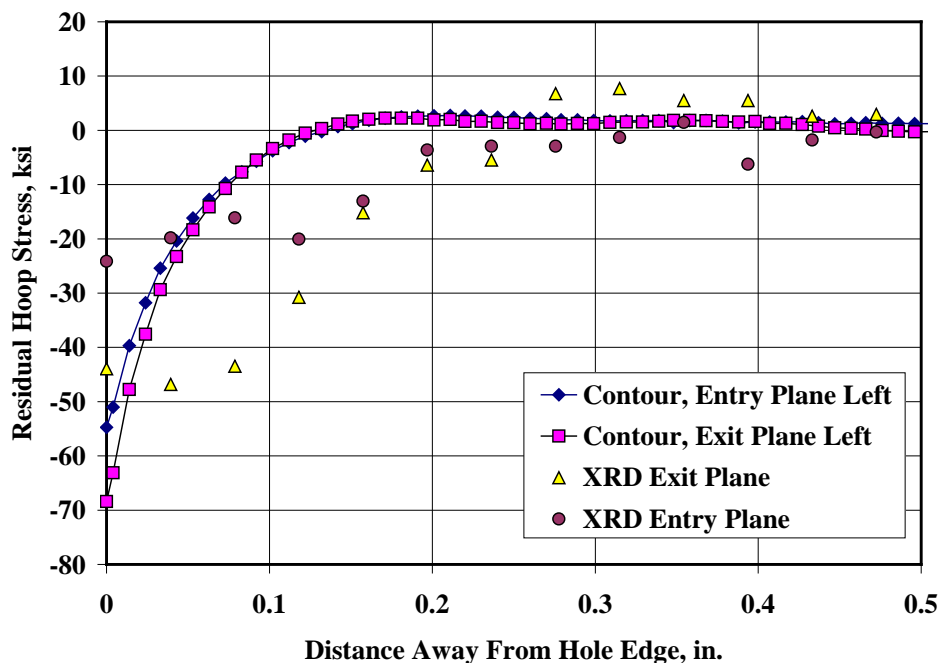


Figure 69. Comparison of Residual Stress Measurements with CM and XRD Methods, 0 Load Cycles

6.2.4 Cyclic Evolution of Residual Strains Measured by Digital Image Correlation

It is even more difficult to discern an effect of cyclic loading on the digital image correlation (DIC) strains, Figure 70, which shows the strains in coupon 2H32, measured at 1 cycle, 100 cycles, 5,000 cycles and 50,000 cycles for a 25 ksi load. The difference between the 50,000 cycle measurement and the 1 cycle measurement is less than 0.0005 in/in=500 μ in/in.

2H32

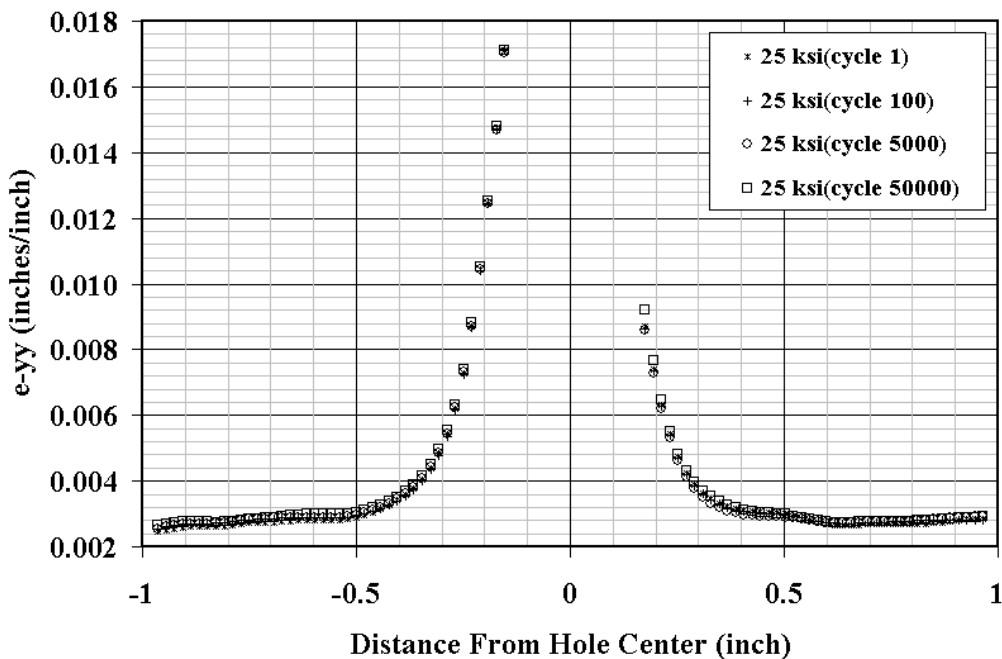


Figure 70. Residual Strain Measurements, 4% CX, Entry Face, Variable Cycles

6.2.5 Conclusions

There were several interesting aspects to the CM measurements. The behavior of the residual stress fields is consistent with the observations of the failure modes in the fracture faces; lower residual stresses, less negative (that is, smaller in magnitude but still compressive) were measured on the entrance face compared to the mid-plane and exit face—this is consistent with the failure mode typically observed in cold worked coupons, in which the “failure flaw” normally nucleates at the corner of the entrance plane and the hole bore. While this study was focused on determining the redistribution or relaxation of stresses, the observed changes have mixed trends and potentially could be masked by other variables that would influence specimen to specimen variation. The data show other interesting behavior, such as the wave shapes along the distributions, and it is difficult to ascertain if they are results of the CM process or indicative of non-linear behavior (Hill Engineering verified that the waves are related to the computational algorithm of the contour method). Though we observed no cracks on the coupons before they were sent to Hill Engineering for contour method measurement (which is a destructive technique), early formation of small cracks in cold worked holes could still have influenced the measured residual stress fields, thus complicating the extraction of the isolated effect of cycles on the residual stress fields. Other fatigue experiments completed during this program show that cracking, particularly in the bore of the hole, happens very quickly, usually within 32,000 cycles at the stresses tested here.

It is premature to make firm conclusions about this data. The CM measurements appear to provide useful information, although unsupported by the XRD and other measurement

techniques. One of our challenges is to determine which method *if either* is right for analytical modeling. We would have recommendations for looking at further CM measurements, but further engineering is needed prior to selecting the conditions of the experiments. It is important to keep in mind that this series of experiments briefly investigated the evolution of residual stress due only to the application of a number of tension load cycles at room temperature and not relaxation due to other effects, such as, thermal load cycling and time.

6.3 DIC Data from Task 8 and Observations on Residual Stress Relaxation

6.3.1 Initial Observations

Changes in the average strain profile across the net section of the mandrel entrance face were observed during digital image correlation (IC or DIC) experiments (Figure 3, May 2010 GDIT MSR). During 25 ksi (net section maximum stress, when ignoring the presence of the hole) fatigue cycling at a stress ratio $R=0.0$, the test was repeatedly paused to acquire IC images during a 25 ksi dwell. The change in strain, relative to the first 25 ksi dwell, was then plotted as a function of cycles in order to see how the strains changed during the test. Observations made when analyzing the results of the 2H05 test led to the postulate that changes in the IC strain profiles are due simply to crack formation and propagation during the test, and *not* due to relaxation of residual stresses. Since the time of the May 2010 MSR, specimen 2H06 fatigue cycling with IC was conducted at the same stress level as 2H05, the only difference being that 2H06 was *not* cold worked, and IC measurements were taken at more frequent intervals due to the shorter total life of the non-cold worked specimen. Comparisons between specimen 2H05 and 2H06, when plotting strain changes vs. life fraction, Figure 71, appear to indicate that strain changes are occurring more rapidly in the cold worked specimen than in the non-cold worked specimen. However, this result still does not verify if the strain changes are fully due to cracking, since the crack size vs. cycles curve is typically significantly different for cold worked vs. non-cold worked specimens.

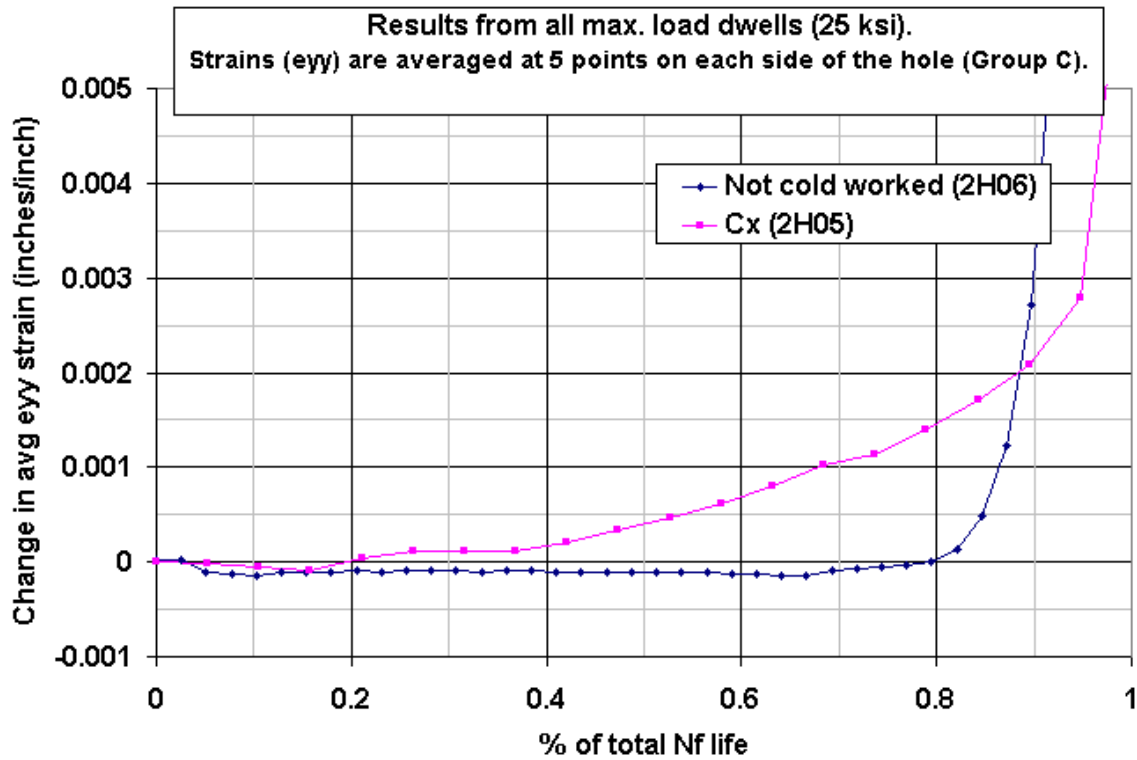


Figure 71. Comparison of Surface Strain Changes near the Hole for 2H06 and 2H05

The IC speckle paint pattern prevents optical inspection of crack lengths during testing, as the paint bridges and obscures the crack tip. However, other similar specimens were tested under an identical stress level, stress ratio, and cold work condition. These specimens did not use speckle paint or IC, instead they were inspected optically to measure crack growth. They also used EDM notches as crack starters, whereas 2H05 and 2H06 did not. One specimen was selected (2H20, No Cx, $N_f = 22,847$ cycles) as similar to 2H06 ($N_f = 39,020$, no Cx), and one specimen was selected (2H14, Cx, $N_f = 180,066$ cycles) as similar to 2H05 (Cx, $N_f = 195,695$). A remaining life (cycles) vs. optical surface crack length plot was generated for both 2H20 and 2H14 (Figure 2). These two plots were used to generate the ‘expected surface crack length’ for specimens 2H06 and 2H14, respectively. The expected crack length was determined by computing the remaining life (in cycles) for each data point in Figure 71, then interpolating an expected crack length using the respective curve for the ‘similar’ specimen in Figure 72; using a remaining life plot helps to mask the effects (on total N_f life) of the EDM starter notch in specimens 2H20 and 2H14.

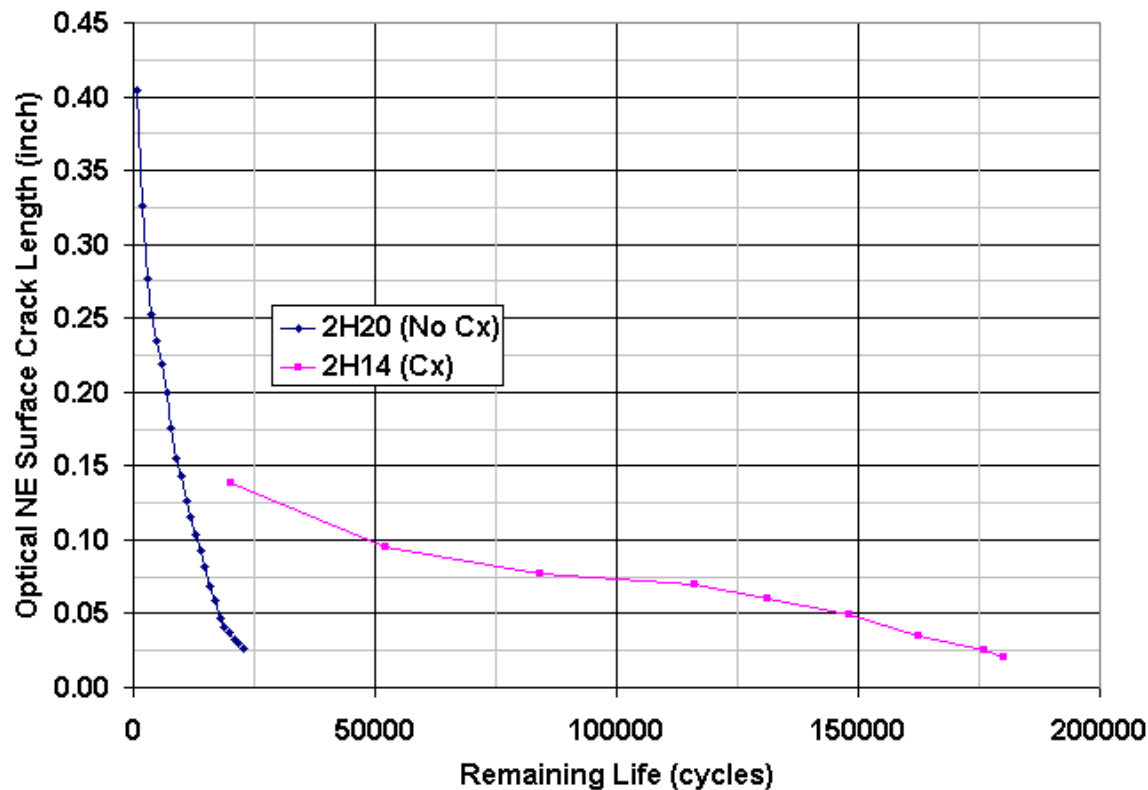


Figure 72. Remaining Life Plot for Specimens ‘Similar’ to 2H06 and 2H05

Finally, the IC strain changes in time were plotted against the ‘expected surface crack length’ for specimens 2H06 and 2H05, Figure 73; this plot suggested that there may be something happening with mandrel entrance surface strains in a cold worked specimen that is not fully explained by the physical surface crack size alone. In multiple cold worked specimens, multiple site cracking has been observed down the bore near the very beginning of the experiments, even those with an EDM starter notch. This bore cracking could be contributing to the relatively rapid strain changes seen on specimen 2H05, as non-cold worked specimens do not typically exhibit this rapid multi-site bore cracking at the onset of cycling. Further experiments were conducted in order to provide a better link between IC images and surface crack lengths.

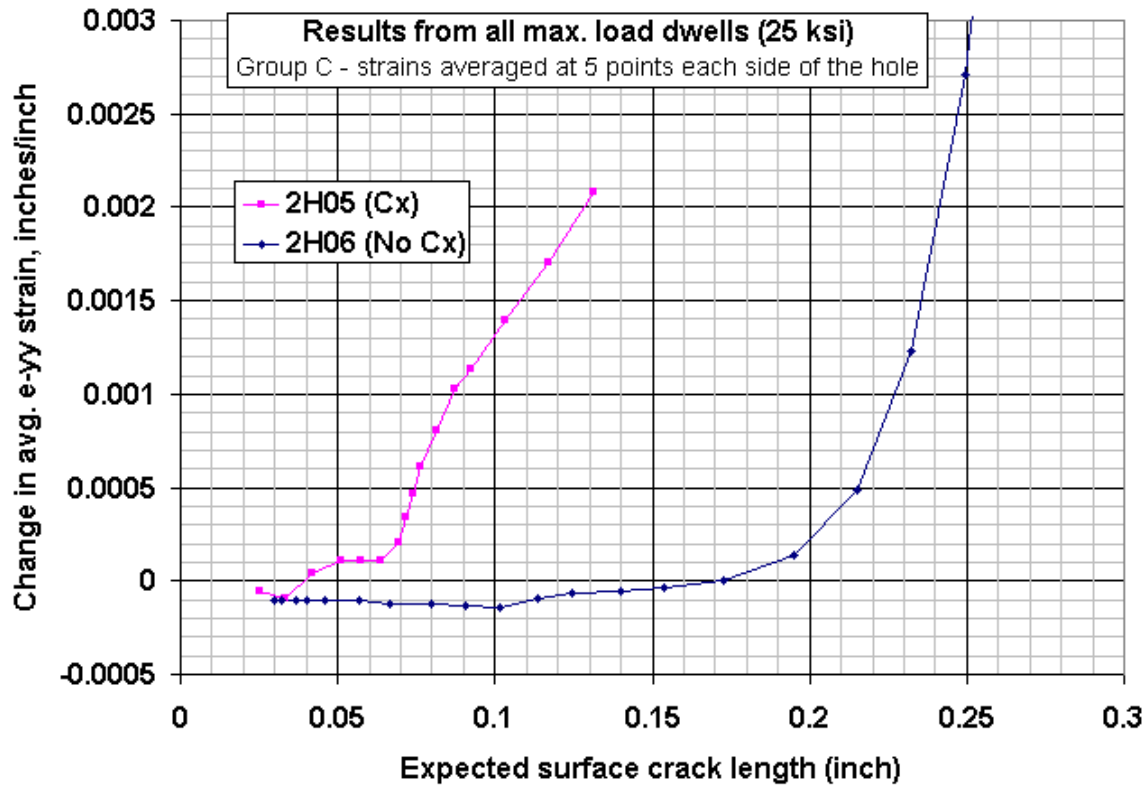


Figure 73. IC Strain Changes vs. Expected Surface Crack Length

Figure 73 above suggests that there may be a relaxation and/or redistribution effect that is present in cold worked specimens and not present in non-cold worked specimens. However, this figure was based on *assumptions* of physical crack lengths instead of actual physical crack lengths, since the IC speckle paint prevents optical inspection of the surface crack length.

6.3.2 Experiments and Refined Observations

In order to investigate *actual* crack lengths vs. changes in IC ϵ_{yy} strain, a self-marking spectrum was used with two coupons, 2H35 and 2H36. The marker bands were used post-fracture to determine surface crack length vs. cycles, and IC measurements were obtained vs. cycles during the physical testing. The marking spectrum and cycles to failure N_f are shown in Table 32, Table 33, and Figure 74. Specimen 2H35 was non-cold worked and 2H36 was cold worked.

Table 30. Marker band spectrum MB-DIC.

Description	Peak	Valley	Number of Cycles
Nominal Stress	0.80	0.00	4000
Marking Overload	1.00	0.00	10
Marking Underload	0.53	-0.27	490

Table 31. Specimen Details.

Specimen	Cold Worked?	Nominal Stress (ksi)	Max. Stress (ksi)	N_f
2H35	No	18	22.50	181,845
2H36	Yes	23	28.75	765,380

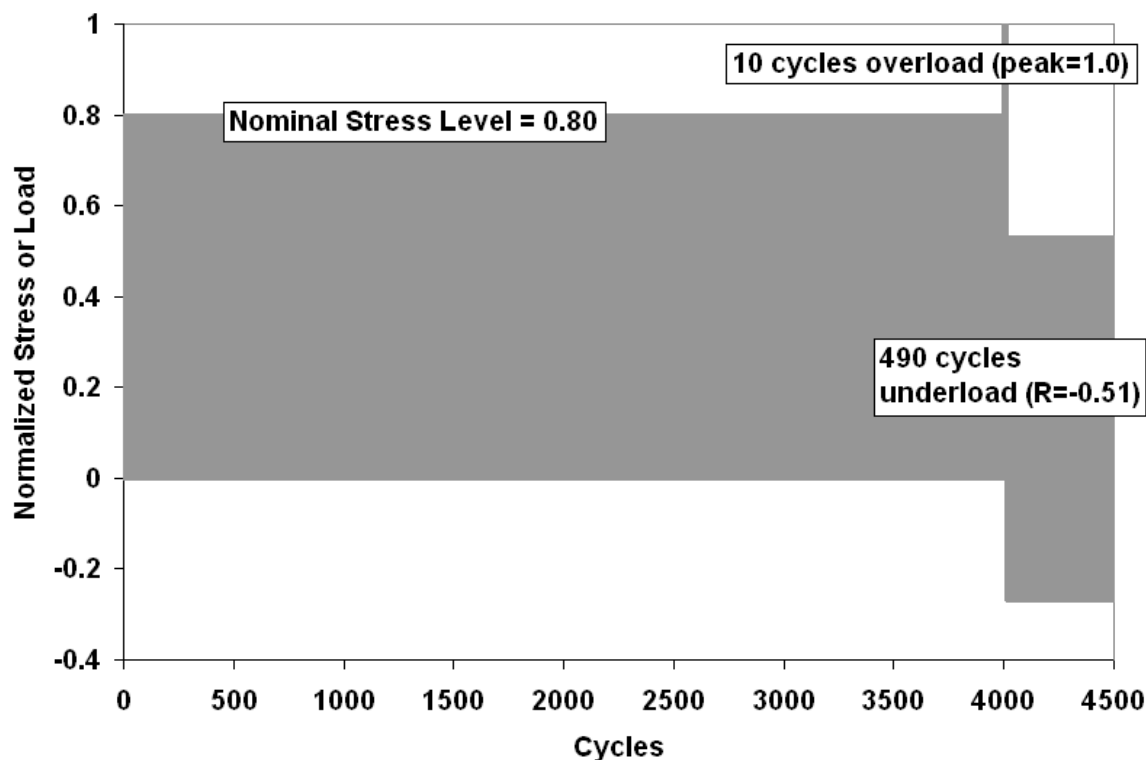


Figure 74. Normalized spectrum MB-DIC for specimens 2H35 and 2H36

The ε_{yy} strain extraction line is shown in Figure 75. Results are extracted at 101 points along this line, and consistent with previous measurements obtained using IC, the ε_{yy} strain was averaged over a short region directly adjacent to the central hole. Termed “Group C” in the May 2010 MSR, this region uses the average strain of 10 points directly adjacent to the hole (5 points each side) along the extraction line. For the total 2” wide specimen width, this is a strain average over approximately a 0.16” long region (0.08” on each side of the hole). Consistent with previous measurements, the IC images are captured during a load dwell at the first maximum stress level in the spectrum (the 1.0 marking overload). For the marking spectrum MB-DIC of Figure 74, this resulted in the first (reference) image being acquired during the 4001st cycle, then subsequent images acquired every additional 4500 cycles until specimen failure. The change in ε_{yy} strain at the subsequent maximum stress levels is then reported relative to the first reference image that was taken at maximum stress.

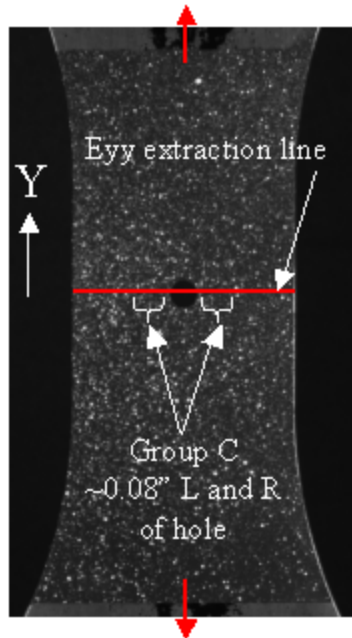


Figure 75. Strain Extraction Line, Definition of “Group C”, and Loading Direction (Y)

The relatively low nominal stress levels allowed specimens 2H35 and 2H36 to mark clearly, and the resulting fractography on both specimens showed well-behaved crack growth a vs. N curves, Figure 76.

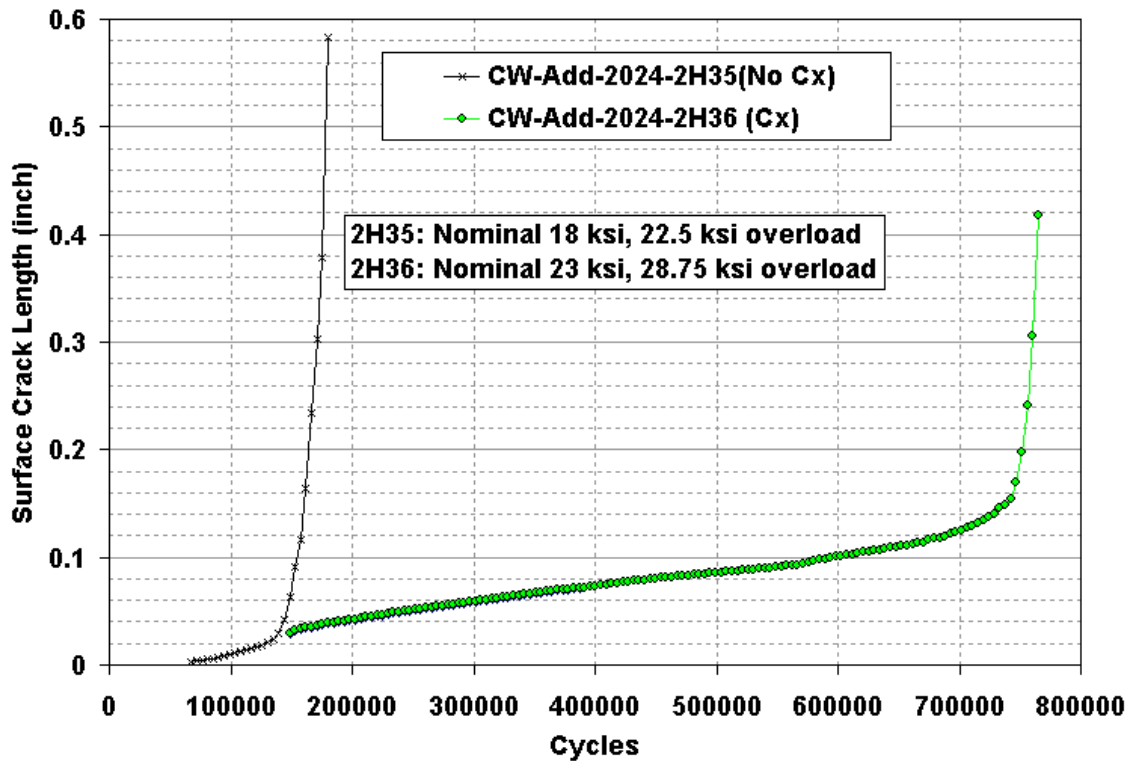


Figure 76. Marker Band Crack Growth Plots for 2H35 and 2H36

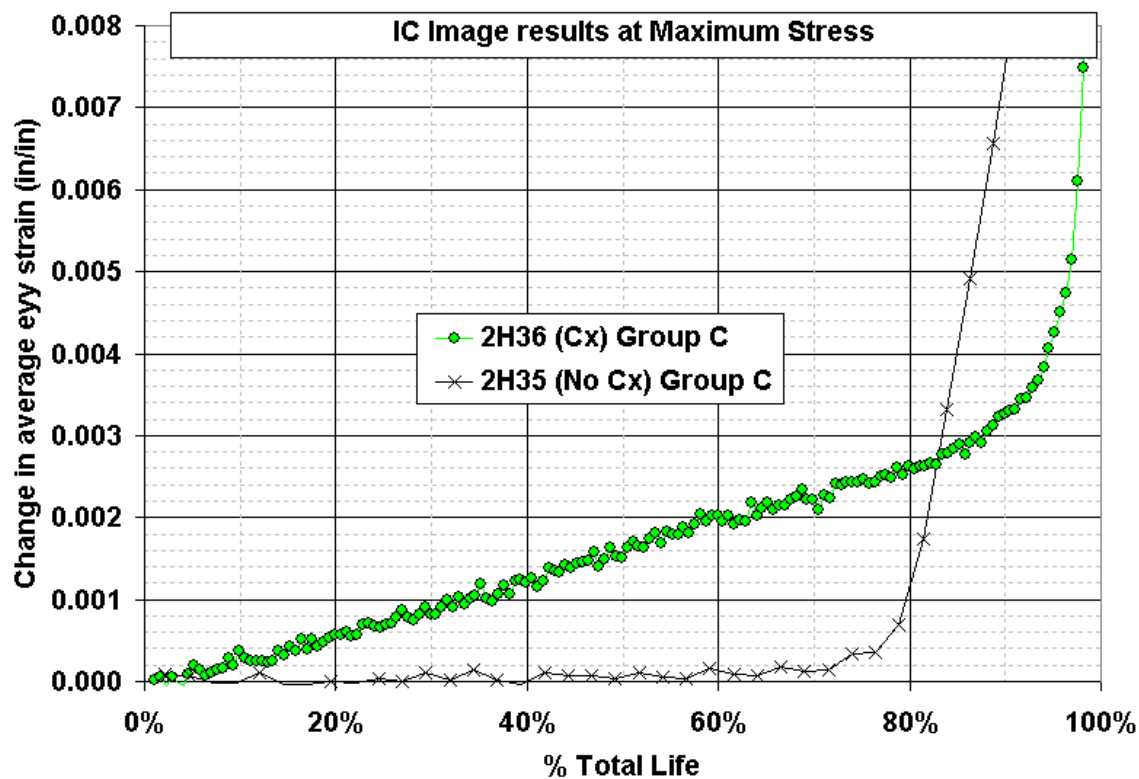


Figure 77. IC Strain Changes vs. Total Life for 2H35 and 2H36.

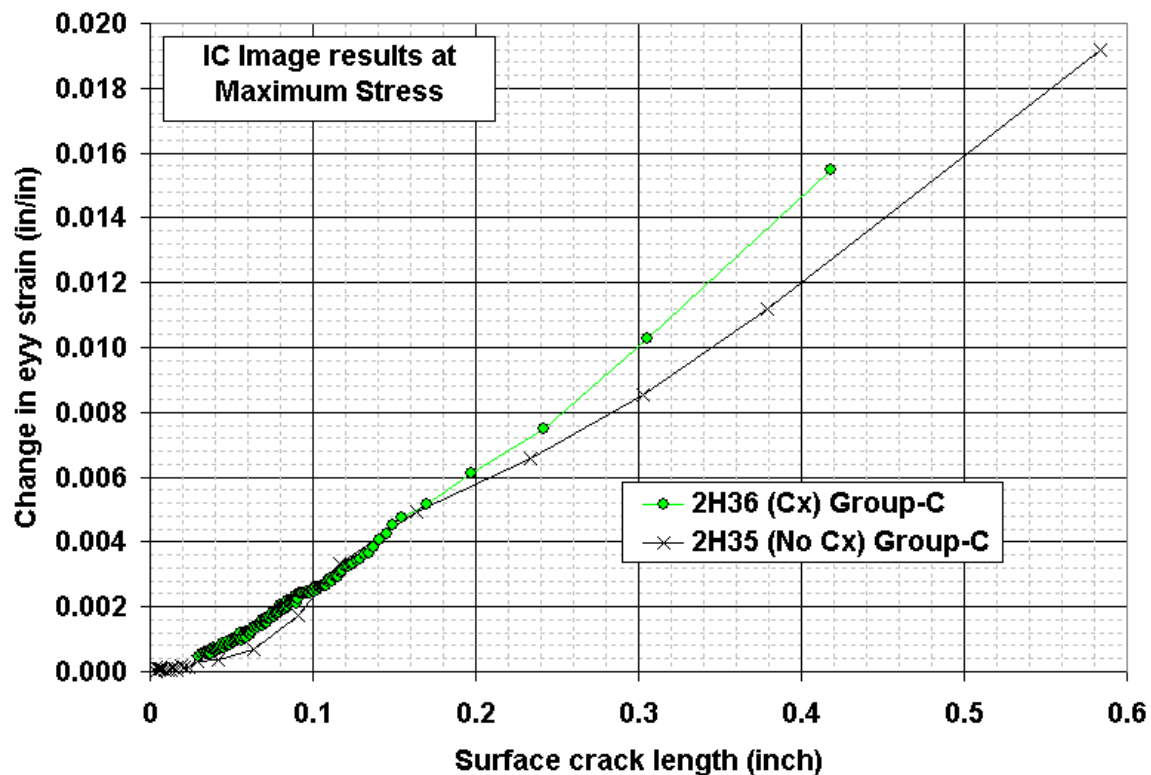


Figure 78. IC Strain Changes vs. Marker Band Surface Crack Length for 2H35 and 2H36

Figure 77 shows the changes in ϵ_{yy} strain vs. life fraction for the two specimens 2H35 and 2H36. These results appear fairly consistent with Figure 71, except the cold worked specimen 2H36 from Figure 77 appears to have a more linear change in the ϵ_{yy} strain response than does the cold worked specimen 2H05 from Figure 71. We speculate that this difference in curve shapes is likely due to the marking spectrum of 2H36, as the spectrum for 2H05 was non-marking, 25 ksi constant amplitude.

When the ϵ_{yy} strain changes were plotted against the actual surface crack length determined via fractography, Figure 78, it is important to note that there is very little, if any, difference between the cold worked coupon and the non cold worked coupon. This is in sharp contrast to the results of Figure 73, but the Figure 73 results were based on crack lengths *expected* from tests of similar specimens, and not actual crack lengths such as those used in Figure 78. The Figure 78 results lead us to the preliminary conclusion that IC surface strain changes observed during testing are likely solely related to surface crack length changes (strain redistribution), and not related to relaxation of cold working strains.

Further testing and fractography were conducted during Task 8 of this program, one of the multiple purposes of this testing was to help support or refute the above conclusion. Full details of the test conditions, predictions, and results from Task 8 are contained in Section 7.3 of this report. Of the 18 central hole, dogbone 2024-T351 specimens tested under Task 8, five were selected (Table 34) for fractography of the marking bands in order to make comparisons to the results shown in Figure 78. These five specimens used the marking spectrum from Figure 74, and in the case of specimen 2H46, the marking spectrum also included a single 37 ksi overload before the start of the test.

Table 32. Task 8 Specimens Selected for IC Correlation vs. Marker Band Crack Length

Specimen	Cold Worked?	Nominal Spectrum Stress (ksi)	Max. Spectrum Stress (ksi)	1 st cycle overload (37 ksi)?	N_f
2H37	Y	25	31.25	N	377,691
2H42	N	25	31.25	N	48,843
2H46	N	25	31.25	Y	80,549
2H55	Y	29	36.25	N	98,448
2H43	N	29	36.25	N	36,677

Due to the high stress levels present in these specimens, the three non-cold worked specimens did not mark well, and only one or two marker bands could be correlated with IC surface crack lengths. The two cold worked specimens marked better, though not as well as they did at the lower stress levels used for specimens 2H35 and 2H36. Hence, the cold worked specimens have more measurable surface crack lengths during the life of the specimens. These additional surface crack lengths in the cold worked specimens are also due to a crack nucleation mode shift: the cold worked specimens, after a short period of numerous secondary crack nucleations along the hole bore, tended to exhibit the primary crack nucleating as a corner crack on the mandrel entrance surface (the IC painted surface). The non cold-worked specimens tended to exhibit the primary crack nucleating near the center of the hole bore, and as such, any crack on the IC surface was not present until much later during crack propagation.

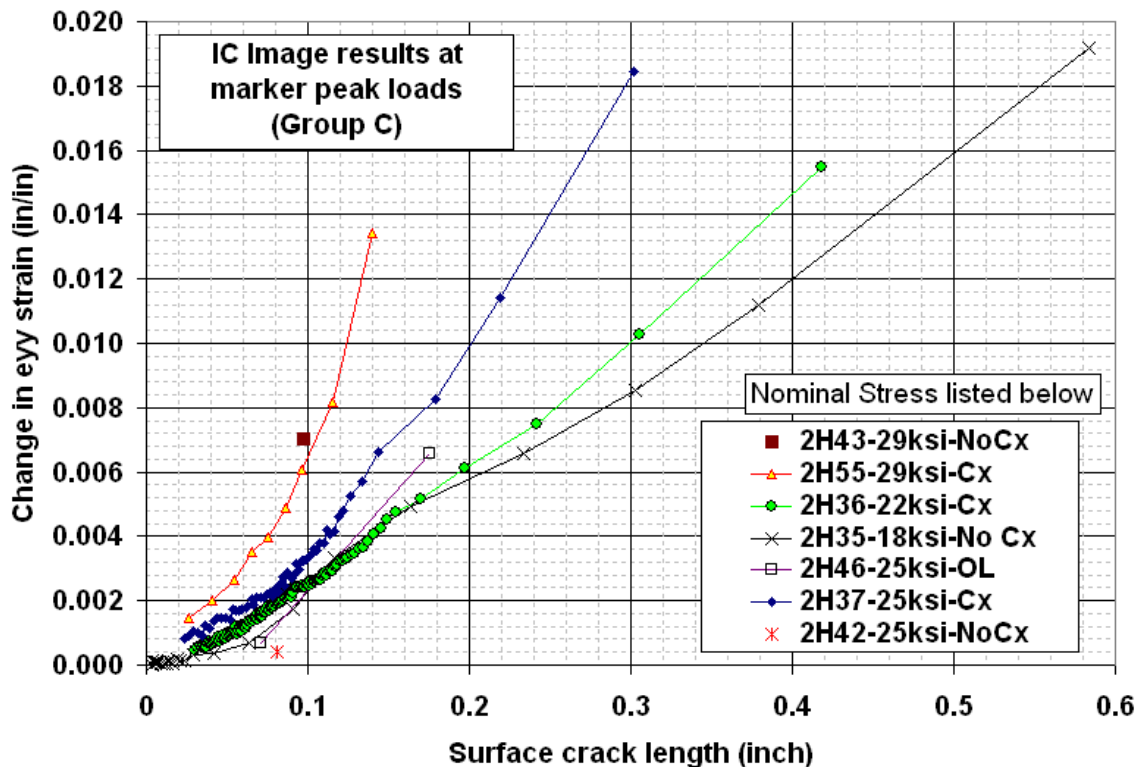


Figure 79. IC Strain Changes vs. Marker Band Surface Crack Length for Multiple Experiments

Figure 79 shows the fractography surface crack length results of the five specimens from Table plotted against the ϵ_{yy} strain changes observed using IC during the fatigue tests. These results are superimposed upon Figure 78 results for comparison purposes.

Although the results are not as conclusive as Figure 78, Figure 79 shows that there is still little evidence to suggest that surface relaxation of cold working strains is occurring. There is a fairly large difference between the single surface marker band point of the non-Cx specimen 2H42 and the Cx specimen 2H37, but since only one point was available from specimen 2H42, this may be an anomaly. 2H37 shows larger strain changes when compared with 2H36, but this effect is predominant only after crack lengths of 0.08" or so. Since "Group C" only includes points approximately 0.08" on both sides of the hole, it is supposed that the difference here is just due to macroscopic CTOD differences between the two specimens during the later stages of life – perhaps 2H37 was beginning to crack on the non-primary side of the hole and 2H36 was not. Finally, 2H43 and 2H55 show that the strain changes at equivalent surface crack lengths are more rapid for the higher nominal stress level of 29 ksi than they are at lower nominal stress levels. This was unexpected, as 2H35 and 2H36 demonstrated a stress level independence, but the fact remains that at 29 ksi nominal stress, there is a negligible difference in the surface strain change behavior of a cold worked specimen (2H55) vs. a non-cold worked specimen (2H43). In general, the conclusion based on Figure 78 is likely sufficient: the mandrel entrance surface strain field changes during fatigue testing, as observed by 2D digital image correlation, appear to be primarily related to surface crack lengths and not related to any time-based changes (strain relaxation) of the initial strain field that is imparted by cold working.

6.3.3 Relaxation and Redistribution Parameters

One of the deliverables for this project was to rerun previous analyses using newly incorporated relaxation or redistribution parameters. We have concluded that based on contour method measurements and DIC method measurements, we do not observe strain relaxation at the stress levels, cold working levels, and spectra tested under this program. We have also concluded that the redistribution of strain fields during a specimen's laboratory cyclic fatigue lifetime can be related to surface crack length, and therefore should be able to be modeled adequately by industry standard software such as AFGROW, since the software libraries of stress intensity solutions include the effect of cracked area relative to specimen geometry. Hence, analysis parameters for relaxation and redistribution were not developed under this program and there was no attempt to incorporate these parameters into any analyses.

7 Overload Model

7.1 FEA Modeling to Determine the Equivalent Overload (Task 3)

The initial overload (called the “Equivalent Overload) necessary to create an “Equivalent Residual Stress” (ERS) field for a cold worked hole of AA2024-T3511 was determined using two dimensional (2D) finite element analysis (FEA). The overload was judged “equivalent” if the residual stress field of the overload yielded a predicted life close to the predicted life of the 4% cold worked hole simulation.

The residual stress fields caused by tension overloads and cold working were computed with the finite element method. Simulations of several tension overload levels and nominally 4% cold working were made on symmetric, tapered section (dogbone) coupons of varying gage width: 1.5 in. and 2.0 in. Residual stresses from the edge of the centered hole to closest free edge are presented.

7.1.1 Model

7.1.1.1 Finite Element Mesh

The finite element mesh captured a tapered section (dogbone) with a hole centered in the middle of the narrow section, Figure 80. Because the geometry and loads were symmetric, it was necessary to model only half the entire coupon and apply symmetry constraints.

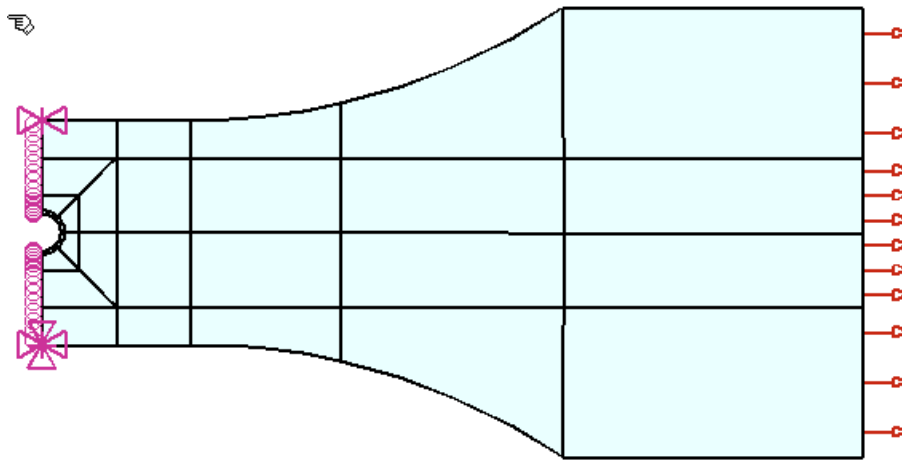


Figure 80. Finite Element Mesh. Overload Model

Gage section (minimum section in front of the hole) was either 2.0 or 1.5 inches wide; the hole diameter was 0.25 in., and the grip section was 3.0 in. wide. Overall coupon length was 7.0 in.

7.1.1.2 Material

The coupon material was a power law nonlinear plastic, with Ramberg-Osgood parameters $(E, S_{70E}, n) = (10,775 \text{ ksi}, 57.8 \text{ ksi}, 50)$ --these are typical material parameters captured in the monotonic stress strain tests of 2024-T351 aluminum alloy in this project.

7.1.1.3 Boundary Conditions

Geometries and loads were symmetric; to enforce symmetry, a symmetry boundary with rigid body nodes were applied to the coupon section that passed right through the middle of the hole, Figure 80. It was possible of course for this simple case, to further reduce the model to 1/4th the actual domain, but this half model was kept to allow flexibility, in case the hole is offset rather than centered.

7.1.1.4 Loads

7.1.1.4.1 Cold working

Nominal 4% cold working was simulated with a steel fastener in the centered hole. The cold working simulation starts with an interference fit (4% of the diameter) fit fastener then finishes when the fastener is removed from the hole. Reaming, which is a normal part of the FTI cold working process, was not simulated.

7.1.1.4.2 Overloads

Loads were constant normal (tension) traction at the larger grip section, depicted at right hand side of Figure 80. Tension loads of 40 ksi, 45 ksi, 50 ksi and 55 ksi (52.5 ksi for the 1.5 inch wide coupons) were applied, then released. The stress concentration at the holes is at least 3; therefore, the stresses at the hole edge with these tension loads are above yield stress, which is about 57 ksi. The goal is to specify a particular overload that appears to result in a residual stress that approximates the residual stresses caused by 4% cold working.

7.1.2 Results and Discussion

7.1.2.1 Wide Gage Section

The ‘wide’ gage section is 2.0 inches—this gage section width is the width the coupons were originally machined with and represents the reference coupon geometry. Simulations of 4% cold working and overloads of 40 ksi, 45 ksi, 50 ksi, and 55 ksi were made with the *p*-version finite element software StressCheck. in the wide gage section coupons. The tangential residual stress σ_t is normalized by the Ramberg-Osgood curve fit parameter S_{70E} and plotted against distance from the hole edge to the short side free edge, normalized by the hole radius, Figure 81. Note that the overload values of 40, 45, 50, and 55 ksi are 69%, 78%, 87%, and 95% of S_{70E} . The residual stresses caused by the two types of loads have similar behavior: 1) at the hole edge, the stress is negative (compression) and near yield, 2) as you move away from the hole edge, the stresses dip down a bit on an approximately linear line, become more negative, then bottom out, 3) from the minimum, the stress then rapidly increases until, 4) it crosses the 0 value, goes up a bit, is now tensile, then heads back down to zero. Because the stress is in compression near the hole, there must be a tensile region away from the hole for equilibrium. These simulations do not give clear indication of which overload is closest to the 4% CX—one possible screening method is to compare the fatigue lives predicted using the 5 residual stress fields and matching those fatigue lives and the crack paths.

7.1.2.2 Narrow Gage Section

The ‘narrow’ gage section is 1.5 inches—this gage section is a reduced section that would allow AP/ES to increase the overload; at 2.0 inches, the maximum overload stress would be 40 ksi, since the MTS fatigue machine is limited to 20 kips with calibration. At 1.5 inches, the maximum overload stress would increase to 53.33 ksi. Note that at this overload, StressCheck predicts that the coupon will yield all the way across the minimum section—therefore, the greatest overload, 52.5 ksi, is the largest overload possible with this narrow gage section.

Simulations of 4% cold working and overloads of 40 ksi, 45 ksi, 50 ksi, and 52.5 ksi were made with the p -version finite element software StressCheck. in the narrow gage section coupons. The tangential residual stress σ_{tt} is normalized by the Ramberg-Osgood curve fit parameter S_{70E} and plotted against distance from the hole edge to the short side free edge, normalized by the hole radius, Figure 82. Note that the overload values of 40, 45, 50, and 55 ksi are 69%, 78%, 87%, and 91% of S_{70E} . The residual stresses caused by the two types of loads have similar behavior: 1) at the hole edge, the stress is negative (compression) and near yield, 2) as you move away from the hole edge, the stresses dip down a bit on an approximately linear line, become more negative, then bottom out, 3) from the minimum, the stress then rapidly increases until, 4) it crosses the 0 value, goes up a bit, is now tensile, then heads back down to zero. Because the stress is in compression near the hole, there must be a tensile region away from the hole for equilibrium. These simulations do not give clear indication of which overload is closest to the 4% CX—the screening method used here was to compare the fatigue lives predicted using the 5 residual stress fields and match those fatigue lives and the crack paths.

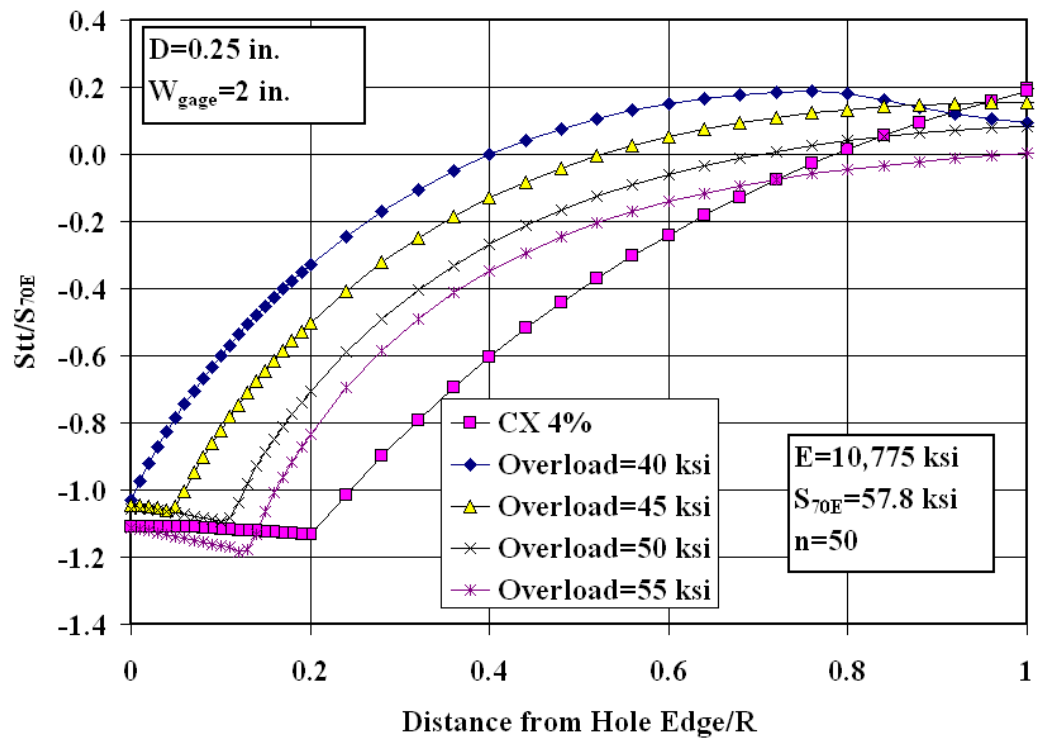


Figure 81. Cold Working (CX) and Overload Simulations, 2 inch Gage Widths

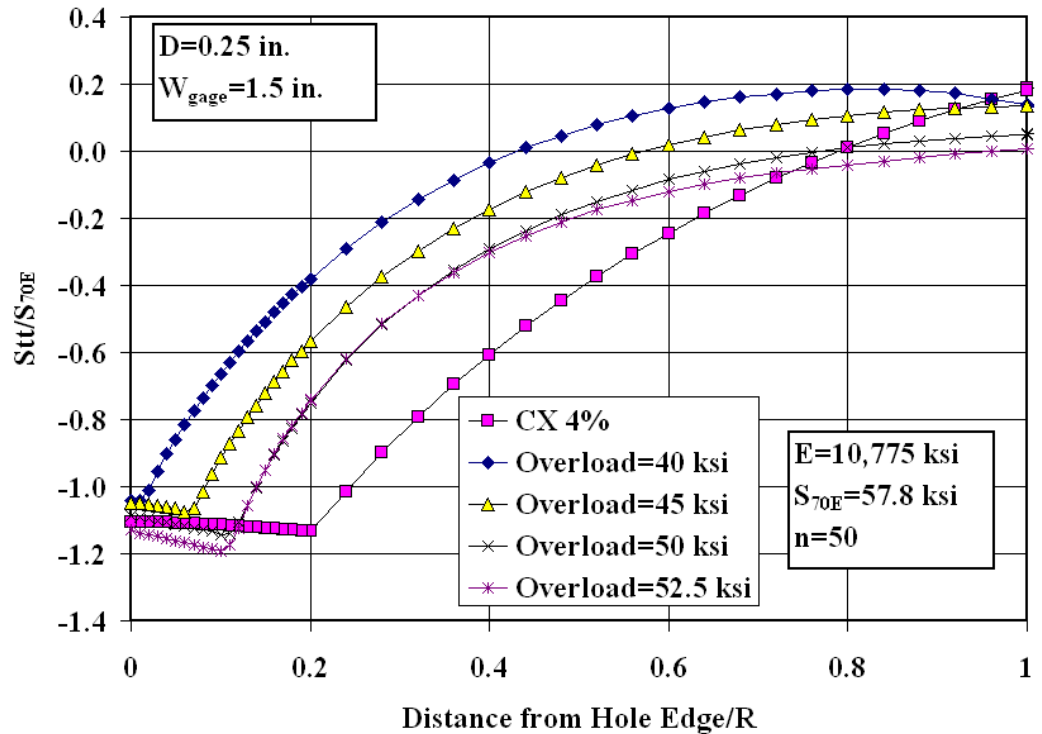


Figure 82. Cold Working (CX) and Overload Simulations, 1.5 inch Gage Widths

7.2 Analyses Using Equivalent Overload (Task 4)

Technical Deliverables:

- Fatigue crack growth analyses (Single and double Cracked-Holes (if necessary) (a vs. N))
- Document modeling improvement ideas.

Residual stresses were computed in StressCheck for 11 different single tension overload levels; the computed residual stresses for 6 of the tensile over levels are shown in Figure 83 below. Residual stresses at tension overloads of 36, 37, 37.5, 38 and 39 ksi were also computed; however, these were intermediate to the 35 and 40 ksi overload levels in Figure 83, and were omitted for clarity.

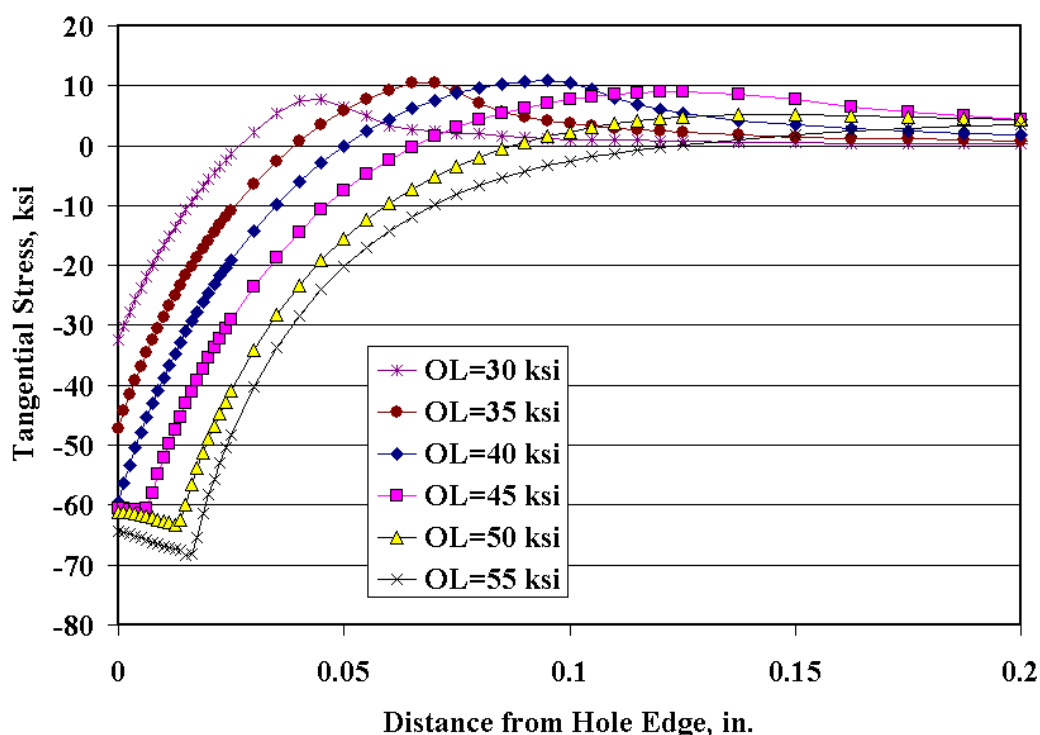


Figure 83. Computed Residual Stresses by Tensile Overload Level

Stresses were put into AFGROW compatible form, and read into the AFGROW residual stress interface (actually, we've created an Excel macro that reads in any .lkp file, *.sd3 (residual stress) file, any AFGROW file or model, and any spectrum file, and runs a series of AFGROW computations, given initial geometry parameter values such as initial crack length).

The experimentally measured initial crack lengths (after pre-cracking and reaming were completed) for each of the 9 coupon tests that have been completed were used to start each of the retro-dictions. Nine (9) retro-dictions were computed for each overload level; in addition, 9 retro-dictions were computed using each of the following initial or boundary conditions: initial flaw size of 0.05 in. (damage tolerant design flaw size), initial flaw size of 0.005 in. (Joint specs allowable design flaw size if Cold working residual stresses present), 4% cold working residual stress, NASGRO FCG rates for 2024-T351, and Harter-T FCG rates for 2024-T351. The

analyses (retro-dictions, since the experimental results were known *a priori*) are summarized in Figure 84 below.

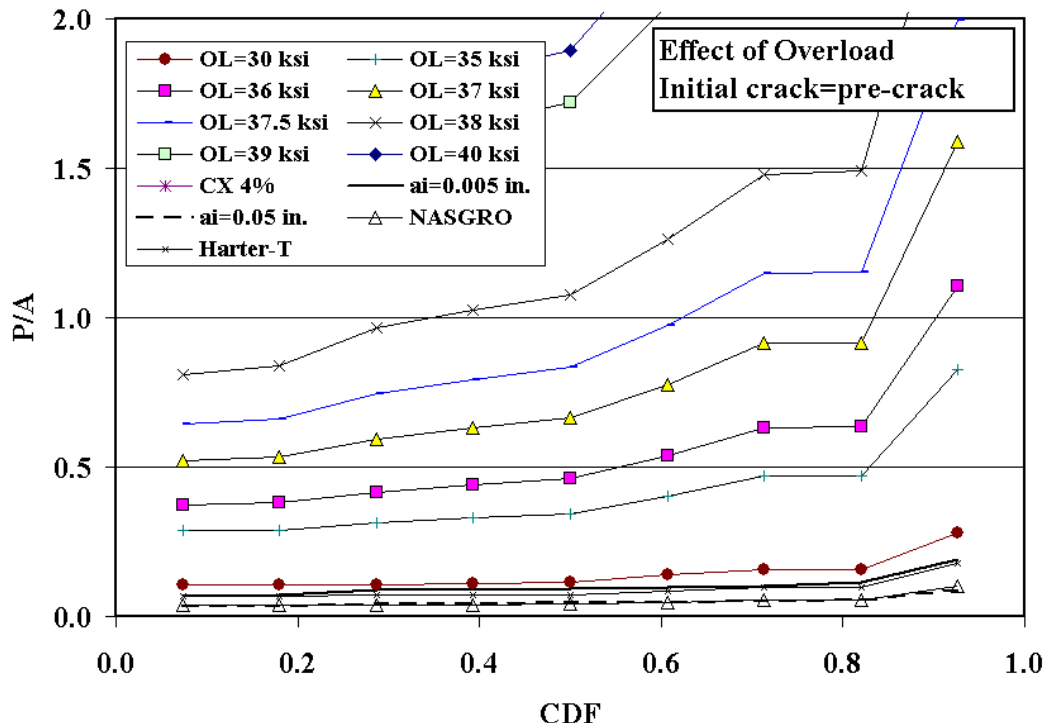


Figure 84. Comparison of Fatigue Crack Growth Rates from Various Sources (Indicated in Legend)

Retro-dictions using the following methods: 1) 0.005 in. initial flaw size (no residual stress), 2) 0.05 in. initial flaw size (no residual stress), 3) coupon specific pre-crack sizes, NASGRO material for AA2024-T351 (no residual stress), and 4) coupon specific pre-crack sizes, Harter-T for AA2024-T351 (no residual stress) on average under-predicted the actual coupon lives by 90%, 95%, 95% and 91%, respectively. The computed lives are clearly strong function of the overload level, as expected. As far as overall ‘performance’ of the overload levels, either 37.5 ksi or 38 ksi tensile overload appears to be the best for calibrating with the experimentally observed lives.

The test of Coupon 2H09 appears to be an outlier—though each coupon has a unique pre-crack length, those pre-crack lengths were roughly equal, so it should be possible to compare them directly. The average number of cycles to failure was 132,125 cycles, with a standard deviation of 34,225 cycles. The number of cycles to failure of 2H09 was, 65,890 cycles, which is almost 2 standard deviations lower than the average number of cycles to failure. Unfortunately, we have not had time to analyze all the fracture surfaces of this coupon, so we do not know if there was an obvious reason for its outlier standing.

Conclusions

Residual stresses resulting from tensile overloads were computed for several tension load levels. The computed residual stresses were used as inputs in AFGROW and crack growth analyses performed using as initial flaws the pre-crack dimensions as measured in constant amplitude tests of 2024-T351 coupons that were cold worked to 4%. Overload levels of 37.5 or 38 ksi

appeared to provide the best calibration to this collection and conditions of cold work coupon tests.

7.3 Experimental and Analytical Investigation of Overload Model

A primary goal of Task 8 testing was to demonstrate the experimental and analytical effect of an initial overload (OL) before fatigue cycling began, and to compare this effect with the experimental and analytical effect of cold working. Section 7.2 detailed the analytical work that identified an overload value of 37.5 or 38 ksi as best representing the effect (as quantified with AFGROW) of the residual stress field due to 4% cold working. 37 ksi was chosen for the experiments as it still provides good correlation with the Task 2 EDM fatigue experiments (Figure 84), and also provides a small measure of safety: assuming that specimen 2H09 is an outlier, the P/A values for all experiments are less than 1.0 at the 37 ksi overload level, meaning that actual specimen lives are slightly longer than predicted.

7.3.1 Task 8 Test Results

Table 35 lists the experiments conducted under Task 8, the test conditions, and fatigue test results. All specimens were 2024-T351 aluminum alloys, 0.25" plate product form, with the fatigue loading in the L (plate longitudinal rolling) direction. The specimen geometry was shown in Figure 15, and the spectrum MB-DIC from Figure 74 was used, with the exceptions shown in the table.

Table 33. Task 8 Specimen Details and Results. All cracks were naturally occurring

Specimen	Cold Worked?	Spectrum	Nominal Spectrum Stress (ksi)	Max. Spectrum Stress (ksi)	1 st cycle overload (37 ksi)?	N _f
2H37	Y	MB-DIC	25	31.25	N	377,691
2H38	Y	MB-DIC	25	31.25	N	441,478
2H39	Y	MB-DIC	25	31.25	N	364,545
2H40	N	MB-DIC	25	31.25	N	56,331
2H41	N	MB-DIC	25	31.25	N	78,305
2H42	N	MB-DIC	25	31.25	N	48,843
2H46	N	MB-DIC*	25	31.25	Y	80,549
2H47	N	MB-DIC*	25	31.25	Y	67,149
2H48	N	MB-DIC*	25	31.25	Y	70,486
2H49	Y	MB-DIC	29	36.25	N	84,022
2H53	Y	MB-DIC	29	36.25	N	91,382
2H55	Y	MB-DIC	29	36.25	N	98,448
2H43	N	MB-DIC	29	36.25	N	36,677
2H44	N	MB-DIC	29	36.25	N	29,576
2H45	N	MB-DIC	29	36.25	N	29,194
2H56	N	CA: R=0*	25	25	Y	133,736
2H59	N	CA: R=0*	25	25	Y	86,419
2H60	N	CA: R=0*	25	25	Y	109,972

* a single 37 ksi overload was applied to the specimen prior to fatigue testing

The test results, along with appropriate results from Table 11, are plotted in Figure 85 (constant amplitude results) and Figure 86 (marker band results). Life improvement factors, relative to the baseline non-cold worked and non-overloaded condition “NoCx” are also shown, where the life improvement factor is simply (Cx life / baseline life) or (OL life / baseline life).

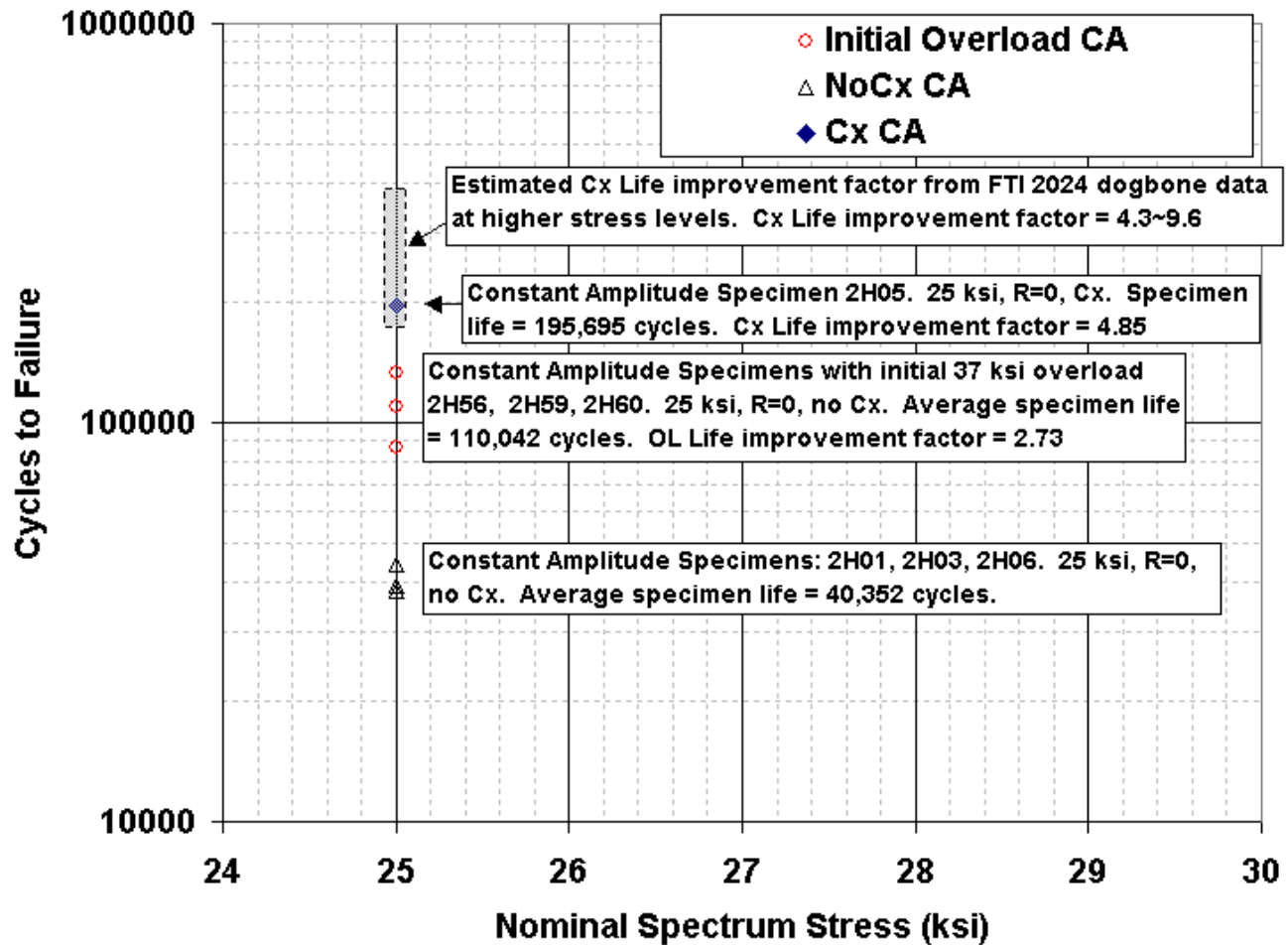


Figure 85. Results Using CA Spectrum: Non Cx, overload, Cx test, and Cx estimates

Under this program, there was only one 25 ksi, CA R=0, 2024-T3 cold worked specimen with a naturally occurring crack tested. However, a paper provided to APES by Fatigue Technology, Inc., Ref. [17], contained two figures (6 and 7 of the reference) presenting life ratios between cold worked and non cold worked 2024 dogbone specimens. Product thickness, hole diameter, product form and specimen details were not stated, though Figure 7 of Ref. [17] specified 2024-T3 product form, open hole dogbone coupon. Both of these figures presented life ratios at higher net section stress levels (30 ksi and 28 ksi), and assuming they follow the trends of the experiments presented here and in Ref. [17], the life ratios (the life benefit due to cold working) should increase as net section stress decreases. This is a logical assumption since the lower the net section stress, the closer the life is to an asymptotic life run-out or endurance limit. As such, the life ratios from reference [17] should be conservative when applied to Figure 85 at a 25 ksi net section stress level. Furthermore, Figure 4 in Ref. [17] shows a Cx life improvement ratio of 10x to 30x for Al 2024-T851 in a net section stress range of 25 to 30 ksi, comparing a Cx open hole to a reamed, non-Cx open hole. Even at a net section stress of 40 ksi the Cx life improvement ratio is still 2.5.

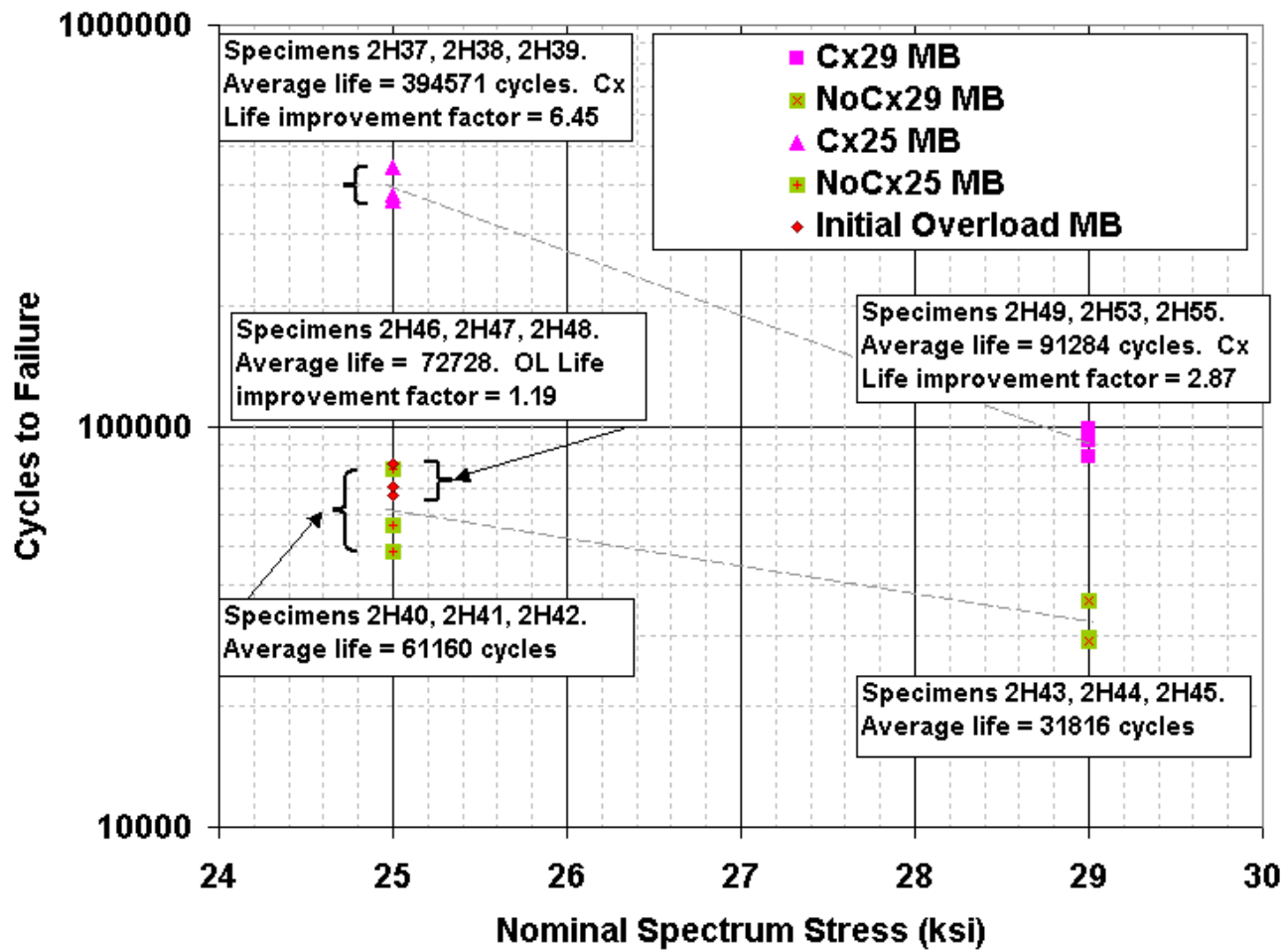


Figure 86. Results Using MB-DIC Spectrum, Non Cx, overload, and Cx

No marker band overload tests were conducted at the nominal 29 ksi stress level; had these tests been conducted, they would most likely fall within the fatigue life scatter band of specimens 2H43, 2H44, and 2H45. This is a reasonable assumption due to the following two facts: (1) the 37 ksi overload is of nearly identical magnitude to the maximum spectrum stress at 29 ksi nominal stress (Table 36), and (2) even at the 25 ksi nominal MB-DIC stress level, the overload specimens (2H46-2H48) nearly lie within the scatter band of the baseline specimens (2H40-2H42). In the following analysis section, the baseline average life of 31,816 cycles is also used to represent the ‘actual’ test life for 37 ksi overload specimens under 29 ksi (nominal) MB-DIC spectrum, though none were physically tested.

Table 34. 37 ksi Overload Factor, Relative to the Maximum Spectrum Stress

Spectrum	Nominal Spectrum Stress (ksi)	Max. Spectrum Stress (ksi)	37 ksi overload factor
CA R=0	25	25	1.48
MB-DIC	25	31.25	1.18
MB-DIC	29	36.25	1.02

Examining Figure 85 and Figure 86, we see that while an initial overload can enhance a baseline constant amplitude fatigue life significantly, the effectiveness of the overload was nearly lost if the variable amplitude (VA) spectrum contains fatigue cycles with peak loads about halfway between the mean (nominal) spectrum stress and the overload stress. This VA spectrum is more representative of real aircraft wing spectra than is a constant amplitude spectrum. From a mechanical test perspective, the life benefit due to initial overload was clearly less than the life benefit due to cold working.

7.3.2 Analysis and Correlation of Task 8 Test Results

The mechanical testing showed that an initial overload of 37 ksi did not provide the same life benefit as 4% cold working. However, the equivalent overload *analytical model* may still have merit. Here we apply the model using AFGROW, the methods and assumptions consistent with section 7.2, and compare the model's predicted (P) life results to the (actual, A) test lives of Table .

For all 'actual' lives, the mean of the three replicate tests was used, with the exception being the overload tests under the MB-DIC spectrum at 29 ksi nominal stress. Since none of these tests were conducted, the actual life used for comparisons is the same as the baseline life, 31,816 cycles, using the logic discussed above. Although scatter exists in the actual life test results, we chose to present P/A results using only the mean value of the replicate tests in order to simplify the charts and ensuing conclusions.

For the 'predicted' lives, computations were performed using three models (A, B, and C, Table 37), permuted with three different starting crack sizes and the three spectra tested. The predicted values from model C were used for relative comparisons to both the Cx test results and the OL test results. The resulting sets of P/A values from Model C are denoted as C(Cx) and C(OL).

Table 35. Models A, B, C, and Associated Residual Stress Profiles

Model	Residual Stress Profile
A. Baseline Model (no plasticity corrections)	N/A
B. Baseline Model (with plasticity corrections)	Computed at peak spectrum stress (either 25 ksi, 31.25 ksi, or 36.25 ksi)
C. 37 ksi initial OL model	Computed at 37 ksi

The residual stress profiles for the peak spectrum stress or overload were computed using StressCheck. The residual stress profiles used inside AFGROW (in both the 'a' and the 'c' crack directions) were 50% of the residual stresses as determined by StressCheck, because of a possible bug in the AFGROW implementation of residual stresses that we identified in 2010 and documented in MSRs for this project.

At each of the starting crack sizes, each model was used for a total of three AFGROW runs: 1) spectrum 1, a 25 ksi constant amplitude spectrum, 2) spectrum 2, the MB-DIC spectrum at 25 ksi nominal stress, and 3) spectrum 3, the MB-DIC spectrum at 29 ksi nominal stress. Predicted and actual results are tabulated in Table 38. For each set of the three spectra, the P/A values were ordered as an increasing cumulative distribution functions (CDF) and plotted as an individual series curve in Figure 87, Figure 88, and Figure 89.

Table 36. Analysis Matrix, Predicted Life Values, Actual Test Values, and P/A Metric

Initial Crack Size	Model	Nominal Stress Level (ksi)	Spectrum	P (cycles)	A (cycles)	P/A
0.000959	A	25	CA	28587	40352	0.7084
0.000959	A	25	MB-DIC	30411	61160	0.4972
0.000959	A	29	MB-DIC	17500	31816	0.5500
0.000959	B	25	CA	50544	40352	1.253
0.000959	B	25	MB-DIC	138949	61160	2.272
0.000959	B	29	MB-DIC	156092	31816	4.906
0.000959	C(OL)	25	CA	705571	110042	6.412
0.000959	C(OL)	25	MB-DIC	777186	72728	10.69
0.000959	C(OL)	29	MB-DIC	187901	31816	5.906
0.000959	C(Cx)	25	CA	705571	195695	3.605
0.000959	C(Cx)	25	MB-DIC	777186	394571	1.970
0.000959	C(Cx)	29	MB-DIC	187901	91284	2.058
0.005	A	25	CA	12429	40352	0.3080
0.005	A	25	MB-DIC	13000	61160	0.2126
0.005	A	29	MB-DIC	7593	31816	0.2387
0.005	B	25	CA	21568	40352	0.5345
0.005	B	25	MB-DIC	62277	61160	1.018
0.005	B	29	MB-DIC	69777	31816	2.193
0.005	C(OL)	25	CA	250263	110042	2.274
0.005	C(OL)	25	MB-DIC	276466	72728	3.801
0.005	C(OL)	29	MB-DIC	80500	31816	2.530
0.005	C(Cx)	25	CA	250263	195695	1.279
0.005	C(Cx)	25	MB-DIC	276466	394571	0.7007
0.005	C(Cx)	29	MB-DIC	80500	91284	0.8819
0.05	A	25	CA	5959	40352	0.1477
0.05	A	25	MB-DIC	6275	61160	0.1026
0.05	A	29	MB-DIC	3298	31816	0.1037
0.05	B	25	CA	8984	40352	0.2226
0.05	B	25	MB-DIC	21869	61160	0.3576
0.05	B	29	MB-DIC	22000	31816	0.6915
0.05	C(OL)	25	CA	93211	110042	0.8470
0.05	C(OL)	25	MB-DIC	102300	72728	1.4067
0.05	C(OL)	29	MB-DIC	26500	31816	0.8329
0.05	C(Cx)	25	CA	93211	195695	0.4763
0.05	C(Cx)	25	MB-DIC	102300	394571	0.2593
0.05	C(Cx)	29	MB-DIC	26500	91284	0.2903

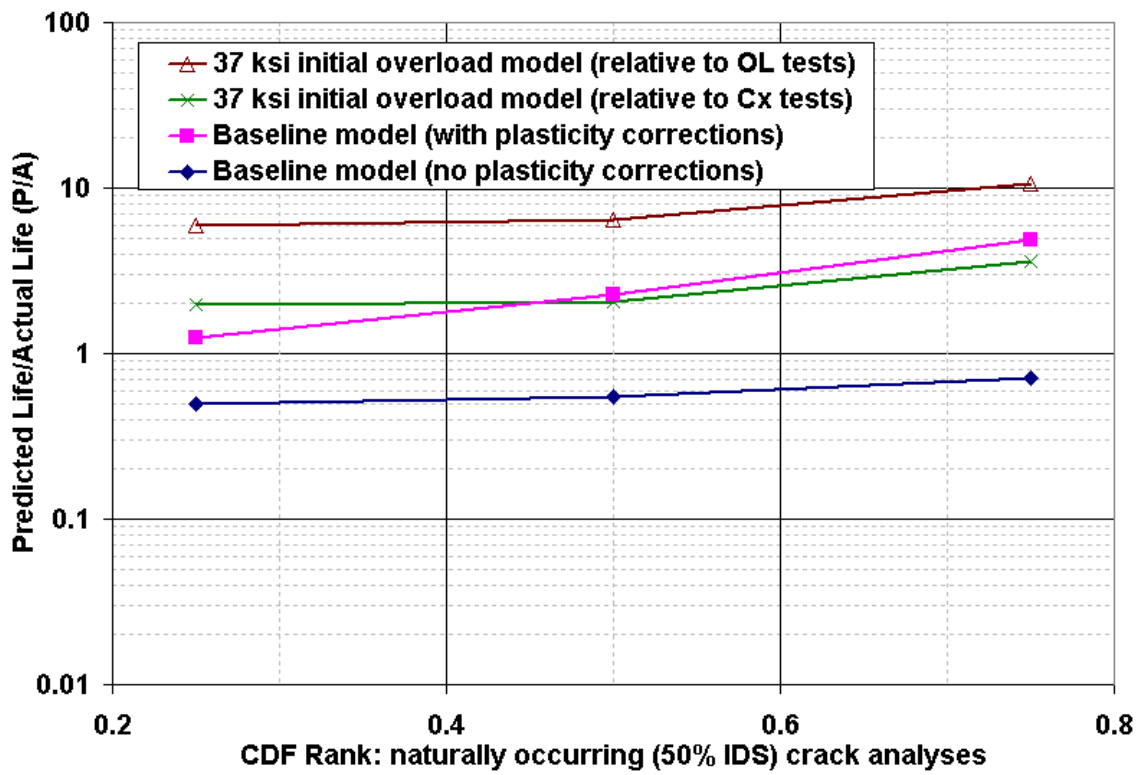


Figure 87. Model P/A Performance, 50% IDS Initial Crack

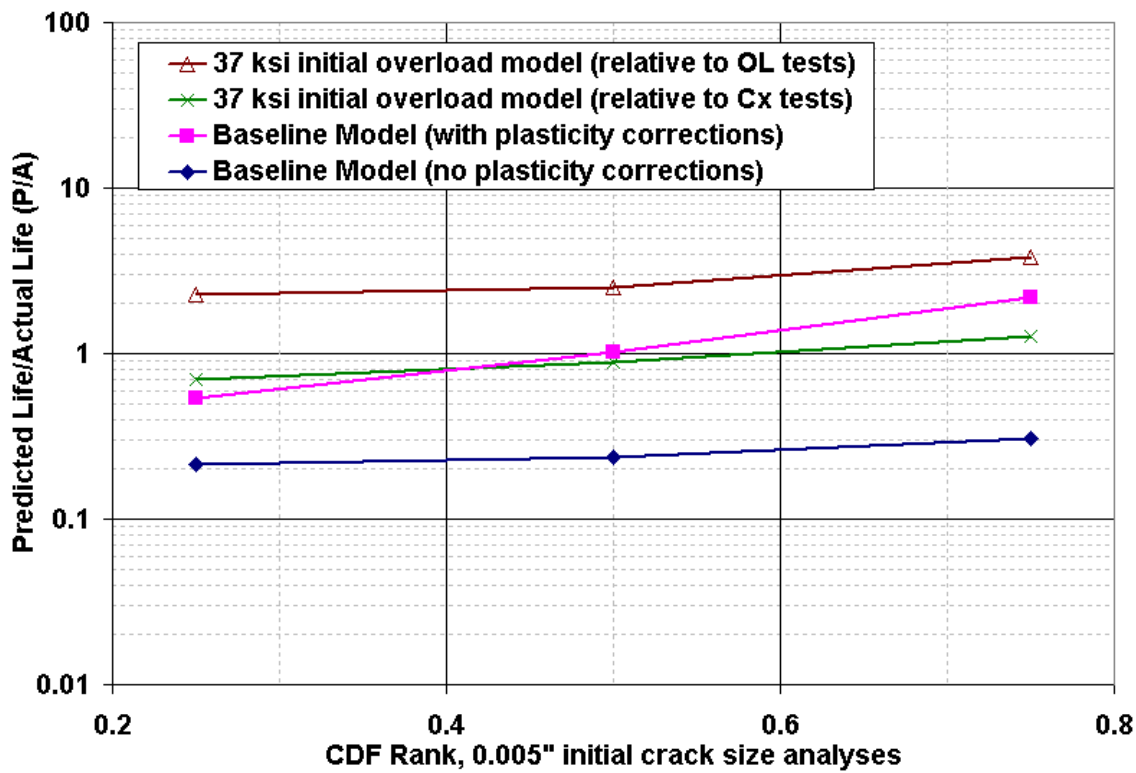


Figure 88. Model P/A Performance, 0.005" Initial Crack

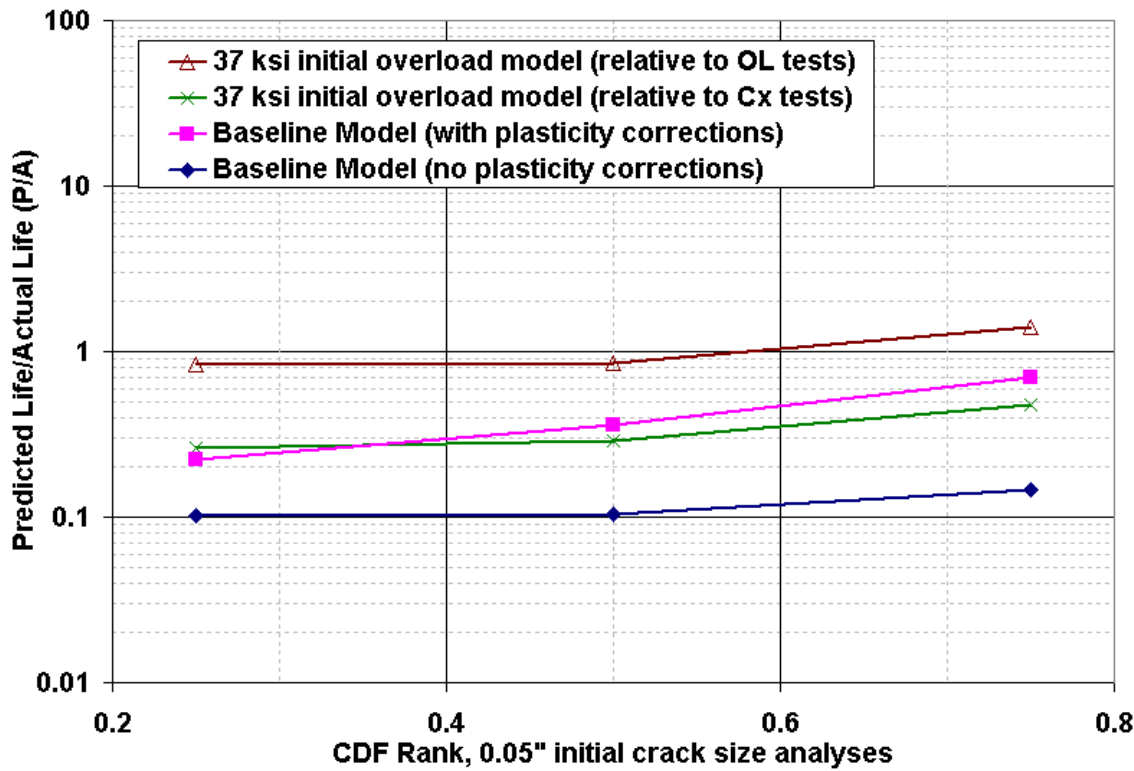


Figure 89. Model P/A Performance, 0.05" Initial Crack

We see from Figure 87 that none of the 50% IDS ($c=a=0.000959"$) initial crack size models do a very good job of predicting the test lives. This is not at all surprising, since the target 37 ksi overload value was based on a detailed analysis of the EDM tests, all of which had crack starter notches plus pre-cracks on the order of 0.02" to 0.05". Figure 88 shows that the 37 ksi overload model predicts the cold work test results fairly well when a starting crack size of 0.005" is used (along with the residual stress profile resulting from the 37 ksi overload). Figure 89 shows that using a starting crack size of 0.05", the 37 ksi overload model does a fairly good job of predicting the tests that had an initial overload, although test data demonstrated that the OL tests had significantly shorter lives than the cold worked tests.

One important thing to note is that in Figure 88, the baseline model (with no plasticity corrections) is giving P/A values of 0.21 to 0.31. This model (0.005" starting crack size) is the current industry standard for analyzing the lives of cold worked holes, but in all comparisons shown in Figure 87, Figure 88, and Figure 89, the actual ("A") value used is the *non-cold worked* test life. If we want to examine the current industry practice, we need to examine how a 0.005" initial crack model (without a residual stress profile used during analysis) predicts the cold worked test lives. This comparison is shown in Figure 90. Clearly, modeling a cold worked hole by using a 0.005" initial crack is extremely conservative, and there is much room for improvement of this practice.

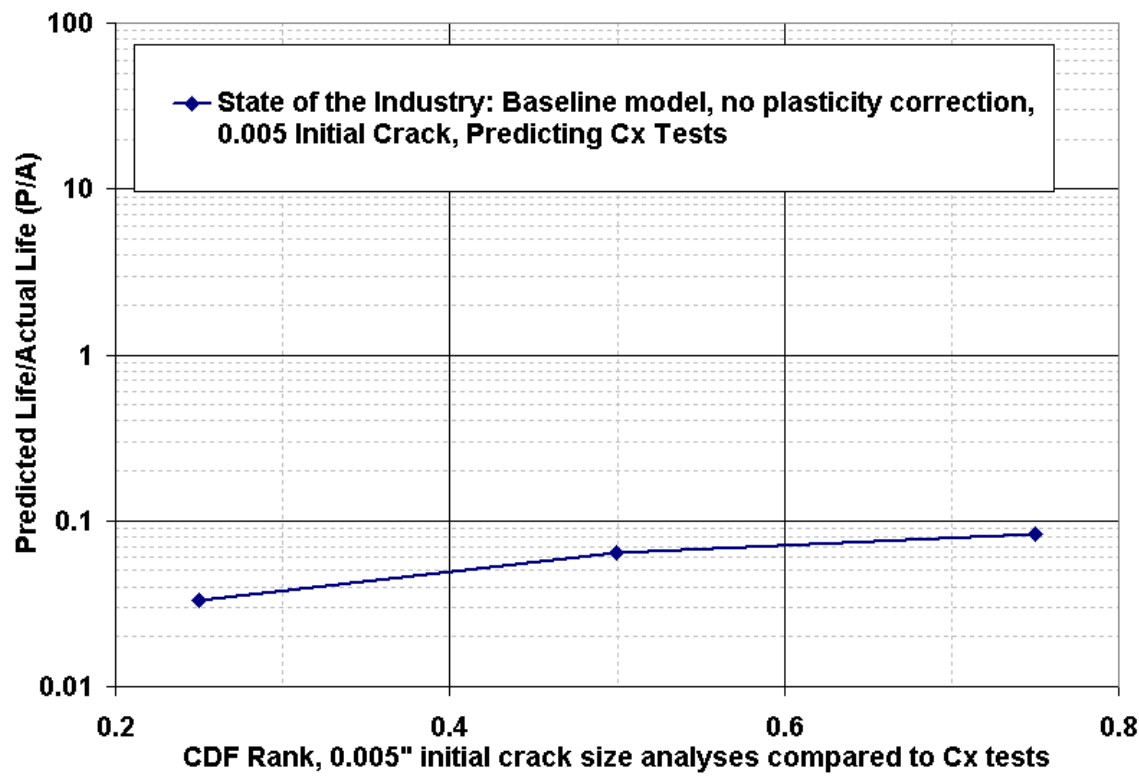


Figure 90. Current Industry Practice for Predicting Fatigue Life of Cold Worked Holes

8 Summary and Conclusions

A focused experimental test program aimed at studying the cyclic behavior of plastically exercised material conditions around cold-worked holes produced insights into deficiencies as well as potential paths to viable solutions of analytical tools based primarily on linear elastic concepts; i.e., finite element modeling of residual stresses and their resolution into applied spectrum and crack growth simulations using conventional LEFM with some plasticity corrections. One of the major challenges noted is that many of the industry's analytical approaches to this issue do not take into account the multi-axial, non-uniform material behavior induced by the cold work process.

An exception to this statement above is advanced elastic-plastic finite element modeling of the mandrel cold work process, which may provide better estimates of the residual strain and stress state, although they were not considered in this effort. These more sophisticated methods could readily complement the observations from this program to augment technology readiness levels. However, one of the principal directions of this program was to determine whether some of the obstacles within the analytical procedures and the logic supporting those particular procedures as they are applied today to USAF aircraft such as the A-10 or F-16 could be overcome for better solutions while maintaining the proper spirit of ASIP. The present procedures are in place more for the protection of the system and perceived unknowns, than an analytical PRE-diction of the crack growth behavior from cold-worked holes. They provide some credit with very little risk. Many of the models investigated improved upon the correlation of analytical methods relative to those in practice on present aircraft systems, but again most did not replicate or adequately simulate the crack path, crack size, and crack growth rates as a function of applied loads (compared to experiments) to enable or even recommend immediate implementation. However, it is important to note that most of the methods do provide better representations of structural behavior in cold-worked applications than do the computations currently authorized for use in ASIP applications.

While current ASIP methods under-compute the cold worked benefits by factors of 10x to 30x, any one of the several methods explored under this effort shows service capabilities two to five times greater than those analytical estimation procedures being used on in-service vehicles. One thing that became very clear during the execution of this program is that modeling of fatigue response in residual stress fields is subject to many sources of variation, any of which can significantly affect predicted response. Understanding these sources of variation (and their statistical distribution) will be a necessary part of any physical based solution proposed. Such sources of variation include:

- Threshold crack growth rate behavior
- Crack growth behavior through plastically deformed material (we currently apply LEFM based crack growth laws in these regions)
- The residual stress state. Many techniques provide wide varieties of answers. Which one is correct, or are none correct?
- Variability in residual stress state as a function of nominal processing parameters (for instance, the cold working equipment manufacturer has established quality control procedures with limits on dimensions of holes and process equipmentthese quality

control procedures still allow significant variations in the cold work level from 3 to 5% for a nominal 4% cold worked hole).

The direct use of empirically-derived scale factors (a simple life improvement factor not unlike what the use of 0.005 initial cracks vs. 0.05 initial cracks currently provides) is equally as comfortable as the more complex single overload method. Both require many experiments to either derive the necessary scale factor or to compute the controlling equivalent over-load as functions of materials, stress levels, and spectra. Either approach leaves you with another dependency on experimental verification when variation from the comfort zone is encountered.

Many applications for engineered residual stress (shot peening, laser peening) are certified by testing, and this, too, would be required by the single overload model for every new application. As such, it seems more prudent to invest in the physical based approach and into understanding true damage progression and the impact of the principal sources of variation governing cold worked material response. Sufficient technologies and analysis tools have emerged augmenting the understanding of fracture mechanics in complex residual strain fields, and it is the investigators' opinion that these are close at hand. Again: Those interested in capturing the full benefits and economic advantage afforded by proper characterization of the cold work process should continue to promote a robust physical based solution; thus to change to this paradigm requires consideration of the multiple aspects of the ASIP philosophy and a demonstration of capabilities within that philosophy.

9 References

- [1] ASTM Standard E647, "Standard Test Method for Measurement of Fatigue Crack Growth Rates," ASTM International, West Conshohocken, PA, 2000, DOI: 10.1520/E0647-00, www.astm.org
- [2] Paul, Clare A. "Crack Growth Database V3.1 for Windows 95 and Access 97," Electronic media (CD), 1998.
- [3] Edwards, P.J. and Newman, J.C., Jr., "Short-Crack Growth Behavior in Various Aircraft Materials," AGARD Report No. 767, AGARD-R-767, 1990. Neuilly-Sur Seine, France: North Atlantic Treaty Organization.
- [4] Brooks, C.L., Prost-Domasky, S., and Honeycutt, K., "Determining the Initial Quality State for Materials," presented at the 1998 USAF Aircraft Structural Integrity Program Conference, San Antonio, Texas, December 1998.
- [5] ASTM Standard E8, "Standard Test Methods for Tension Testing of Metallic Materials," ASTM International, West Conshohocken, PA, 2009, DOI: 10.1520/E0008_E0008M-09, www.astm.org
- [6] MIL-HDBK-5H, "Metallic Materials and Elements for Aerospace Vehicle Structures," 1 December 1998.
- [7] Cintron, Rommel, and Saouma, Victor, "Strain Measurements with the Digital Image Correlation System Vic-2D," Report CU-NEES-08-06, NEES at CU Boulder, September 2008.
- [8] ASTM Standard E399-09e2, 2009, " Standard Test Method for Linear-Elastic Plane-Strain Fracture Toughness KIC of Metallic Materials," ASTM International, West Conshohocken, PA, 2009, DOI: 10.1520/E0399-09E02, www.astm.org
- [9] ASTM Standard E1820, " Standard Test Method for Measurement of Fracture Toughness," ASTM International, West Conshohocken, PA, 2011, DOI: 10.1520/E1820-11, www.astm.org
- [10] Brooks, C.L., Mills, T.B., Prost-Domasky, S.A., and Honeycutt, K.T., "Development of a Holistic Structural Integrity Process," Dual Use Science & Technology Program (DUST) Final Report for Contract: F33615-03-C-3301, 26 October 2006.
- [11] Merati, Ali, "Fractography Results for Fatigue Coupon Testing of Unclad AA2024-T351 Plate," LTR-SMPL-2005-0164, 2005.
- [12] Joint Service Specification Guide, "Aircraft Structures," JSSG-2006, 30 October 1998.
- [13] Golden, Patrick John (2001) "High Cycle Fatigue of Fretting Induced Cracks", PhD Thesis, Department of Aerospace Engineering, Purdue University, 127 pp.
- [14] Newman, J.C., Jr. and Raju, I.S. (1986) "Stress-Intensity Factor Equations for Cracks in Three-Dimensional Finite Bodies Subjected to Tension and Bending Loads", Chapter 9 in Computational Methods in the Mechanics of Fracture, S.N. Atluri, Editor, pp. 312-334.
- [15] Nadri, B., Edwards, L., Fitzpatrick, M.E., and Lodini, A., "Analysis of Residual Stresses Following Overloading of Cold Expanded Holes Using the X-ray Diffraction Technique and Finite Element Method," Journal of Neutron Research, Vol. 12 (1-3), Jan-Sep 2004, pp. 219-224.
- [16] Prime, M.B., "The Contour Method: A New Approach in Experimental Mechanics," Proceedings of the SEM Annual Conference, June 1-4, 2009, Albuquerque, New Mexico, Paper Number 156.
- [17] Reid, Len. "Answers to Cold Working Questions You Were Afraid to Ask," Fatigue Technology Inc., internal document 281347, Log #35685.

[18] Mills, Thomas B., Honeycutt, Kyle T., Brooks, Craig L., Sharp, P. Khan, Loader, Chris, and Crawford, Bruce, "Development and Demonstration of an Holistic Structural Integrity Process using the Initial Discontinuity State Concept for 7050-T7451 Aluminum," Proceedings, USAF Aircraft Structural Integrity Program Conference, Memphis TN, 2004.

APPENDIX

Table A-1. Traveling Microscope Measurements of Crack Growth in Non-Cold Worked Coupons.

Specimen	Stress	Cycles	NE Surface	NE Bore	Specimen	Stress	Cycles	NE Surface	NE Bore
	ksi	1000s	in.	in.		ksi	1000s	in.	in.
2H34	25	1	0.02472	0.03482	2H33	25	14	0.21386	0.20376
2H34	25	2	0.03166	0.04148	2H33	25	15	0.23184	0.22754
2H34	25	3	0.03934	0.04724	2H33	25	16	0.25826	0.25000
2H34	25	4	0.04562	0.05612	2H33	25	17	0.28016	0.25000
2H34	25	5	0.05576	0.06716	2H33	25	18	0.31288	0.25000
2H34	25	6	0.06494	0.08040	2H33	25	19	0.36470	0.25000
2H34	25	7.5	0.08718	0.10686	2H33	25	20.3	0.47420	0.25000
2H34	25	9	0.10898	0.12770	2H20	25	0	0.02628	0.03418
2H34	25	10	0.12974	0.14936	2H20	25	1	0.03026	0.03418
2H34	25	11	0.15420	0.16526	2H20	25	2	0.03276	0.03622
2H34	25	12	0.18110	0.19432	2H20	25	3	0.03756	0.04384
2H34	25	13	0.20514	0.21438	2H20	25	4	0.04100	0.04656
2H34	25	14	0.24210	0.23880	2H20	25	5	0.04664	0.05672
2H34	25	15	0.26620	0.25000	2H20	25	6	0.05878	0.06562
2H34	25	16	0.29138	0.25000	2H20	25	7	0.06836	0.07536
2H34	25	17	0.34012	0.25000	2H20	25	8	0.08192	0.08570
2H34	25	18	0.39738	0.25000	2H20	25	9	0.09228	0.10750
2H33	25	1	0.02914	0.03640	2H20	25	10	0.10378	0.11636
2H33	25	2	0.03572	0.04222	2H20	25	11	0.11580	0.13640
2H33	25	3	0.04204	0.05144	2H20	25	12	0.12644	0.15240
2H33	25	4	0.04552	0.05488	2H20	25	13	0.14294	0.16814
2H33	25	5	0.05462	0.06230	2H20	25	14	0.15580	0.18684
2H33	25	6	0.06556	0.08012	2H20	25	15	0.17600	0.20346
2H33	25	7	0.07820	0.08810	2H20	25	16	0.19922	0.21940
2H33	25	8	0.09068	0.10750	2H20	25	17	0.21866	0.25000
2H33	25	9.3	0.11732	0.12526	2H20	25	18	0.23496	0.25000
2H33	25	10	0.13196	0.13660	2H20	25	19	0.25240	0.25000
2H33	25	11	0.14844	0.15644	2H20	25	20	0.27636	0.25000
2H33	25	12.15	0.17362	0.17600	2H20	25	21	0.32644	0.25000
2H33	25	13	0.19524	0.19078	2H20	25	22	0.40432	0.25000

Table A-2. Traveling Microscope Measurements of Crack Growth in Cold Worked Coupons.

Specimen	Stress ksi	Cycles 1000s	NE				Stress ksi	Cycles 1000s	NE			
			Surface in.	NE Bore in.	Specimen	Surface in.			NE Bore in.	NE Bore in.		
2H08	25	121.312	0.02810	0.03486	2H15	25	176.893	0.10034	0.11784			
2H08	25	121.312	0.04322	0.05304	2H15	25	176.893	0.12578	0.12422			
2H08	25	121.312	0.05162	0.06244	2H15	25	176.893	0.17878	0.15876			
2H08	25	121.312	0.06584	0.07398	2H16	25	137.640	0.02286	0.07736			
2H08	25	121.312	0.07116	0.08384	2H16	25	137.640	0.04844	0.07884			
2H08	25	121.312	0.07858	0.09040	2H16	25	137.640	0.06012	0.08966			
2H08	25	121.312	0.08494	0.10182	2H16	25	137.640	0.06584	0.09720			
2H08	25	121.312	0.09292	0.10472	2H16	25	137.640	0.08356	0.11866			
2H08	25	121.312	0.09946	0.10866	2H16	25	137.640	0.10026	0.13530			
2H08	25	121.312	0.11504	0.12398	2H16	25	137.640	0.11104	0.13530			
2H08	25	121.312	0.13232	0.12704	2H16	25	137.640	0.13476	0.13530			
2H09	25	65.890	0.02166	0.04136	2H16	25	137.640	0.21596	0.13530			
2H09	25	65.890	0.07978	0.08568	2H17	25	110.553	0.04972	0.05872			
2H09	25	65.890	0.39630	0.23260	2H17	25	110.553	0.07234	0.09580			
2H10	25	126.587	0.02200	0.03204	2H17	25	110.553	0.08784	0.12080			
2H10	25	126.587	0.05572	0.07564	2H17	25	110.553	0.09772	0.14836			
2H10	25	126.587	0.07916	0.15736	2H17	25	110.553	0.11310	0.19336			
2H10	25	126.587	0.11726	0.16556	2H17	25	110.553	0.13974	0.19336			
2H14	25	180.066	0.02032	0.02936	2H18	25	131.931	0.04808	0.07680			
2H14	25	180.066	0.02498	0.02994	2H18	25	131.931	0.07156	0.09896			
2H14	25	180.066	0.03542	0.04192	2H18	25	131.931	0.07882	0.11702			
2H14	25	180.066	0.04920	0.05916	2H18	25	131.931	0.09310	0.13376			
2H14	25	180.066	0.06048	0.08062	2H18	25	131.931	0.10068	0.14572			
2H14	25	180.066	0.06922	0.08502	2H18	25	131.931	0.11562	0.16060			
2H14	25	180.066	0.07676	0.08502	2H18	25	131.931	0.13930	0.21088			
2H14	25	180.066	0.09450	0.09496	2H18	25	131.931	0.16758	0.21658			
2H14	25	180.066	0.13896	0.09860	2H18	25	131.931	0.36386	0.21658			
2H15	25	176.893	0.01838	0.03556	2H19	25	138.257	0.05132	0.06248			
2H15	25	176.893	0.02976	0.04916	2H19	25	138.257	0.06992	0.09520			
2H15	25	176.893	0.03656	0.04952	2H19	25	138.257	0.07792	0.11802			
2H15	25	176.893	0.04270	0.07536	2H19	25	138.257	0.08886	0.11044			
2H15	25	176.893	0.04454	0.07822	2H19	25	138.257	0.09870	0.12008			
2H15	25	176.893	0.05382	0.08050	2H19	25	138.257	0.10846	0.23532			
2H15	25	176.893	0.05888	0.09188	2H19	25	138.257	0.12128	0.24438			
2H15	25	176.893	0.06738	0.09777	2H19	25	138.257	0.14258	0.25000			
2H15	25	176.893	0.07756	0.11784	2H19	25	138.257	0.23910	0.25000			
2H15	25	176.893	0.08810	0.11784	2H19	25	138.257	0.37848	0.25000			

Table A-3. Residual Stress Due to Single Overload of 25 ksi on Cold Worked Coupon Geometry.

r in.	S(r,0) ksi	S(0,r) ksi
0	-18.126	-18.126
0.001	-16.5699	-18.126
0.002	-15.0805	-18.126
0.003	-13.6635	-18.126
0.004	-12.3011	-18.126
0.005	-10.9907	-18.126
0.006	-9.73787	-18.126
0.007	-8.52731	-18.126
0.008	-7.3649	-18.126
0.009	-6.24738	-18.126
0.01	-5.16562	-18.126
0.02	3.26021	-18.126
0.04	1.53619	-18.126
0.05	0.95872	-18.126
0.06	0.64233	-18.126
0.08	0.35184	-18.126
0.1	0.22041	-18.126
0.15	0.10338	-18.126
0.2	0.06388	-18.126
0.3	0.03487	-18.126
0.4	0.02342	-18.126
0.5	0.01695	-18.126
0.6	0.01191	-18.126
0.8	-0.00185	-18.126
0.875	-0.01171	-18.126